

学位論文

Search for Supersymmetric Partners of Gluons
in Proton-Proton Collisions at $\sqrt{s} = 13$ TeV

(重心系 13 TeV の陽子-陽子衝突を用いた
グルーオンの超対称性粒子の探索)

平成 28 年 2 月博士 (理学) 申請

東京大学大学院理学系研究科
物理学専攻

南 雄人

Search for Supersymmetric Partners of Gluons in Proton-Proton Collisions at $\sqrt{s} = 13$ TeV

Yuto Minami

Abstract

Supersymmetry (SUSY) is one of the most promising theories which could explain physics beyond the Standard Model (SM). The Large Hadron Collider (LHC) provides proton-proton collisions at the world's highest energies, where production of coloured SUSY particles is highly expected. The R -parity conserved Minimal Supersymmetric Standard Model (MSSM) is phenomenologically motivated. Under R -parity conservation, SUSY particles are pair produced from the collision of SM particles and the lightest SUSY particle (LSP) is stable. According to phenomenological expectations, SUSY partners of quarks (squarks) are likely to have large masses ($\sim O(10)$ TeV) which provide large radiative corrections to make the Higgs boson as heavy as 125 GeV. On the other hand, it is expected that SUSY partners of gluons (gluinos) are possibly light enough to be pair-produced in the proton-proton collisions at the LHC. Each gluino decays into two quarks and a SUSY partner of electroweak gauge boson (electroweakino) via virtual squark. The electroweakino decays to lighter SUSY particles until the LSP is finally produced. Since light gluinos with masses up to ~ 1.3 TeV were already excluded by the previous SUSY searches at the LHC, a focus is now on heavier gluinos whose production may be characterized by non-planar multi-jet with large missing transverse energy (E_T^{miss}).

In this thesis, gluino pair-production is searched for using events with large E_T^{miss} , jets, and no lepton in the final states of the proton-proton collisions recorded by the ATLAS detector at $\sqrt{s}=13$ TeV in 2015. The total amount of data used correspond to an integrated luminosity of 3.2 fb^{-1} .

To optimize the event selection for non-planar multi-jet events, a variable "aplanarity" is newly introduced, which results in better signal selection efficiencies over the previous searches. Four different event selections are prepared to cover a large region of gluino mass and event kinematics.

To estimate the number of SM background (BG) events after the event selection, a new method has been developed which does not rely on Monte Carlo (MC) simulations as much as possible. This method is carefully validated with data outside the signal regions.

No significant excess is observed after the event selections. This result is interpreted using simplified models of gluino decays, where gluinos are pair-produced and decay in a way to preserve R -parity. For massless LSPs, gluinos with masses up to ~ 1530 GeV are excluded with 95% confidence level. This represents the most stringent constraint on SUSY models to date.

Contents

1	Introduction: Standard Model and Supersymmetry	6
1.1	The standard model	6
1.1.1	Problems of standard model	6
1.2	Supersymmetry	11
1.3	MSSM	12
1.3.1	R -parity	14
1.3.2	SUSY breaking term	15
1.3.3	Target SUSY particles	16
1.4	Objectives of this thesis	17
2	LHC and ATLAS detector	20
2.1	Large Hadron Collider	20
2.2	ATLAS detector	21
2.2.1	Overview of the ATLAS detector	21
2.2.2	The coordinate system and nomenclature	21
2.2.3	Magnet system	22
2.2.4	Inner Detector	22
2.2.5	Calorimeter	25
2.2.6	Muon spectrometer	27
2.2.7	Luminosity detector	27
3	Data set and Monte Carlo samples	29
3.1	Data samples	29
3.2	Monte Carlo samples	29
3.2.1	Standard Model MC samples	30
3.2.2	Signal samples	31
4	Object definition and acquisition from data	34
4.1	Jets	34
4.1.1	B-jets	35
4.1.2	Jet cleaning	35
4.2	Electrons	36
4.3	Photons	37
4.3.1	Photon conversion	38
4.3.2	Photon identification	38
4.3.3	Photon isolation	41
4.3.4	Efficiency and purity of photons	41
4.4	Muons	43
4.5	Overlap removal	43

4.6	Missing transverse momentum	44
4.7	Triggers	44
4.7.1	Triggers used in this analysis	45
4.8	Event cleaning	45
5	Event selection and optimization	47
5.1	Discriminating variables	47
5.2	Study of aplanarity	48
5.2.1	Definition of aplanarity, sphericity, and transverse sphericity[60]	49
5.2.2	Thrust	50
5.2.3	Comparison of event shape variables	50
5.2.4	Jets Systematic effects for aplanarity	55
5.3	Optimization procedure	61
5.3.1	Definition of significance	61
5.3.2	Optimization with TMVA	62
5.3.3	Results of optimization with TMVA	63
5.3.4	Distribution check with TMVA results	63
5.3.5	The optimized SRs	65
6	Background estimation	75
6.1	Top BGs and W BGs	75
6.2	Multi-jet BGs	76
6.3	Diboson BGs	76
6.4	Z($\rightarrow \nu\nu$)+jets BG estimation with γ replacement	77
6.5	Data-driven γ replacement	80
6.6	ABCD method for γ +jets CR	80
6.6.1	Selection	80
6.6.2	Monte Carlo sample	82
6.6.3	Evaluation of the 2D correlation	83
6.6.4	Systematic Uncertainty in γ ABCD method	83
6.7	WXYZ method	84
6.7.1	Small Corrections for WXYZ method	87
6.7.2	WXYZ method with ABCD method	87
6.7.3	WXYZ method without ABCD method	88
6.7.4	Fitting implementation of ABCD and WXYZ method	88
6.7.5	Removing contaminating events in CRs	91
6.8	γ /Z and W/Z check	92
6.9	Expectation from MCs	95
6.10	Purity estimation in γ CR	98
6.10.1	Data/MC comparison	98

6.10.2	Purity estimation with isolation template fitting	99
6.11	Summary of CRs	106
6.12	Strategy of validation regions	109
6.13	Fit results for control regions and validation regions	109
7	Statistical treatment	127
7.1	Log likelihood	127
7.2	Profile log likelihood	128
7.2.1	Approximation for discovery limit	129
7.3	CL _S technique	130
7.4	Systematic uncertainties	130
7.4.1	Experimental uncertainties	130
7.4.2	Theoretical uncertainties	131
8	Results	133
8.1	Fit results for signal region	133
8.2	Interpretations and discussions	141
9	Conclusion	145
	Appendix	148
A	Photon	148
A.1	Jet-Photon overlap removal validation	148
A.2	Photon purity estimation with ABCD method	150
A.2.1	The difference of overlap-removal and ID order	150
A.2.2	Correlation study for ABCD method	153
B	TMVA	154
B.1	Genetic algorithm	154
B.1.1	Determination of optimized cut combination	155
C	ABCD method	156
C.1	ABCD method with correction	157

1 Introduction: Standard Model and Supersymmetry

The standard model (SM) of particle physics is very successful model. It consists of quarks, leptons, gauge bosons, and Higgs particle, and all the predicted particles were discovered. In Sec.1.1, the SM and its problems are described. These problems are called physics beyond SM. Supersymmetry (SUSY) is one of the promising theory which can explain the physics beyond SM. The details of SUSY and target signal of this thesis are described in Sec.1.2. The objectives of this thesis are described in Sec.1.4.

1.1 The standard model

Thanks to the discovery of Higgs particle [1, 2], the content of elementary particles in the Standard Model (SM) is completed (Figure 1).

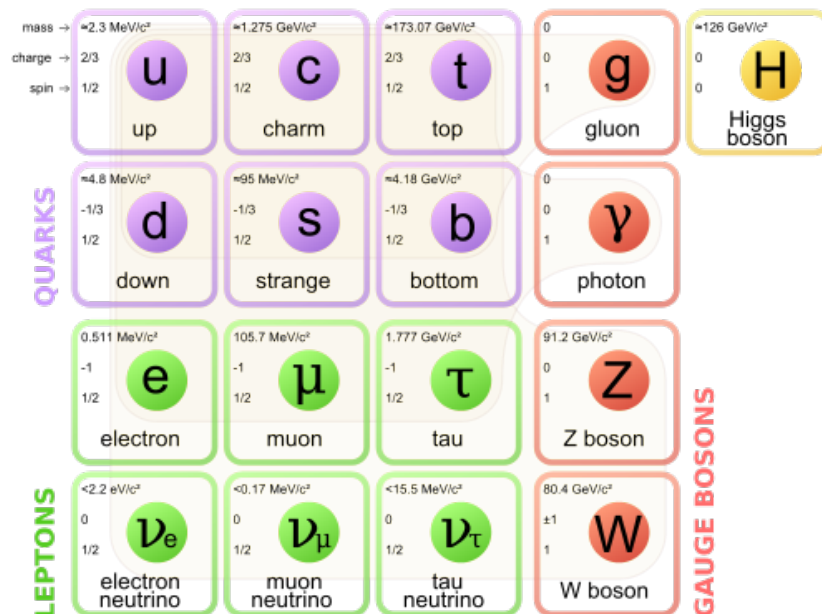


Figure 1: Standard model particles[3].

1.1.1 Problems of standard model

Hierarchy problem

The order of Planck scale is $\sim 10^{19} \text{ GeV}$. This is the scale where quantum effects of gravity is not negligible. In contrast, the mass scale of all the SM particles,

including Higgs particle, are at most $\sim 10^2$ GeV. This is called the electroweak (EW) scale. Because huge difference between the EW scale and the Planck scale, there arises one problem in quantum corrections to Higgs mass. The Higgs field has Yukawa couplings with a SM fermion, like:

$$\mathcal{L} = -\lambda_f \bar{\psi} H \psi \quad (1)$$

This term allows the first diagram of Figure 2 and the quantum correction yields quadratic divergence

$$\Delta m_H^2(\psi) \sim -\Lambda^2, \quad (2)$$

where Λ is the ultraviolet cutoff scale in the calculation. If we consider Λ as the Planck scale, this term becomes the quadrature of the Planck scale. This is also the case for heavy neutrino scale and the GUT scale (described afterwards). To fix the Higgs mass divergence within the EW scale, fine tuning is needed to cancel the effects of the large radiative correction. This problem is called hierarchy problem.

One solution for this problem is to introduce scalar partners of fermions, like

$$\mathcal{L} = -\lambda_f^2 |H| |\phi|. \quad (3)$$

This term make the second diagram of Figure 2 and the quantum correction yields

$$\Delta m_H^2(\phi) \sim +\Lambda^2 + m_\phi^2 \log(\Lambda). \quad (4)$$

Then the quadratic divergences of Eq.(2) and (4) are cancelled (Figure 2). In supersymmetry, all the fermions have scalar partners. Therefore, this problem is automatically solved with supersymmetry.

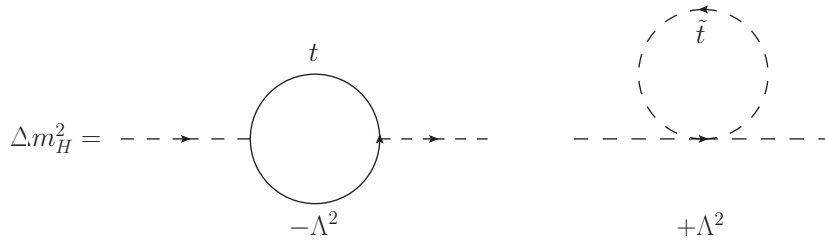


Figure 2: Cancellation of quadratic divergence between contributions from top quark, and scalar top quark.

Dark matter

There are many evidences for the existence of Dark Matter (DM). The DM is a hypothetical matter which is introduced to explain some astronomical phenomena.

If the DM is made up with massive particles, they do not interact with the electromagnetic force and are stable. The oldest and direct evidence is from "Galaxy rotation curves". Indirect but most accurate determination of Ω_{DM} is from "Cosmic microwave background (CMB) " measurement.

Galaxy rotation curves If a galaxy obeys Newton dynamics, the rotational velocity of stars is expected from the equations:

$$\frac{GM(r)m}{r^2} = \frac{mrv(r)^2}{r^2} : \text{Balance of gravitaion and centrifugal force,} \quad (5)$$

$$\text{hence, } v(r) = \sqrt{\frac{GM(r)}{r}}, \quad (6)$$

where, r is the radial length from the centre of the galaxy, $\rho(r)$ is the mass density of visible matters, and $M(r) = \int 4\pi r^2 \rho(r) dr$. If there are no matter at the out of galaxy disk, $v(r) \propto r^{-1/2}$. However, the observed rotation curve of a galaxy is almost constant at large distances as shown in Figure 3. This means some matter exist at the end of galaxy disk in addition to visible matters.

CMB With the anisotropy of CMB, the density of matters in space is determined indirectly. From the results of Planck satellite [5], the baryonic matter density is

$$\Omega_{\text{b}} h^2 = 0.02207 \pm 0.00033, \quad (7)$$

where h is the Hubble constant (100 km/(s·Mpc)). The non-baryonic cold dark matter density is

$$\Omega_{\text{c}} h^2 = 0.1196 \pm 0.0031, \quad (8)$$

and this indicate the existence of DM. Candidates for DM particles are sterile neutrino, axion, and supersymmetric particles. In supersymmetry , the Lightest Supersymmetric Particles (LSP) is neutral and stable, and can be a candidate for the DM, as far as R-parity (1.3.1) is conserved. The DM is one of the strong motivation for supersymmetry.

Grand unification

The coupling unification including electromagnetic, weak, and strong interaction is expected. If they are unified at some energy scale, the coupling constants of these theories ($\alpha_{g'}$, α_g , α_{g_s}) become the same value. These coupling constants are related to gauge couplings:

$$\alpha_{g'} = \frac{g'^2}{4\pi}, \quad \alpha_g = \frac{g^2}{4\pi}, \quad \alpha_{g_s} = \frac{g_s^2}{4\pi}. \quad (9)$$

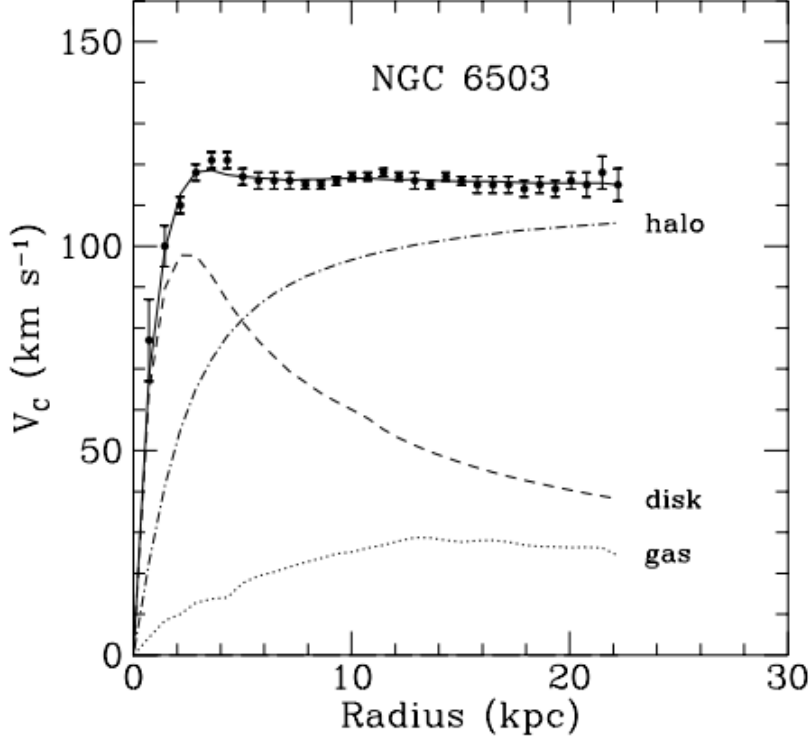


Figure 3: The rotation curve of NGC 6503 from Ref. [4]. The dashed and dotted lines are expected contributions from visible matters, disk and gasses. The dash-dotted line is the expected contributions from dark matter. The observed line is flat and can be explained by existence of dark matter.

In renormalization group, the coupling constants (actually they are not constants) vary with energy scale. This is called "running" couplings. The coupling constant as a function of energy is represented as follows:

$$\frac{1}{\alpha(E)} = \frac{1}{\alpha(E_0)} + \frac{\beta}{2\pi} \ln\left(\frac{E}{E_0}\right), \quad (10)$$

where E_0 is the energy scale we measure the initial coupling constants $\alpha(E_0)$ and is usually Z -mass scale, and β is the beta function which depends on the theory (it depends on the degree of group, and number of fermions and scalars).

The unification scale cannot be obtained simply with the Eq. (10) and (9). The SM representation is arbitrarily chosen and not suitable for unification. For

example, in the SM the covariant derivative can be modified as follows

$$D_\mu = \partial_\mu + ig_s \frac{\lambda^a}{2} A_\mu^a + ig \frac{\tau^i}{2} W_\mu^i + ig' \frac{Y}{2} B_\mu, \quad (11)$$

$$D_\mu = \partial_\mu + i \left(\frac{g_s}{c_s} \right) \frac{c_s \lambda^a}{2} A_\mu^a + i \left(\frac{g}{c} \right) \frac{c \tau^i}{2} W_\mu^i + i \left(\frac{g'}{c'} \right) \frac{c' Y}{2} B_\mu, \quad (12)$$

where c , c' , c_s are arbitrary constants. If the three groups are unified in some scale, the three groups must be the subgroup of one large group. This condition imposes the equations:

$$\text{Tr} \left(\frac{c_s \lambda^a}{2} \right)^2 = \text{Tr} \left(\frac{c \tau^i}{2} \right)^2 = \text{Tr} \left(\frac{c' Y}{2} \right)^2 \quad (13)$$

From this equation, the gauge couplings become

$$g_s, g, \sqrt{\frac{5}{3}} g'. \quad (14)$$

Therefore, if we define $\alpha' = \frac{3}{5} \alpha_{g'}$ and use the coupling constants in Z mass scale and beta function in SM from 1-loop, Eq.(10) become:

$$\begin{aligned} \frac{1}{\alpha_s(E)} &= 8.47 + \frac{7}{2\pi} \ln\left(\frac{E}{M_Z}\right), \\ \frac{1}{\alpha_g(E)} &= 29.6 + \frac{19/6}{2\pi} \ln\left(\frac{E}{M_Z}\right), \\ \frac{1}{\alpha'(E)} &= 59.0 + \frac{-41/10}{2\pi} \ln\left(\frac{E}{M_Z}\right). \end{aligned} \quad (15)$$

These three functions can be written in linear function,

$$y_i = a_i x + b_i, \quad (16)$$

where $x = \ln\left(\frac{E}{M_Z}\right) / 2\pi$ and $y = 1/\alpha(E)$. If these three lines meet at one point E , the condition is

$$\left(\frac{a_1 - a_2}{a_3 - a_2} \right) \left(\frac{b_3 - b_2}{b_1 - b_2} \right) = 1. \quad (17)$$

In the SM case, from Eq. (15), Eq. (17) become 1.36 and is not equal to 1 (left figure of Fig 4). If we introduce MSSM(Sec.1.3), Eq. (10) become:

$$\begin{aligned} \frac{1}{\alpha_s(E)} &= 8.47 + \frac{3}{2\pi} \ln\left(\frac{E}{M_Z}\right), \\ \frac{1}{\alpha_g(E)} &= 29.6 + \frac{-1}{2\pi} \ln\left(\frac{E}{M_Z}\right), \\ \frac{1}{\alpha'(E)} &= 59.0 + \frac{-33/5}{2\pi} \ln\left(\frac{E}{M_Z}\right). \end{aligned} \quad (18)$$

In this case, the Eq. (17) is 1.006 and MSSM shows possibility to be GUT (right figure of Fig 4). If we expect GUT, supersymmetry becomes promising beyond

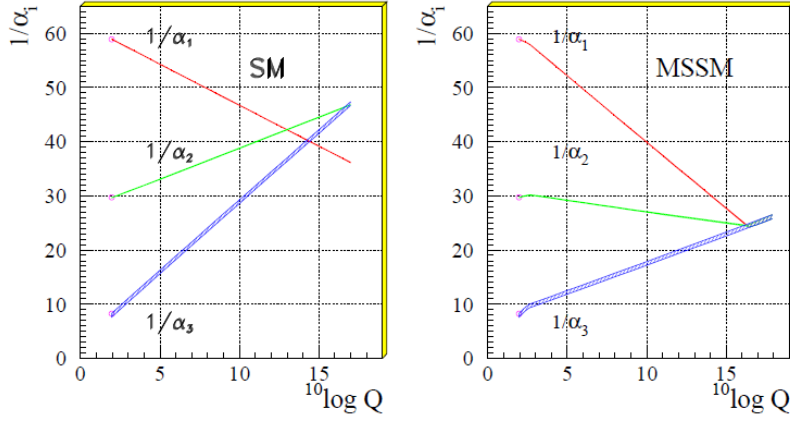


Figure 4: Running of gauge coupling in SM and MSSM [6]. The left figure is the case for SM and there is no meeting point. The right figure is the case for MSSM.

SM theory.

1.2 Supersymmetry

The notation and logical layout of this section mainly follows "SuperSymmetry Demistified"[7] and "Supersymmetry primer"[8].

Supersymmetry (SUSY) introduces the transformation between a fermion and a boson[8]

$$\mathcal{Q} |\text{fermion}\rangle = |\text{boson}\rangle, \quad \mathcal{Q} |\text{boson}\rangle = |\text{fermion}\rangle \quad (19)$$

, where \mathcal{Q} is the SUSY generator. With the transformation, each SM particle has its "superpartner". The naming schemes for the superpartner is

- To add prefix "s-" for fermions, e.g. superpartner of electron is selectron.
- To add suffix "-ino" for bosons, e.g. superpartner of gluon is gluino.

The formalization both including SUSY and Poincaré algebras is constrained by Haag-Lopuszanski-Sohnius[9]. As a result, the SUSY algebra is introduced as:

$$\{Q_\alpha, \bar{Q}_{\dot{\beta}}\} = 2(\sigma^\mu)_{\alpha\dot{\beta}} P_\mu, \quad (20)$$

$$\{Q_\alpha, Q_\beta\} = 0, \quad (21)$$

$$\{\bar{Q}_{\dot{\alpha}}, \bar{Q}_{\dot{\beta}}\} = 0, \quad (22)$$

$$[Q_\alpha, P_\mu] = 0, \quad (23)$$

$$[\bar{Q}_{\dot{\alpha}}, P_\mu] = 0, \quad (24)$$

where P_μ is the translation generator of Poicaré group, dotted character means right-chiral spinor, no dotted character means left-chiral spinor, and $\alpha = 1,2$ and $\dot{\beta} = 1,2$ are the two types of spinor indices. Including the commutation rules of Lorentz generators ($M_{\mu\nu}$) in Poincaré group,

$$[Q_\alpha, M_{\mu\nu}] = (\sigma_{\mu\nu})_\alpha^\beta Q_\beta \quad (25)$$

$$[\bar{Q}^{\dot{\alpha}}, M_{\mu\nu}] = (\bar{\sigma}_{\mu\nu})^{\dot{\alpha}}_{\dot{\beta}} Q_{\dot{\beta}}. \quad (26)$$

Next, Grassmann number (θ) is introduced to make "superfield" which is transformed with both SUSY and Poincaré transformations. In this section, only left-chiral superfields are used:

$$\mathcal{V} = \phi(y) + \theta \cdot \chi(y) + \frac{1}{2} \theta \cdot \theta F(y), \quad (27)$$

where $y^\mu = x^\mu - \frac{i}{2} \theta \sigma^\mu \bar{\theta}$ (Wess-Zumino gauge), θ is Grassmann number, ϕ is a scalar field, χ is a fermion field, F is an auxiliary field, and a dot product means $\chi \cdot \chi \equiv \chi^T (-i\sigma^2) \chi$ and hence $\chi \cdot \chi = \chi_2 \chi_1 - \chi_1 \chi_2$, and 1,2 means two types of spinor indices. Only left-chiral fields are enough to describe fundamentals of the SUSY. These fields are transformed as,

$$\delta\phi = \zeta \cdot \chi \quad (\text{boson to fermion}), \quad (28)$$

$$\delta\chi = -i\chi\sigma^\mu(i\sigma^2\zeta^*)\partial\phi + F\zeta \quad (\text{fermion to boson, and fermion to F}), \quad (29)$$

$$\delta F = -i\zeta^\dagger \bar{\sigma}^\mu \partial_\mu \chi \quad (\text{F to fermion}), \quad (30)$$

where ζ is a fermion. Using these superfields, a minimal extension of the SM with SUSY is made.

1.3 MSSM

The minimal extension of the SM with SUSY is called Minimal Supersymmetric Standard Model (MSSM). Since this is an extension of the SM, the Lagrangian of this model should include

- fermion kinetic terms,
- gauge bosons kinetic terms,
- Higgs bosons kinetic terms,
- Higgs bosons potential terms,
- Higgs-fermion Yukawa coupling terms.

The superfield of each particle can be written using Eq. 27. The summary of superfields are in Table 1. For example, the $SU(2)_L$ left-chiral quarks of first generation are written as,

$$\mathcal{Q}_{1st} = \begin{pmatrix} \tilde{\phi}_u \\ \tilde{\phi}_d \end{pmatrix} + \theta \cdot \begin{pmatrix} \chi_u \\ \chi_d \end{pmatrix} + \frac{1}{2}\theta \cdot \theta \begin{pmatrix} F_u \\ F_d \end{pmatrix}, \quad (31)$$

where χ means quark, and $\tilde{\phi}_u$ means superpartner of quark (squark). The corresponding anti-up and anti-down quarks are written as,

$$\mathcal{U} = \tilde{\phi}_{\bar{u}} + \theta \cdot \chi_{\bar{u}} + \frac{1}{2}\theta \cdot \theta F_{\bar{u}}, \quad (32)$$

$$\mathcal{D} = \tilde{\phi}_{\bar{d}} + \theta \cdot \chi_{\bar{d}} + \frac{1}{2}\theta \cdot \theta F_{\bar{d}}.$$

Similarly, the other fermions can be written in superfield.

Higgs fields (\mathcal{H}) are also written in superfield style. Though complex conjugate Higgs field is introduced in SM, \mathcal{H}^\dagger cannot be used. This is because superpotential must be holomorphic to make SUSY-invariant Lagrangian. Thus, two Higgs fields are introduced for MSSM.

About gauge vector superfields, $\mathcal{V} = \mathcal{V}^\dagger$ is imposed. From this, for example, $SU(3)_C$ superfield is written as

$$\mathcal{G}^a = \frac{1}{2}\theta\sigma^\mu G_\mu^a + \frac{1}{2\sqrt{2}}\theta \cdot \theta\bar{\theta} \cdot \bar{\lambda}_C^a + \frac{1}{2\sqrt{2}}\bar{\theta} \cdot \bar{\theta}\theta \cdot \lambda_C^a - \frac{1}{8}\theta \cdot \theta\bar{\theta} \cdot \bar{\theta}D_C^a \quad (33)$$

Kinetic terms of fermions and Higgs are composed of fermion or Higgs superfields and gauge superfields. For the \mathcal{Q}_i , that becomes

$$\mathcal{L}_{\text{kinetic}} = \mathcal{Q}_i^\dagger \exp\left(Yg'\mathcal{B} + g_s\mathcal{G}^a\lambda^a + g\mathcal{W}^i\tau^i\right)\mathcal{Q}_i\Big|_D, \quad (34)$$

where $\mathcal{V}^\dagger\mathcal{V}\Big|_D$ means $\int d^2\theta d^2\bar{\theta}\mathcal{V}^\dagger\mathcal{V}$. From this the interactions like gluino-quark-squark are derived.

Kinetic terms of gauge vector fields are written as

$$\mathcal{L}_{\text{gauge}} = \frac{1}{4}\mathcal{B} \cdot \mathcal{B}\Big|_F + \frac{1}{2}\text{Tr}(\mathcal{W} \cdot \mathcal{W})\Big|_F + \frac{1}{2}\text{Tr}(\mathcal{G} \cdot \mathcal{G})\Big|_F, \quad (35)$$

where $\mathcal{V}_i\mathcal{V}_j\Big|_F$ means $\int d^2\theta\mathcal{V}_i\mathcal{V}_j$.

For now, the kinetic term of fermions, Higgs, and gauge bosons are implemented. The rest is implemented by the "superpotential". General gauge invariant MSSM superpotentials are written as

$$\mathcal{W} = y_u^{ij}\mathcal{U}_i(\mathcal{Q}_j \circ \mathcal{H}_u) - y_d^{ij}\mathcal{D}_i(\mathcal{Q}_j \circ \mathcal{H}_d) - y_e^{ij}\mathcal{E}_i(\mathcal{L}_j \circ \mathcal{H}_d) + \mu\mathcal{H}_u \circ \mathcal{H}_d, \quad (36)$$

Superfield	$SU(3)_C$	$SU(2)_L$	$U(1)_Y$	Description
fermions and Higgs bosons				
\mathcal{Q}_i	3	2	1/3	quarks and squarks
\mathcal{U}_i	$\bar{3}$	1	-4/3	anti-up type quarks and squarks
\mathcal{D}_i	$\bar{3}$	1	2/3	anti-down quarks and squarks
\mathcal{L}_i	1	2	-1	leptons and sleptons
\mathcal{E}_i	1	2	2	anti-leptons and sleptons
\mathcal{H}_u	1	2	1	Higgs and Higgsinos
\mathcal{H}_d	1	2	-1	Higgs and Higgsinos
gauge bosons				
\mathcal{B}	1	1	0	B and bino
\mathcal{W}	1	1	0	W and winos
\mathcal{G}	1	1	0	gluons and gluinos

Table 1: Summary of superfields. *sleptons* are the superpartner of leptons, *Higgsinos* are superpartners of Higgs. *Bino*, *wino*, *gluino* are superpartners of B, W, and g for each.

where $A \circ A$ means $A^T i \tau_2 A$, y s are Yukawa couplings, from first to third terms means (s)fermion-(s)fermion-Higgs(ino) interactions and include Yukawa couplings, and forth term is called μ term.

Finally, all the terms needed for SM are implemented. In addition to these terms, actually, there are some possible terms can be implemented. However these terms are not desired, since they violate the lepton/baryon quantum numbers. The terms are

$$\mathcal{W} = a_1^{ij} \mathcal{D}_i (\mathcal{Q}_j \circ \mathcal{L}) + a_2 \mathcal{H} \circ \mathcal{L} + a_3^{ij} \mathcal{L}_i (\mathcal{L}_j \circ \mathcal{E}) + f_c^{abc} \mathcal{U}^a (\mathcal{D}^b \circ \mathcal{D}^c), \quad (37)$$

where a s and f are coupling constants. For example, the first term and last term lead to rapid proton decay. To avoid this R-parity conservation is introduced. The details are described in Section 1.3.1.

1.3.1 R-parity

The first term and last term of Eq.37 leads to the rapid proton decay(Figure 5). However, the life time of proton is limited by the search with the Super-Kamiokande

experiment[10]. To avoid the lepton and baryon quantum number violation, " R -parity" is introduced. This is defined as

$$R = (-1)^{3(B-L)+2s}, \quad (38)$$

where B and L are baryon and lepton number, and s is the spin. For SM particles $R = 1$ and for SUSY particles $R = -1$. If R -parity conservation is imposed, all the interactions in Eq.37 are rejected.

R -parity is also motivated from the theoretical point of view. In SO(10) grand unified theories, the R -parity conservation automatically occurs[11].

If R -parity is conserved, two SUSY particles should simultaneously be generated with the collision of SM particles. Once SUSY particles are generated, they can only decay into another SUSY particle with a SM particle or SM particles. Therefore, the lightest SUSY particle (LSP) cannot decay into any other particles and becomes a possible candidate for the dark matter.

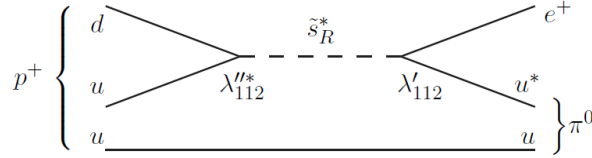


Figure 5: Diagram of proton decays to $e^+\pi^0$ [8].

1.3.2 SUSY breaking term

If supersymmetry is not broken, the supersymmetric partners of the SM particles have the same mass. However, such SUSY particles are not observed. Therefore, a SUSY breaking is needed to explain the experimental fact. If vacuum state $|0\rangle$ is not invariant under SUSY transformation, the SUSY breaks spontaneously. It means $Q_\alpha|0\rangle \neq 0$ and $Q_\alpha^\dagger|0\rangle \neq 0$. The hamiltonian H is the operator P^0 . This can be derived from Eq.20,

$$2H = \{Q_1, Q_1^\dagger\} + \{Q_2, Q_2^\dagger\} \quad (39)$$

Therefore the vacuum expectation value (vev) is

$$2\langle 0|H|0\rangle = \langle 0|Q_1Q_1^\dagger|0\rangle + \langle 0|Q_1^\dagger Q_1|0\rangle + \langle 0|Q_2Q_2^\dagger|0\rangle + \langle 0|Q_2^\dagger Q_2|0\rangle \quad (40)$$

Since the vacuum is assumed not to be SUSY invariant,

$$\langle 0|H|0\rangle > 0, \quad (41)$$

is derived. However, there is no theoretical mechanism to break SUSY spontaneously within MSSM. With any term which can break SUSY spontaneously, one of superpartner particles with mass lighter than the SM particles is predicted after the SUSY breaking, and such particles are not observed. Therefore, SUSY breaking term should be added explicitly. Such terms are added as "hidden sector". It is assumed that the SUSY breaks in this hidden sector. The interaction between particles of MSSM and hidden sector is mediated only by "messenger interaction".

There are some models of mechanisms with different "messenger interactions", and each model predicts different mass spectrum of SUSY particles.

mSUGRA mSUGRA stands for minimal Super GRAvity model. In this model gravity is the messenger interaction[12]. From this model, the ratios of the masses of three gauginos are predicted[8] to be

$$M_{gluino} : M_{wino} : M_{bino} \approx 6 : 2 : 1. \quad (42)$$

Since R -parity is assumed to be conserved, this bino become the LSP. Therefore $M_{gluino} : M_{LSP} \approx 6 : 1$.

GMSB GMSB stands for Gauge Mediated Symmetry Breaking. In this model, a messenger interaction is gauge interaction[13]. From this model, the ratios of the masses of three gauginos are predicted[8] to be the same as mSUGRA case (Eq.42).

AMSB AMSB stands for Anomaly Mediated Symmetry Breaking[14]. In this model, the messenger interaction is via anomaly. In typical models, the ratios of the masses of three gauginos are predicted[15] to be

$$M_{gluino} : M_{bino} : M_{wino} \approx 7 : 3 : 1. \quad (43)$$

Since R -parity is assumed to be conserved, this wino become the LSP. Therefore $M_{gluino} : M_{LSP} \approx 7 : 1$.

1.3.3 Target SUSY particles

Since the LHC is a hadron collider (Sec.2.1), the coloured SUSY particle production cross section is high (Figure 6). Therefore gluino or squark productions are highly expected. Moreover, these particles are produced in pair, since the R -parity conservation is highly motivated as described in Sec.1.3.1.

Squark mass has relation to the observed light Higgs mass of 125 GeV calculated with radiative corrections. With some reasonable parameter settings, a

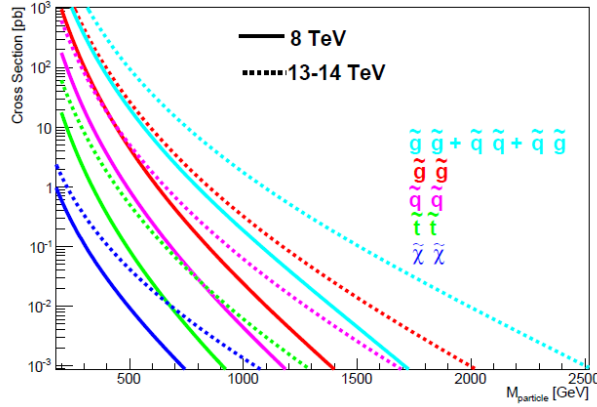


Figure 6: Cross section for SUSY particles in $\sqrt{s} = 8$ TeV and 13,14 TeV [16].

squark (\tilde{q}) mass is expected to be greater than ~ 10 TeV (Figure 7). In contrast, there is no such constraint on gluino (\tilde{g}) mass and hence gluino would possibly be discovered in the LHC-ATLAS experiment. Therefore, the target particle is gluino. Since squarks are heavy, the each of pair-produced gluinos decays directly into "electroweakino" and quark-antiquark pair via a virtual squark. This typical decay model is interpreted with "simplified model" (Sec. 3.2.2). In Run 1 (previous run of the LHC described in Sec. 2.1), the LHC-ATLAS experiment excluded gluino masses up to 1330 GeV [18] as shown in Figure 8. Therefore, pair-produced gluinos whose masses $\gtrsim 1.3$ TeV are the target of this analysis.

1.4 Objectives of this thesis

A search for supersymmetric partner of gluon (gluino) which decays hadronically is presented in this thesis. The new data recorded by the ATLAS detector in proton-proton collision at $\sqrt{s} = 13$ TeV is used. This energy is about twice that in the previous LHC run. The analysed data correspond to $\int L dt = 3.2 \text{ fb}^{-1}$.

The structure of this thesis is as follows. In the Chapter 2, overview of the LHC and the ATLAS detector are described. In the Chapter 3, the used data and Monte Carlo samples are described. The signal samples used for the event selection optimization and interpretation are described in this section. In Chapter 4, the used objects in this analysis and the triggers to select the objects are described. Since this analysis uses hadronic events, the reconstruction of jets are described in precise. Some performances of photons are also described, since the studies about photons are also important in this analysis. In Chapter 5, a variable "aplanarity" is introduced in addition to the conventional discriminant variables. Including aplanarity, the event selection is optimized for gluino signals as the

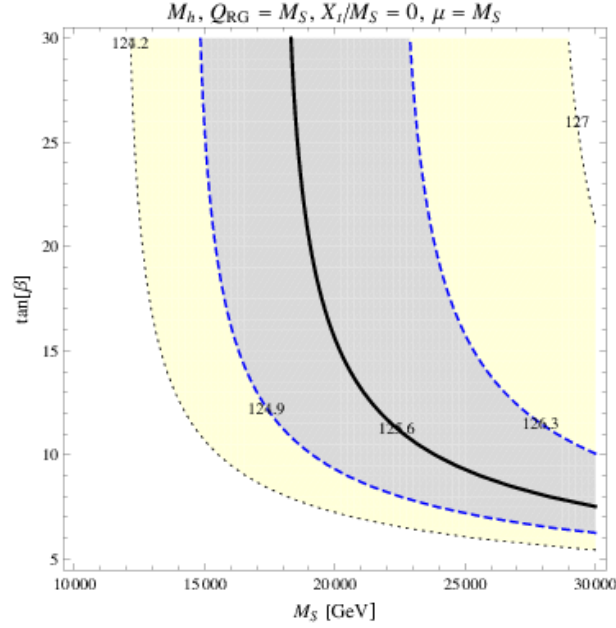


Figure 7: M_h contour in the $\tan \beta$ vs, M_S (sparticle mass) plane. Solid line is central value, dashed lines are 1σ contour, and dotted lines are 2σ contour. $X_t/M_S = 0$, $\mu = M_S$ [17].

target. In Chapter 6, the estimation method of background events after the event selection is described. A new dedicated method to estimate number of events in the signal region mainly using data is applied to this analysis. Also, validation of the estimated number of background events is described. For the background estimation of $Z(\rightarrow \nu\nu)+\text{jets}$ events, the events with hard photons are used. The purity estimation of photon events is also described in this section. In Chapter 7, the fitting method used in this analysis and statistical treatment for exclusion of signals are described. In Chapter 8, the observed number of events after the event selection are described with the estimated number of events. Using the results, the interpretation with some signal models are presented. Finally in the Chapter 9, the conclusion of this analysis is given.

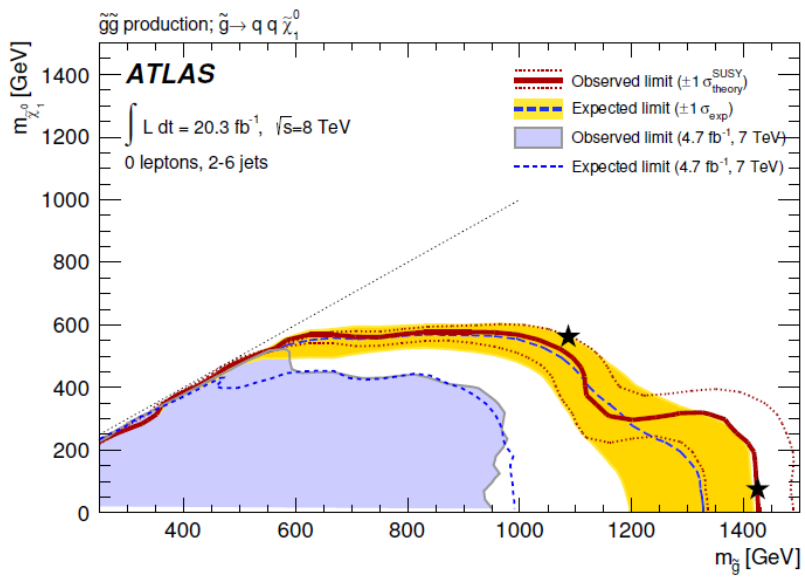


Figure 8: Exclusion contours (95%CL) in the mass plane of LSP and gluino from previous ATLAS analysis[18]. The model is the case pair-produced gluino decays $\tilde{g} \rightarrow qq\tilde{\chi}_1^0$. The solid and dotted red line show the observed limit and its $\pm 1\sigma$ excursion with signal theoretical uncertainties. The dashed blue line shows the expected limit.

2 LHC and ATLAS detector

2.1 Large Hadron Collider

The Large Hadron Collider (LHC)[19] at CERN (the European Organization for Nuclear Research) is a collider with two-ring superconducting accelerator and is installed in the 26.7 km tunnel underground near Geneva (Figure 9). It is designed to collide proton beams with a center-of-mass energy (CME, \sqrt{s}) of 14 TeV and with a peak luminosity of $10^{34} \text{ cm}^{-2}\text{s}^{-1}$. The LHC is designed to accelerate 2,808 bunches for each proton beam and the bunch spacing is 25 ns. It is also designed to collide heavy ions (Pb) with an energy of 2.8 TeV/nucleon and a peak luminosity of $5.1 \times 10^{27} \text{ cm}^{-2}\text{s}^{-1}$.

During 2011 and 2012 (Run1 period), the LHC ran at $\sqrt{s} = 7$ and 8 TeV, and peak luminosity reached $7.7 \times 10^{33} \text{ cm}^{-2}\text{s}^{-1}$ with bunch spacing 50 ns.

The period from 2015 is referred to as Run2. the center-of-mass energy is increased to $\sqrt{s} = 13$ TeV and peak luminosity reached $5.0 \times 10^{33} \text{ cm}^{-2}\text{s}^{-1}$ with bunch spacing 25 ns. The recorded data with the ATLAS detector (Sec.2.2) is described in Chapter.3.

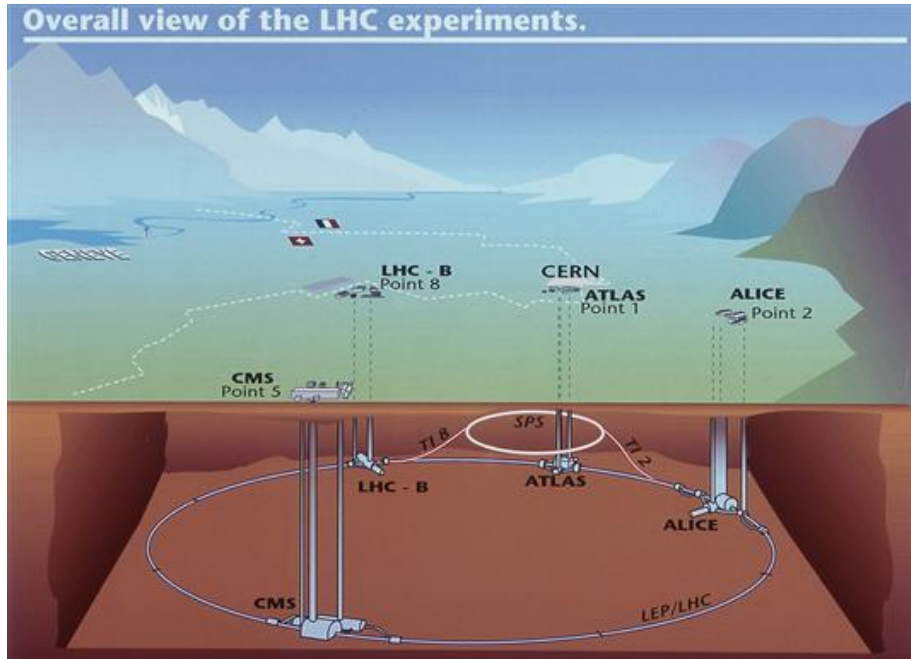


Figure 9: The conceptual figure of LHC[20].

2.2 ATLAS detector

The ATLAS (A Troidal LHC ApparatuS) detector [21] is a general purpose detector built for probing proton-proton and heavy ion collision.

2.2.1 Overview of the ATLAS detector

The detector layout is in Figure 10. The ATLAS detector has the cylindrical shape. In the transverse plane, from inner to outer, the ATLAS detector is composed of the Inner Detector (ID), superconducting solenoid magnet, Liquid-Argon (LAr) electromagnetic (EM) calorimeter, scintillator-tile hadronic calorimeter and the muon chambers which is surrounded by toroid magnets. The both end-caps of the cylinder are covered with LAr hadronic calorimeters, toroid magnets and muon chambers.

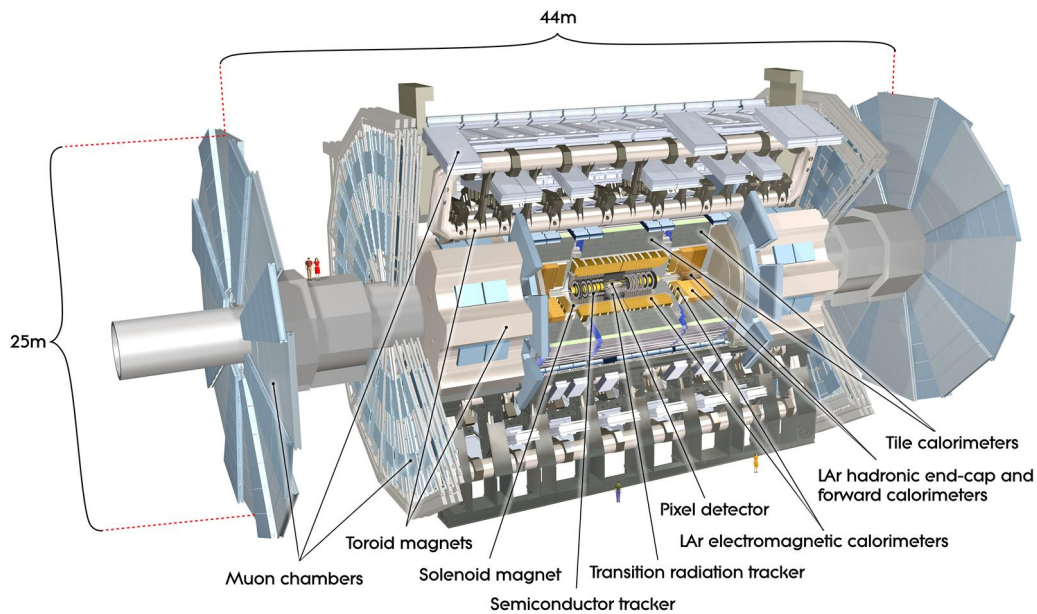


Figure 10: The overall layout of the ATLAS detector.[20]

2.2.2 The coordinate system and nomenclature

For a three-dimensional coordination system, right-handed coordinate system is used. The definition is as follows:

- x-axis: Direction from collision point to the center of the LHC ring.

- y-axis: Upwards direction perpendicular to the plane of the LHC ring.
- z-axis: One of the beam directions.

Azimuthal angle ϕ and polar angle θ are defined as usual polar coordinates.

To describe the 4 momentum of the particle, E, p_T, η, ϕ are used.

E is the energy of the particle.

p_T is a transverse momentum

$$p_T = \sqrt{p_x^2 + p_y^2}. \quad (44)$$

η is a pseudo-rapidity and defined as

$$\eta = -\ln \tan\left(\frac{\theta}{2}\right), \quad (45)$$

where θ is the polar angle. This η is the massless approximation of rapidity

$$y = \frac{1}{2} \ln\left(\frac{E + p_z}{E - p_z}\right). \quad (46)$$

The distance in the pseudo-rapidity and azimuthal angle space is defined as

$$\Delta R = \sqrt{\Delta\eta^2 + \Delta\phi^2}. \quad (47)$$

2.2.3 Magnet system

The ATLAS magnet system consists of four superconducting magnets:

- A solenoid magnet: The solenoid magnet is installed in barrel regions. It covers ID (Sec.2.2.4) and provides 2 T axial magnetic field for tracking.
- A barrel troid: The barrel troid provides approximately 0.5 T magnetic field for central muon detectors.
- Two end-cap troids: Each end-cap troid provides approximately 1 T magnetic field for end-cap detectors.

The overview of magnet system is shown in Figure 11.

2.2.4 Inner Detector

The Inner Detector (ID) is used for tracking charged particles. The ID is in the magnetic field of 2 T and the full tracking coverage is in $|\eta| \leq 2.5$. From inner to outer in radial, the ID is composed of pixel detector, semiconductor tracker (SCT), and the transition radiation tracker (TRT) as shown in Figure 12. The radiation length (X_0) as a function of η is in Figure 13.

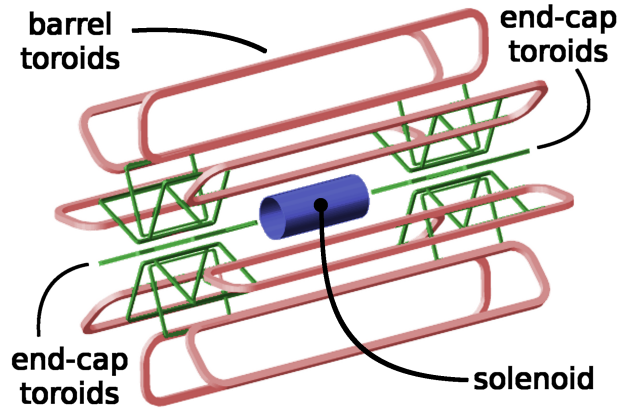


Figure 11: Overview of magnet system in the ATLAS detector[22].

Pixel detector The pixel detector([24]) is the nearest detector to the beam-pipe. It is designed to perform with high granularity and precision measurement. Precise measurement with pixel detector determines the impact parameter and can find decay vertices of particle with measurable decay length. The detector consists of 4 barrel layers and 6 disk layers (3 for each end-cap). The innermost barrel layer is called Insertable B Layer (IBL)[23]. The pixel size of detectors except for IBL is $50 \times 400 \mu\text{m}$ and of IBL is $50 \times 250 \mu\text{m}$. The total 4 barrel layers are at mean radius of ~ 33.25 , ~ 50.5 , ~ 88.5 , and ~ 122.5 mm. The intrinsic accuracy in barrel is $10 \mu\text{m}$ ($R-\phi$) and $115 \mu\text{m}$ (z), and in end-cap is $10 \mu\text{m}$ ($R-\phi$) and $115 \mu\text{m}$ (R).

Semiconductor tracker The SCT consists of layers of silicon microstrip detectors. The SCT system is designed to determine the track, impact parameter and vertex position. The SCT in barrel have eight layers which covers $255 < R < 549$ mm and $|z| < 805$ mm, and the SCT in each end-cap has nine wheel disks which cover $251 < R < 610$ mm and $810 < |z| < 2797$ mm.

Transition radiation tracker The TRT consists of 4 mm diameter straw tube detectors. The TRT provides large number of hits for the track and provides intrinsic accuracy of $130 \mu\text{m}$. In barrel region, the straw tubes are aligned along beam axis, and covers $554 < R < 1082$ mm and $|z| < 780$ mm. In end-cap region, the straw tubes are arranged radially and covers $617 < R < 1106$ mm and $827 < |z| < 2744$ mm. In total, the TRT provides tracking in the range $|\eta| < 2.0$.

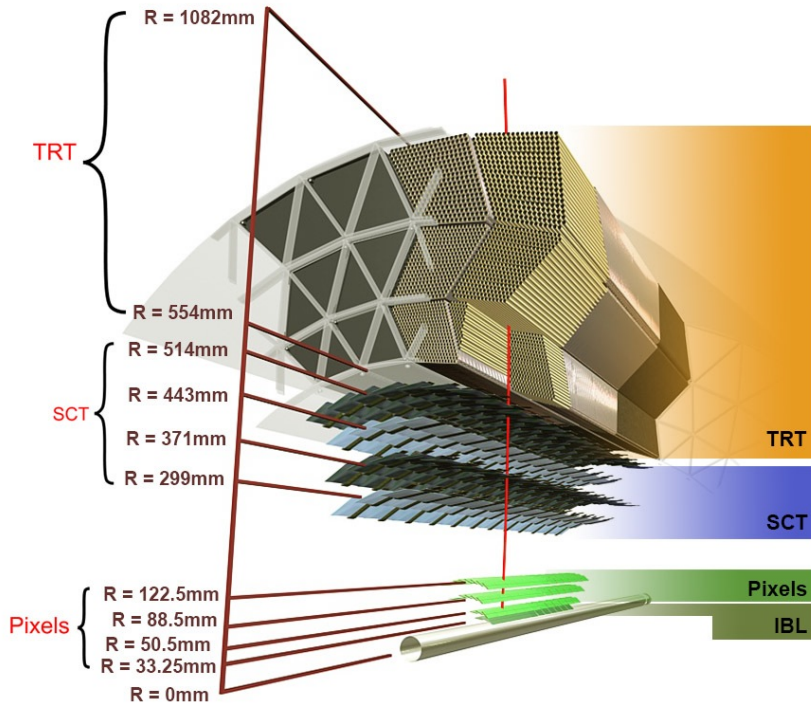


Figure 12: The sectional view of Inner Detector (ID) [20].

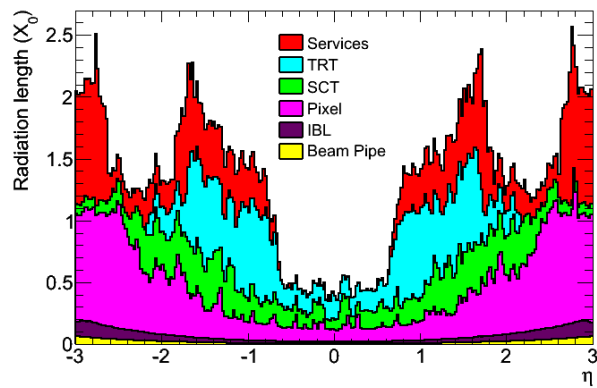


Figure 13: Radiation length versus η for each ID component. [23].

2.2.5 Calorimeter

The overview of the ATLAS calorimeter is presented in Figure 14. The calorimeter consists of 4 types of calorimeter:

- Electromagnetic (EM) calorimeter which covers $|\eta| < 3.2$.
- Hadronic barrel calorimeter which covers $|\eta| < 1.7$.
- Hadronic end-cap calorimeter which covers $1.5 < |\eta| < 3.2$.
- Forward calorimeter which covers $3.1 < |\eta| < 4.9$.

In total, the calorimeter covers the range $|\eta| < 4.9$. The granularity of the EM calorimeter is very fine and provides precise measurements of energies and positions for electrons and photons. The other calorimeter is for jet reconstruction and measurement of E_T^{miss} .

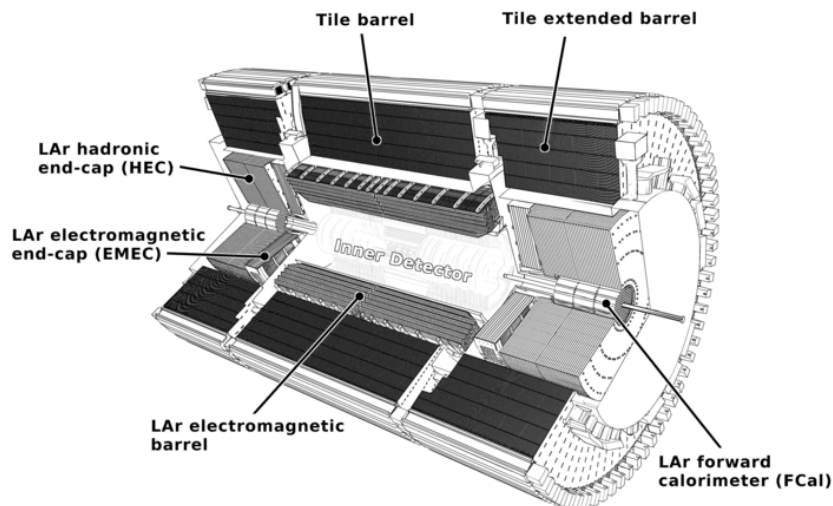


Figure 14: The overview of the ATLAS calorimeters[22].

EM calorimeter				
layer	Barrel		End-cap	
	$ \eta $ coverage	Number of layers	$ \eta $ coverage	Number of layers
Presampler	$ \eta < 1.52$	1	$1.5 < \eta < 1.8$	1
Calorimeter	$ \eta < 1.35$	3	$1.375 < \eta < 1.5$	2
	$1.35 < \eta < 1.475$	2	$1.5 < \eta < 2.5$	3
			$2.5 < \eta < 3.2$	2
layer	$ \eta $ coverage	Granularity $\Delta\eta \times \Delta\phi$	$ \eta $ coverage	Granularity $\Delta\eta \times \Delta\phi$
Presampler	$ \eta < 1.52$	0.025×0.1	$ \eta < 1.52$	0.025×0.1
1st layer	$ \eta < 1.52$	$0.025/8 \times 0.1$	$ \eta < 1.52$	$0.025/8 \times 0.1$
	$1.40 < \eta < 1.475$	0.025×0.025	$1.40 < \eta < 1.475$	0.025×0.025
2nd layer	$ \eta < 1.4$	0.075×0.025	$ \eta < 1.4$	0.075×0.025
	$1.40 < \eta < 1.475$	0.025×0.1	$1.40 < \eta < 1.475$	0.025×0.1
3rd layer	$ \eta < 1.375$	0.050×0.025	$ \eta < 1.375$	0.050×0.025

Table 2: Pseudo rapidity coverage, granularity and number of layers of the calorimeter system[21].

Electromagnetic calorimeter The EM calorimeter consists of LAr detectors with electrodes and lead absorbers. The electrode has accordion geometry which provides complete ϕ symmetry without azimuthal cracks. The summary of parameters is in Table 2. In the barrel region, the EM calorimeter has thickness $> 22X_0$. In the end-cap region, the EM calorimeter have thickness $> 24X_0$. The barrel region which ID covers ($|\eta| < 2.5$) is required for precision measurement. The EM calorimeter is segmented into three layers in radial and shower shape is used in the reconstruction. The first layer (also called "strip section") is equipped with narrow strips in the η direction, and it realises precise η position measurement. This layer is used to measure the energy before the showering and provides improved particle identification ($e/\pi, \gamma/\pi^0$, and so on). The second layer is used to measure the electromagnetic showers. The third layer is mainly used for the separation from hadrons. In the end-cap, the calorimeter has two layers. In the region of $|\eta| < 1.8$, presampler detector is installed inside of the EM calorimeter, and it is used to correct the energy loss in the inner detectors or materials preceding the EM calorimeter.

Tile calorimeter The tile calorimeter[21] consists of scintillating tiles and iron absorber. The signals are read out via wave length shifting fibres to photomultipliers (PMTs). The tile calorimeter is composed of one barrel which covers range of $|\eta| < 1.0$ and of two extended barrels which cover range of $0.8 < |\eta| < 1.7$. In radius, they covers range of $2.28 < R < 4.25$ m. Each barrel is segmented in three layers. The barrel layers have 1.5, 4.1 and 1.8 interaction length (λ) from inner to outer. Extended barrel layers have 1.5, 2.6, and 3.3 λ .

LAr Hadronic end-cap calorimeter The LAr Hadronic End-cap Calorimeter (HEC)[21] consists of two wheels at the behind of EM end-cap calorimeter and they share the same LAr cryostats. The covering region is $0.475 < R < 2.03$ m and $1.5 < |\eta| < 3.2$ and it has overlap with the tile calorimeter, and the forward calorimeter.

LAr forward calorimeter The Forward Calorimeter (FCal)[21] consists of three modules. One is made of copper and the other are made of tungsten. The FCal covers the range of $3.1 < |\eta| < 4.9$ and has $\sim 10\lambda$. For the minimization of neutron albedo in the ID cavity, the FCal is spaced from EM calorimeter by 1.2 m.

2.2.6 Muon spectrometer

The overview of the muon spectrometer[21] is Figure 15. The muon system is composed of Monitored Drift Tubes (MDT), Cathode Strip Chambers (CSC), Resistive Plate Chambers (RPC), and Thin Gap Chambers (TGC). The main parameters are in Table 3.

- MDTs cover large $|\eta|$ region and provide precision measurement of track bended by magnetic fields.
- CSCs are multiwire proportional chambers with cathodes segmented into strips. They have high granularity and withstand the background conditions.
- RPCs are gas detector and the unit is a gas gap formed by two parallel resistive bakelite plates.
- TGCs are multiwire proportional chambers.

RPCs and TGCs are used for triggering with p_T of muons, for bunch-crossing identification (ID), and for measuring muon direction with orthogonal coordinate to MDTs.

2.2.7 Luminosity detector

The ID (2.2.4) is also used in luminosity measurement. The ID provides primary vertices in proton-proton collision. The actual luminosity measurements are performed by LUCID[25, 26].

LUCID is a Cherenkov detector and is installed around beampipe at $|z| = \pm 17$ m from interaction point (IP). It covers range $5.6 < |\eta| < 6.0$. The inelastic proton-proton collision scattering is detected by the Cherenkov photons created by the charged particles. The Cherenkov photons are transferred to photomultiplier tubes(PMTs). The hit pattern data of PMTs of LUCID is processed with Field

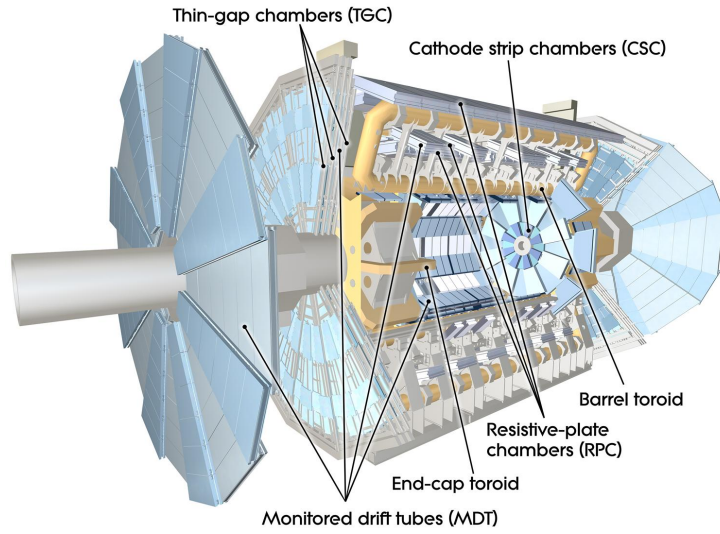


Figure 15: Overview of the ATLAS muon spectrometer components[20].

Components	Coverage in $ \eta $	Function or target
MDT	$ \eta < 2.7$ (2.0 for inner most layer)	Precision-tracking
CSC	$2.0 < \eta < 2.7$	Precision-tracking
RPC	$ \eta < 1.05$	p_T threshold for triggering, bunch-crossing ID, and orthogonal measurement
TGC	$1.05 < \eta < 2.7$ (2.4 for trigger)	p_T threshold for triggering, bunch-crossing ID, orthogonal measurement

Table 3: Main parameters of muon spectrometer[21].

Programmable Gate Arrays (FPGAs) and provides luminosity for given bunch spacing.

3 Data set and Monte Carlo samples

In this chapter the recorded data with the ATLAS detector is described in Sec.3.1. The used Monte Carlo simulated samples are described in Sec.3.2.

3.1 Data samples

The cumulative luminosity as a function of date in $\sqrt{s} = 13$ TeV run is in Figure 16. The total recorded luminosity measured with ATLAS luminosity detector (Sec.2.2.7) is 3.9 fb^{-1} . Since not all detector status are good during a period, the periods when all the detector worked well are vetoed. Then the actually usable data correspond to $\int Ldt = 3.2 \text{ fb}^{-1}$.

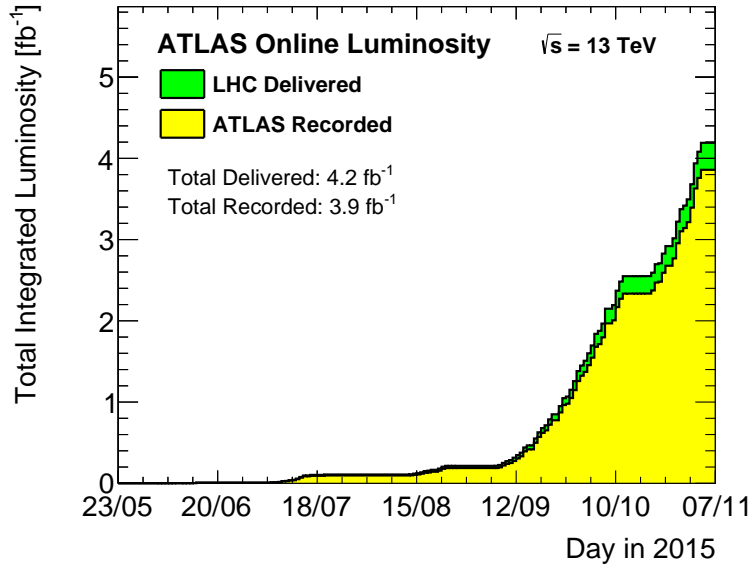


Figure 16: Total accumulated luminosity as a function of day at $\sqrt{s} = 13$ TeV proton-proton collision in 2015[27].

3.2 Monte Carlo samples

In this section, Monte Carlo (MC) simulated samples used in this analysis are described. MC samples are needed to simulate the produced SM processes in proton-proton collision. In this analysis, MC simulated samples are widely used in these studies:

- Event selection optimization to define signal region (SR) where a number of events is counted.
- Background (BG) event estimation in SR.
- Contaminating event estimation in control region (CR).
- Study about the behaviour of SM process event (like, ABCD method study in Sec.6.6).

The generation of MC simulated samples is as follows:

1. Generate partons for hard-process from Parton Distribution Function (PDF). CT10[28], CT10f4[29], and NNPDF[30] are used as the PDF sets.
2. Matrix Element (ME) hard-process is generated with incoming two partons in some order of α_s . The α_s used in ME calculation varies depending on the interaction energy. The reference energy scale is fixed as "renormalization scale" and the α_s of given energy is calculated with the approximated function.
3. Parton shower (PS) is combined with the ME processes, since it is difficult to generate high multiplicity parton processes with ME level calculation. The parton shower from incoming partons is called initial state radiation (ISR) and from outgoing partons is called final state radiation (FSR). To avoid the overlap process in ME+PS combination, various merging processes of partons from ME and PS, such as a MLM merging[31] and a CKKW-L merging[32], are applied.
4. The decay of heavy flavour partons (c , b) are simulated. This is by EVT-GEN[33] except for SHERPA samples.
5. The final state objects without detector simulation are called "Truth" objects. These objects are processed with one of the following three detector simulations. One is the full simulation of ATLAS detector with GEANT4[34]. Second one is the fast simulation with parametrized performance of the ATLAS detector. Third one is the smearing method which smears the jets p_T and E_T^{miss} with Run1 ATLAS detector resolution [35].

3.2.1 Standard Model MC samples

The used processes of the standard model MC processes, generators, and PDFs are listed in Table 4. All of these samples are processed with GEANT4 full-simulation. The details of each process are described in the following paragraphs.

W, Z +jets: Both ME and PS are calculated with SHERPA2.1[36] using CT10 PDF set. The ME up to two partons are calculated at next-to-leading order (NLO) and up to two additional partons are calculated at leading order (LO). The cross section is normalized to next-to-next-to-leading order (NNLO). The alternative MC samples are generated with MADGRAPH5 for ME and PYTHIA8[37] for PS.

γ +jets: Both ME and PS are calculated with SHERPA2.1 using CT10 PDF set. The ME up to three or four partons are calculated at LO with the filter, $p_T^\gamma > 35$ GeV.

$t\bar{t}$ and single top: The ME of $t\bar{t}$, single top (s -channel and Wt -channel) processes are generated with POWHEG-BOX v2 with CT10 PDF set at NLO. The ME of single top (t -channel) is generated with POWHEG-BOX v1 with CT10f4 PDF set at NLO. The PS is calculated with PYTHIA6[38]. The $t\bar{t}$ process cross section is normalized to NNLO+next-to-next-to-leading logarithm (NNLL). The alternative $t\bar{t}$ sample is generated with "aMC@NLO"[39] for ME and HERWIG++[40] for PS.

$t\bar{t} + W/Z/WW$: The samples are generated with MADGRAPH5 at LO for ME and with PYTHIA8 for PS. NNPDF is used for PDF set. The cross section is normalized to NLO.

Diboson process(ZZ, WZ, WW): The samples are generated with SHERPA2.1 with CT10 PDF set. The main diboson processes in which the both bosons decay leptonically are generated at NLO and additional up to three partons are generated at LO. ZZ sample in which one of the bosons decays hadronically is generated at NLO up to one parton and additional partons are generated at LO. WZ and WW samples in which one of the bosons decays hadronically are generated at NLO only for main processes and all additional partons are generated at LO.

Multi-jet: The multi-jet process is generated with PYTHIA8 at LO using NNPDF as PDF set.

3.2.2 Signal samples

As described in Sec.1.3.3, the target signal is pair-produced gluinos each of which decays into two quarks and one electroweakino. These typical decay models are interpreted with "simplified model".

- Direct-decay model: For the case electroweakino is the LSP, the simplified model $\tilde{g} \rightarrow q\bar{q}\tilde{\chi}_1^0$ is assumed (Figure 17(a)). In this model, gluinos are pair-produced and each gluino decays, $\tilde{g} \rightarrow q\bar{q}\tilde{\chi}_1^0$, with branching ratio (BR)=100%.

Process	PDF	Generator
$Z(\rightarrow \nu\nu) + jets$	CT10	SHERPA2.1
$Z/\gamma^*(\rightarrow \ell\bar{\ell}) + jets$	CT10	SHERPA2.1
$W(\rightarrow \ell\nu) + jets$	CT10	SHERPA2.1
$\gamma + jets$	CT10	SHERPA2.1
$t\bar{t}$ and single top($s-$ and $Wt-$ channel)	CT10	POWHEG-BOXV2 + PYTHIA6
Single top	CT10f4	POWHEG-BOXV1 + PYTHIA6
$t\bar{t} + W/Z/WW$	NNPDF	MADGRAPH5+PYTHIA8
Diboson (ZZ, WZ, WW)	CT10	SHERPA2.1
Multi-jet	NNPDF	PYTHIA8
Alternative MC samples		
$Z(\rightarrow \nu\nu) + jets$	NNPDF	MADGRAPH5+PYTHIA8
$Z/\gamma^*(\rightarrow \ell\bar{\ell}) + jets$	NNPDF	MADGRAPH5+PYTHIA8
$W(\rightarrow \ell\nu) + jets$	NNPDF	MADGRAPH5+PYTHIA8
$t\bar{t}$	CT10	aMC@NLO + HERWIG++

Table 4: Summary of the used MC samples for the SM processes with used generator and PDF information.

- Onestep-decay model: For the case electroweakino is the second lightest particle and have charge, the simplified model, $\tilde{g} \rightarrow q\bar{q}\tilde{\chi}_1^\pm \rightarrow q\bar{q}W^\pm\tilde{\chi}_1^0$ is assumed (Figure 17(b)). The BR of $\tilde{g} \rightarrow q\bar{q}\tilde{\chi}_1^\pm$ and of $\tilde{\chi}_1^\pm \rightarrow W^\pm\tilde{\chi}_1^0$ are simplified to be 100%. The masses of particles are set as $m(\tilde{\chi}_1^\pm) = (m(\tilde{g}) + m(\tilde{\chi}_1^0))/2$.

These signal samples are produced with MADGRAPH5+PYTHIA8 using NNPDF for the PDF set. The cross section of gluino pair-production is normalized to the cross section calculated with NLL-fast[41–46]. The detector simulation for these signal samples are processed with fast simulation.

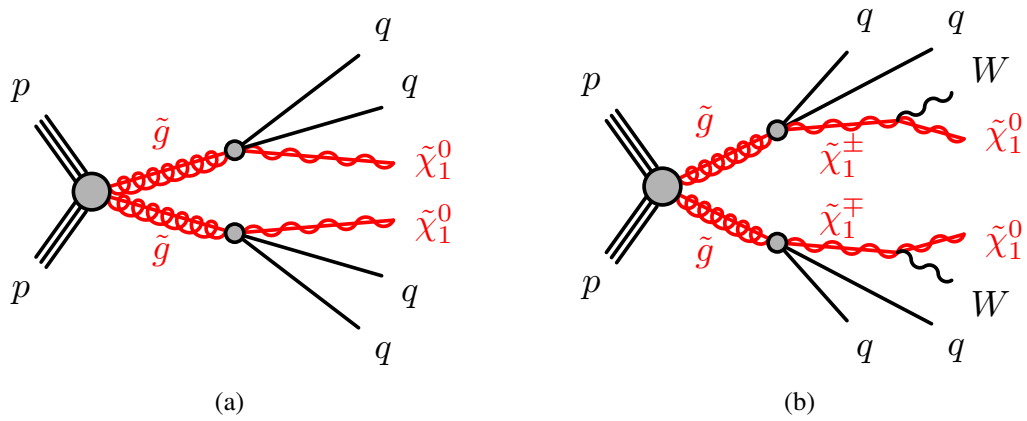


Figure 17: The Feynman diagrams of pair-produced gluinos. (a) shows direct-decay of gluinos. (b) shows onestep-decay of gluinos. Though partons in protons actually interact and produce gluinos, all such processes are represented by one grey circle for simplicity.

4 Object definition and acquisition from data

In this chapter, definitions of physics objects used in this analysis are described. Reconstruction and clustering methods of jets are described in Sec.4.1. Definitions of electrons and muons are described in Sec.4.2 and Sec.4.4. Definition of a photon, variables used for photon identification, and performance of some isolation cuts for photons are described in detail (Sec.4.3) since photons are used for the estimation of the major background of $Z(\rightarrow \nu\nu)+\text{jets}$ events as described in Chapter 6. After the description of objects definitions, triggers and cleaning selection to extract the objects from data are described in Sec.4.7 and Sec.4.8.

4.1 Jets

Final state hadronic particles leave showers in the EM-calorimeter and the hadronic calorimeter. This shower deposits their energy in multiple calorimeter cells. The cell energies are summed up to form clusters. Jets are composed of the clusters. For the jets used in this analysis, clustering method follows topological clustering[47] which is described in the following paragraphs.

In this analysis, jets are reconstructed using the anti- k_T algorithm[48] with cone of size 0.4. Acceptance of jets are required to be $p_T > 20$ GeV and $|\eta| < 2.8$. Moreover, jet cleaning (quality) cuts (Sec.4.1.2) are also applied. The baseline jets are required to pass BadLoose quality cut. These jets are called Loose jets. To calculate some variables used in this analysis, signal jets with $p_T > 50$ GeV are used. To prepare top and W control regions, the information of jets with or without b-hadrons is used. The jet identification definitions are summarized in Table 5.

Topological clustering First, seed cells are put into a seed list with the descending order of S/N , where S is the energy and N is the RMS value of noise, and cells which pass a threshold, $S/N > 6$, are identified as seed cells. Second, the neighbouring cells around the seed cells are added to seed cells if the neighbouring cells pass a threshold, $S/N > 3$, where neighbouring cells mean the eight surrounding cells in the same calorimeter layer. These two processes are iterated until the seed list is empty. With the clustered cells, jets are reconstructed with anti- k_t clustering algorithm as described in following paragraph.

Jet clustering algorithm

In jet clustering algorithm, the distance between clusters (d_{ij}), and between a

cluster and beam (d_{iB}) are used. In general, these are defined:

$$d_{ij} = \min(k_{ii}^{2p}, k_{jj}^{2p}) \frac{\Delta_{ij}^2}{R^2}, \quad (48)$$

$$d_{iB} = k_{ii}^{2p}, \quad (49)$$

where k_t is the transverse momentum (p_T), R is cone size, and $\Delta_{ij} = (\eta_i - \eta_j)^2 + (\phi_i^2 - \phi_j^2)$.

These variables are computed to find the minimum d_{ij} and d_{iB} .

- If $d_{ij} < d_{iB}$: The 4-vector of i th and j th clusters are summed. Then calculate next minimum distances.
- If $d_{iB} < d_{ij}$: The i th cluster is determined as a "jet", and i th cluster is removed from the list of clusters.

These processes are iterated until all clusters are clustered to jets.

In the anti- k_t algorithm, $p = -1$. This means that objects with large k_t tend to compose minimum d and tend to include soft objects. Then, the soft objects don't define the boundary of jet cone and the jet become infra-red collinear safe. Therefore, the jets are robust against the uncertainty of hadronization and underlying event contamination, and are easy to be calibrated. In this analysis $R = 0.4$ is used. After the jet clustering, the energy of jets with calorimeter in the EM scale is corrected to energy of hadron with response of hadron estimated with MC simulation[49].

4.1.1 B-jets

The jets from b-hadrons (b-jets) are tagged using information from ID. The tagging of b-jets are called b-tagging and boosted-decision-tree (BDT) based algorithm MV2c20 is used[50, 51] in the ATLAS. If a jet is associated with a track which is reconstructed with ID hits, the jet is evaluated with MV2c20 value threshold operating point. The operating point corresponds to the efficiency of 77% for truth b-jets. In this operating point, the rejection power (inverse of efficiency) for charm quark, light flavour quark, and τ -jet are expected to be approximately 5, 10 and 140 for each[51]. Since the tagging uses information from ID, b-tagging is applied for jets in the range $|\eta| < 2.5$.

4.1.2 Jet cleaning

For the rejection of non-collision jets and detector noise background, BadLoose and BadTight jet cleaning selections are applied[52]. In the BadLoose cleaning,

requirements for variables such as an energy fraction in the HEC is not large, an energy fraction in the EM calorimeter is not small, and an energy fraction in one layer is not large are applied. `BadLoose` selection is applied for all jets in the events. If at least one jet does not pass the selection, the event is vetoed. In the `BadTight` cleaning, a requirement for a variable such as an energy fraction of tracks from a primary vertex is not small is applied. `BadTight` selection is applied for the events with two leading jets which have $p_T > 100$ GeV. If the jets in an event don't pass the cleaning cut, the event is vetoed.

Selection	Description
Baseline jet	
Acceptance	$p_T > 20$ GeV & $ \eta < 2.8$
ID	Loose
Signal jet	
Acceptance	$p_T > 50$ GeV
B-jet	
Acceptance	$p_T > 50$ GeV & $ \eta < 2.5$
B-tagging	<code>MV2c20</code> working point with 77% efficiency

Table 5: The definitions for baseline jet, signal jet, and B-jet identification.

4.2 Electrons

The electron clusters are reconstructed with the information from EM calorimeter[53]. The seed clusters with energy > 2.5 GeV from 2nd layer cell unit (3×5 in $\eta \times \phi$) are formed by sliding window algorithm. If there are neighbouring clusters, the duplicated clusters are removed. This algorithm is also used in photon reconstruction (Sec.4.3). A cluster is identified as an electron, if there are at least one associating track which is reconstructed with the information from the ID ($|\eta| < 2.5$). A track is determined as best track, if the track is nearest to the cluster barycentre in the 2nd layer of the EM calorimeter.

For the identification of electron, likelihood based identification (ID) criteria[54] is applied. The variables, such as shower shape, measured in the EM calorimeter are used for the calculation of likelihood. Three levels of working point(Loose ID, Medium ID, and Tight ID) are prepared depending on the selection tightness.

For a baseline electron, $p_T > 10$ GeV and $|\eta| < 2.47$ acceptance cut, and loose ID selection is applied.

For a signal electron, significance of impact parameter requirement, $|d_0|/\sigma < 5$, longitudinal impact parameter requirement, $|z_0 \cdot \sin(\theta)| < 0.5$ mm, Tight likelihood based identification criteria, and an isolation requirement from the other particles are applied. This isolation selection uses the information about the p_T sum of tracks around the electron and/or transverse energy of clusters around an electron. In this analysis GradientLoose isolation working point (WP) is used. This isolation WP is likelihood based, and GradientLoose is defined to realize electron efficiency of

$$\varepsilon = (0.057 \cdot p_T [\text{GeV}] + 95.57)\% \text{ for } (25 \text{ GeV} < p_T < 60 \text{ GeV}), \quad (50)$$

where $\varepsilon = 95\%$ at p_T of 25 GeV and $\varepsilon = 99\%$ at p_T of 60 GeV.

The definitions of electron are summarized in Table 6.

Selection	Description
Baseline electron	
Acceptance	$p_T > 10 \text{ GeV} \ \& \ \eta < 2.47$
ID	Loose
Signal electron	
ID	Tight
Isolation	GradientLoose
Impact parameter	$ d_0 /\sigma < 5$ $ z_0 \cdot \sin(\theta) < 0.5 \text{ mm}$

Table 6: The definitions for baseline and signal electron identification.

4.3 Photons

The clustering method is the same as electrons (Sec.4.2). A photon is identified with using conversion information, identification (Sec.4.3.2), and isolation (Sec.4.3.3).

For a reconstructed photon, $p_T > 25$ GeV and acceptance, $|\eta| < 1.37 || 1.52 < |\eta| < 2.37$, are required. The range $1.37 < |\eta| < 1.52$ is removed, since the region has a crack region between barrel and end-cap calorimeters. The identification and isolation selection of photons are described in the following paragraphs.

The summary of photon definition is in Table 7.

Selection	Description
Baseline photon	
Acceptance	$p_T > 25 \text{ GeV} \ \& \ \eta < 1.37 1.52 < \eta < 2.37$
ID	Tight
Signal photon	
Acceptance	$p_T > 130 \text{ GeV}$
Isolation	Cone40

Table 7: The definitions for baseline and signal photon identification.

4.3.1 Photon conversion

If a vertex from one or two track matches to a photon cluster, the photon is reconstructed as converted photon, else the photon is reconstructed as unconverted photon.

4.3.2 Photon identification

The variables used for photon identification is described in Table 8. With these variables, two types of IDs, Tight and Loose, are determined. The definition of Loose and Tight photon ID are in Table 9 and Table 10 for each. The Tight ID selection includes the Loose ID selection.

Name	Description
Variables using the information in the first layer of the EM calorimeter (strip section)	
DeltaE	$:= E_{2nd\ max} - E_{min}$, where $E_{2nd\ max}$ is the energy of the 2nd maximum strip, and E_{min} is the energy in the strip which have minimum value between 1st and 2nd maximum strip.
Eratio	$:= (E_1 - E_2)/(E_1 + E_2)$, where E_1 is the energy of a strip with maximum energy and E_2 is the energy of a strip with 2nd maximum energy.
f1	$:= E_{all-strips}/E_{EM}$, where $E_{all-strips}$ is the energy in all strips in the cluster, and E_{EM} is the energy reconstructed in the EM calorimeter.
fracm	$\frac{E(\pm 3) - E(\pm 1)}{E(\pm 1)}$, where $E(\pm i)$ is the energy in $\pm i$ strips around the strip with maximum energy
weta1	Shower width in ± 1 strips around a strip with maximum energy.
wtot	Total lateral shower width in strips.
Variables using the information of the hadronic calorimeter	
$R_{had,1}$	$:= E_T^{had,1st}/E_T$, where $E_T^{had,1st}$ is E_T in the first layer of the hadronic calorimeter. This variable is only used in the range $ \eta < 0.8 \eta > 1.37$.
R_{had}	$:= E_T^{had,all}/E_T$, where $E_T^{had,all}$ is E_T of all the hadronic calorimeter. This variable is only used in the range $0.8 < \eta < 1.37$.
Variables using the information of energy in the second layer of the EM calorimeter	
e277	Energies in 7×7 ($\eta \times \phi$) cell window.
Reta	$:= e237/e277$, where e237 is the energies in 3×7 ($\eta \times \phi$) cell window. Reta is ratio of energies in η .
Rphi	$:= e233/e237$ (in ϕ), where e233 is the energies in 3×3 ($\eta \times \phi$) cell window. Rphi is ratio of energies in ϕ .
weta2	Width of shower (in η direction)

Table 8: Variables definitions used for photon identification cuts.

Name \ $ \eta $ range	0.0 ~ 0.6	~ 0.8	~ 1.15	~ 1.37	1.52 ~ 1.81	~ 2.01	~ 2.37
Rhad (for $ \eta < 0.8$ or $ \eta > 1.5$) >							
Rhad1 (for $0.8 < \eta < 1.5$) >	0.0606	0.05237	0.06482	0.04908	0.04788	0.06506	0.06201
e277 >	0.1						
Reta >	0.9175	0.9000	0.9109	0.8912	0.8922	0.9221	0.8903
weta2 <	0.0129	0.0142	0.0136	0.0139	0.0152	0.0128	0.0125

Table 9: Loose ID configuration. The cut values are given in the table for each $|\eta|$ range. These cuts are applied both converted and non-converted photons. Definitions of the variables are given in Table 8.

Name \ $ \eta $ range	conversion	0.0 ~ 0.6	~ 0.8	~ 1.15	~ 1.37	1.52 ~ 1.81	~ 2.01	~ 2.37
Rhad (for $ \eta < 0.8$ or $ \eta > 1.5$) >								
Rhad1 (for $0.8 < \eta < 1.5$) <	converted	0.01453	.01323	0.02954	0.03433	0.03132	0.02993	0.04377
	non-converted	0.030	0.030	0.035	0.02725	0.03073	0.05	0.03894
e277 >	both	0.1						
Reta >	converted	0.9206	0.9105	0.9118	0.9183	0.8938	0.09222	0.8930
	non-converted	0.9312	0.9008	0.9259	0.9206	0.9131	0.9238	0.9070
Rphi >	converted	0.5120	0.3760	0.5107	0.5365	0.5113	0.5397	0.470834
	non-converted	0.9	0.85	0.84	0.9020	0.9168	0.9	0.9
weta2 <	converted	0.0118	0.0142	0.0127	0.0134	0.0151	0.0127	0.0125
	non-converted	0.01189	0.01337	0.01112	0.01276	0.01300	0.01208	0.01251
f1 >	both	0.005						
DeltaE [MeV] <	converted	187.5	175	150	150	176.455	400	493.3
	non-converted	200	111.5	140	140	250	400	400
Eratio >	converted	0.827	0.857	0.835	0.790	0.842	0.850	0.80
	non-converted	0.830	0.854	0.839	0.783	0.896	0.820	0.840
wtot <	converted	3.481	3.513	3.303	3.214	3.909	3.354	2.232
	non-converted	3.12	3.20	3.10	2.92	3.00	3.68	2.15
fracm <	converted	0.3539	0.4203	0.5212	0.5958	0.5806	0.3822	0.2715
	non-converted	0.600	0.500	0.600	0.511	0.508	0.238	0.230
weta1 <	converted	0.7606	0.7256	0.7782	0.7823	0.7931	0.7707	0.6928
	non-converted	0.6671	0.7129	0.7207	0.7452	0.7489	0.6867	0.6339

Table 10: Tight ID configuration. The cut values are given in the table. The cut values are varied depending on conversion information and $|\eta|$ range. All the selections require Loose ID intrinsically. Definitions of the variables are given in Table 8.

4.3.3 Photon isolation

For the isolation, two types of variables are used, ptconeX and etconeX.

- ptconeX: The p_T sum of tracks in the defined cone around the photon. The tracks of the photon is excluded for the calculation,
- topoetconeX: The transverse energy sum of the topological clusters in the defined cone excluding the objective photon energy,

where X is 100 times value of the cone size (e.g. X=40 means conesize (ΔR)=0.4). From these variables, three types of isolation Working Points (WP) are prepared in the ATLAS experiment as in Table 11.

Working point name	topoetconeX based	ptconeX based
Cone40	topoetcone40 < 0.022 p_T + 2.45 (GeV)	ptcone20/ p_T < 0.05
Cone20	topoetcone20 < 0.065 p_T (GeV)	ptcone20/ p_T < 0.05
Cone40CaloOnly	topoetcone40 < 0.022 p_T + 2.45 (GeV)	-

Table 11: Isolation working points used in ATLAS experiments.

4.3.4 Efficiency and purity of photons

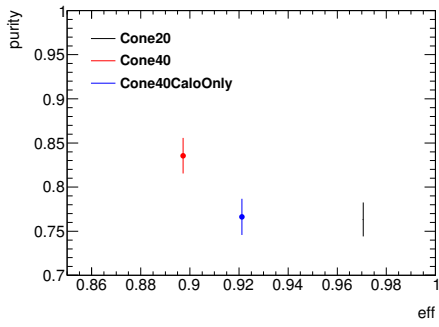
The efficiency and purity of photons for each WP are checked using MC samples. For the true(or signal) photon samples, γ +jets (SHERPA) is used. For the jet-to-photon fake (or background, BG) samples, PYTHIA multi-jets samples are used.

The definition of efficiency and purity are as follows:

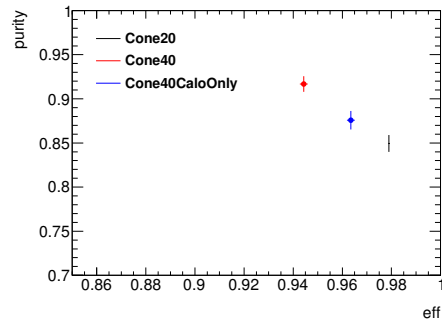
$$\text{Eff} = \frac{N_{\text{iso}}^{\text{Sig}}}{N_{\text{iso}}^{\text{Sig}} + N_{\text{non-iso}}^{\text{Sig}}}, \quad (51)$$

$$\text{Purity} = \frac{N_{\text{iso}}^{\text{Sig}}}{N_{\text{iso}}^{\text{Sig}} + N_{\text{iso}}^{\text{BG}}}. \quad (52)$$

For this study, all the Tight ID passed photons are used. The results of the performance is Figure 18. Since purity is important, Cone40 WP is used.



(a) Purity vs efficiency for photon $p_T > 130$ GeV.



(b) Purity vs efficiency for photon $p_T > 500$ GeV.

Figure 18: Purity vs efficiency performance for each WP. After the selection: one Tight ID photon and $N_{\text{jet}}(p_T > 50 \text{ GeV}) \geq 2$. The errors are MC statistical errors.

4.4 Muons

Muons are reconstructed with combining the information from inner detector and muon spectrometer[55]. A muon candidate is required to be $p_T > 10$ GeV and $|\eta| < 2.4$.

A baseline muon is required to pass Medium identification requirements[56]. This selection uses "stand-alone" muons, which the muon track is reconstructed only in muon spectrometer, and use "combined" muons, which the muon track is reconstructed both in muon spectrometer and inner detector. This selection uses the information of hits in each detector and momentum of muons. This selection is targeted to minimize the systematic uncertainties in calibration and reconstruction.

For a signal muon, significance of impact parameter requirement, $|d_0|/\sigma < 3$, longitudinal impact parameter requirement, $|z_0 \cdot \sin(\theta)| < 0.5$ mm, and isolation requirement from the other particles are applied. The isolation cut `GradientLoose` is the same definition as that of electrons which realize the efficiency of Eq 50.

The summary of muon definition is in Table 12.

Selection	Description
Baseline muon	
Acceptance	$p_T > 10$ GeV & $ \eta < 2.5$
ID	Medium
Signal Muon	
Acceptance	$p_T > 25$ GeV & $ \eta < 2.4$
Isolation	<code>GradientLoose</code>
Impact parameter	$ d_0 /\sigma < 3$
	$ z_0 \cdot \sin(\theta) < 0.5$ mm

Table 12: The definitions for baseline and signal muon identification.

4.5 Overlap removal

A cluster or track is assigned to be different objects. To remove these duplicated objects, overlap removal (OR) of objects is applied for baseline objects. In the regions where photons are not used, the procedure of OR is,

1. $e - \mu$ OR: If e and μ are reconstructed using same track, the electron is removed.
2. e -jet OR: If $\Delta R(e, \text{jet}) < 0.2$, the jet is removed.

3. jet- e OR: If $0.4 > \Delta R(e, \text{jet}) \geq 0.2$, the electron is removed.
4. μ -jet OR: If $\Delta R(\mu, \text{jet}) < 0.4$ for the jet with $N_{\text{track}} \leq 2$, the jet is removed.
5. jet- μ OR: If $\Delta R(\mu, \text{jet}) < 0.4$ for the jet with $N_{\text{track}} > 2$, the muon is removed.

In the regions where photons are used, additionally,

6. e - γ OR: If $\Delta R(\gamma, e) < 0.4$, the γ is removed.
7. μ - γ OR: If $\Delta R(\gamma, \mu) < 0.4$, the γ is removed.
8. γ -jet OR: If $\Delta R(\gamma, \text{jet}) < 0.4$, the jet is removed.

The validation study of γ -jet OR is described in Appendix A.1.

4.6 Missing transverse momentum

All the reconstructed and calibrated objects are used for $E_{\text{T}}^{\text{miss}}$ reconstruction[57]. The $E_{\text{T}}^{\text{miss}}$ is calculated from the vector sum of each component:

$$\vec{E}_{\text{T}}^{\text{miss}} = - \left(\sum_e \vec{p}_{\text{T}}^e + \sum_{\gamma} \vec{p}_{\text{T}}^{\gamma} + \sum_{\text{jets}} \vec{p}_{\text{T}}^{\text{jets}} + \sum_{\mu} \vec{p}_{\text{T}}^{\mu} + \sum_{\text{SoftTerm}} \vec{p}_{\text{T}}^{\text{SoftTerm}} \right). \quad (53)$$

The negative sum of \vec{p}_{T} for the calibrated electrons (e), photons (γ), muons (μ), and jets after overlap removal are used. The \vec{p}_{T} not associated to these objects but deposited in the detector is summed as "SoftTerm". In this analysis, Track Soft Term (TST) is used. The TST is calculated from tracks which are reconstructed with ID but are not associated with electrons, photons, muons or jets.

4.7 Triggers

The designed bunch crossing rate of the LHC is 40 MHz. The ATLAS trigger system is designed to record a few hundreds Hz events from the 40 MHz bunch crossing rate[58]. This is limited by the data processing or data storage capacity. For the reduction of rates, the trigger system selects the events with selected physics objects, e.g. electrons, muons, photons, jets(including b -jets, τ -jets) and $E_{\text{T}}^{\text{miss}}$.

The ATLAS trigger system consists with three levels of processing. The first level (L1) is the trigger with hardware which uses the information from calorimeter and muon detectors (RPCs and TGCs). The second level (L2) and the third (Event Filter, EF) are the triggers with software which use all the information from detectors. The L2 and EF are together called the High Level Trigger (HLT). With L1 trigger, approximately ~ 100 kHz rate events are selected and with HLT $\lesssim 1$ kHz rate events are selected.

4.7.1 Triggers used in this analysis

To select data events which is interesting for this analysis, the events which pass triggers are used. In this analysis "No lepton", "One lepton", "Two leptons", and "One photon" events are used as described in Chapter 5 and Chapter 6. The triggers dedicated for each event are used.

Electron trigger Two types of one-electron triggers are ORed, and used for "One lepton" and "Two leptons" events selection. The first trigger require electrons with Loose ID , isolated and $p_T^e > 24$ GeV. The latter trigger requires electrons with Medium ID and $p_T^e > 60$ GeV.

Muon trigger Two types of one-muon triggers are ORed, and used for "One lepton" and "Two leptons" events selection. The first trigger requires muons with Loose ID and $p_T^\mu > 20$ GeV. The latter trigger requires muons with $p_T^\mu > 50$ GeV.

Photon trigger One-photon trigger is used for "One photon" event selection. The trigger requires photons with Loose ID and $p_T^\gamma > 120$ GeV.

E_T^{miss} trigger E_T^{miss} trigger is used for "No lepton" event selection. The trigger requires an event with $E_T^{\text{miss}} > 70$ GeV. In order to get E_T^{miss} events whose efficiency for the E_T^{miss} trigger becomes $\simeq 1$, $E_T^{\text{miss}} > 200$ GeV is applied as off-line cut.

4.8 Event cleaning

For the rejection of detector noise background or events with mis-reconstructed, event cleaning cuts summarized in Table 13 are applied. Details are described in following paragraphs.

Jet cleaning: As described in Sec 4.1, BadLoose and BadTight jet cleaning is applied for all events.

Cosmic or fake muon veto: Fake muons are reconstructed when not-muon object hits the muon spectrometer or when tracks are mis-matched. Cosmic muons also make background events. Such events should be vetoed since the muons make large fake E_T^{miss} . Such muons are not from hard collision of protons and have large impact parameter. Therefore, the event is vetoed if muons after overlap removal have $|z_0| > 1$ mm & $|d_0| > 0.2$ mm remains.

The other cleaning related to muons is applied to reject the badly reconstructed muon events whose E_T^{miss} have large muon fraction. The veto condition is

$$\frac{E_T^{\text{miss}} \text{Muons}}{E_T^{\text{miss}}} \cdot \cos(\phi(E_T^{\text{miss}} \text{Muons}) - \phi(E_T^{\text{miss}})) > 0.5, \quad (54)$$

where $E_T^{\text{miss}} \text{Muons} = -\sum_{\mu} \vec{p}_T^{\mu}$ in Sec.4.6.

Number	Cleaning	Description of event veto condition
1	Jet cleaning	LooseBad jets with $p_T > 20$ GeV. TightBad leading two jets with $p_T > 100$ GeV.
2	Cosmic muon	Muons with $ z_0 > 1$ mm && $ d_0 > 0.2$ mm after overlap removal.
3	Bad muon	Events with $\frac{E_T^{\text{miss}} \text{Muons}}{E_T^{\text{miss}}} \cdot \cos(\phi(E_T^{\text{miss}} \text{Muons}) - \phi(E_T^{\text{miss}})) > 0.5$

Table 13: The summary table of cleaning.

5 Event selection and optimization

This chapter describes the event selection optimization. The selected region for searching signal events is called "signal region (SR)". In Sec.5.1, the discriminating variables which are also used in the previous analysis [59] are described. In addition to these variables, the "aplanarity" is introduced in this analysis and the studies related to aplanarity are described in Sec.5.2. With these variables, the final SR optimization is described in Sec.5.3.

5.1 Discriminating variables

- " N_{jet} " is number of jets with $p_{\text{T}}^{\text{jet}} > 50$ GeV. Compared to the SM backgrounds, N_{jet} tend to be large for signal events since gluinos are pair-produced and each gluino decays into $N_{\text{parton}} \geq 2$.
- " $E_{\text{T}}^{\text{miss}}$ " is the missing transverse momentum and defined in Sec.4.6. Since LSPs make large $E_{\text{T}}^{\text{miss}}$ events, requiring high $E_{\text{T}}^{\text{miss}}$ reduce the SM backgrounds. In some control regions for the background estimation described in Sec.6, a lepton (e , μ) or γ is added to $E_{\text{T}}^{\text{miss}}$ to reproduce the $E_{\text{T}}^{\text{miss}}$ behaviour of a Z boson which decays into two neutrinos. Such $E_{\text{T}}^{\text{miss}}$ is written as $E_{\text{T}}^{\text{miss}'}$.
- "Effective mass (m_{eff})" is defined as

$$m_{\text{eff}} = \sum_{i=1}^{N_{\text{jet}}} p_{\text{T}}^{\text{jet},i} + E_{\text{T}}^{\text{miss}}, \quad (55)$$

where scalar sum of jets with $p_{\text{T}} > 50$ GeV is used. This variable has strong correlation with the energy of produced objects and helps to select SUSY signal events.

- " $\min \Delta\phi(\text{jet}, E_{\text{T}}^{\text{miss}})$ " is the minimum azimuthal angle between jets and $E_{\text{T}}^{\text{miss}}$. The jets with $p_{\text{T}} > 50$ GeV are used for calculation of this variable. This variable has strong discriminating power to reduce fake $E_{\text{T}}^{\text{miss}}$ events from jet energy mismeasurements. This variable also reduces the events which have neutrinos from semi-leptonic decay of heavy flavour hadrons.
- " $E_{\text{T}}^{\text{miss}}/m_{\text{eff}}(N_{\text{jet}})$ " is the $E_{\text{T}}^{\text{miss}}$ to m_{eff} ratio. In this m_{eff} calculation, number of jets up to N_{jet} is considered. Since LSP does not exist in most of the SM processes, requiring large value of this variable reduces the SM backgrounds. This also reduces fake $E_{\text{T}}^{\text{miss}}$ events from jets mismeasurements. This variable also reduces the events which have neutrinos from semi-leptonic decay of heavy flavour hadrons.

- " $E_T^{\text{miss}}/\sqrt{H_T}$ " is the E_T^{miss} to H_T ratio, where $H_T = \sum_{i=1}^{N_{jet}} p_T^{jet,i}$. Since LSP does not exist in most of the SM processes, requiring large value of this variable also reduces the SM backgrounds. This also reduces fake E_T^{miss} events from jets mismeasurements since E_T^{miss} resolution is proportional to $\sqrt{H_T}$. This variable also reduces the events which have neutrinos from semi-leptonic decay of heavy flavour hadrons.

5.2 Study of aplanarity

Aplanarity[60] is introduced for $\tilde{g}-\tilde{g}$ production search in addition to the variables used in previous search [59]. Aplanarity is the variable which have the information that the jets event is whether 3D shape (neither planar nor linear) or not. The dominant BG processes of $\tilde{g}-\tilde{g}$ search is $Z(\rightarrow \nu\nu)+\text{jets}$ and the second dominant is $W(\rightarrow \ell\nu)+\text{jets}$. In these BG events, hadron jets are mainly produced in the opposite direction of the vector boson. Therefore, the shape of jets become linear or planar as shown in Figure 19(b). In contrast, for the $\tilde{g}-\tilde{g}$ production, the event shape become not-planar shape as shown in Figure 19(a). This is because

- The gluinos are produced in pair.
- The gluinos which we are searching for are heavy and are not boosted.
- Each gluino decays into three bodies ($\tilde{g} \rightarrow \tilde{\chi}_1^0 qq$).

Aplanarity is the variable which is sensitive to the differences.

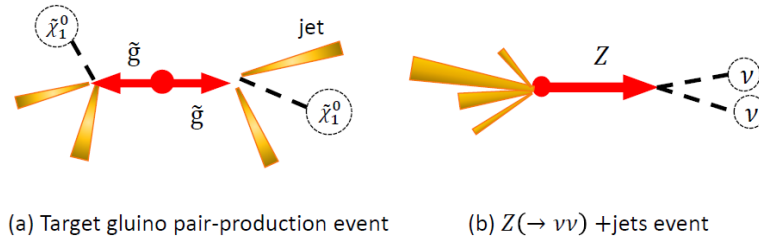


Figure 19: Conceptual figures of (a) signal and (b) background($Z(\rightarrow \nu\nu)+\text{jets}$) events.

In this section, some study of aplanarity is described. The definitions of event shape variables are in Sec.5.2.1 and Sec.5.2.2. The comparison of aplanarity with the other event shape variables are in Sec.5.2.3. The evaluation of jets systematics to aplanarity is described in Sec.5.2.4.

5.2.1 Definition of aplanarity, sphericity, and transverse sphericity[60]

Aplanarity was generally used to evaluate not-planar event shape. In this paper, aplanarity is derived from the momentum tensor of jets,

$$\sum_{i=1}^{N_{jets}} \begin{pmatrix} P_{ix}^2 & P_{ix}P_{iy} & P_{ix}P_{iz} \\ P_{iy}P_{ix} & P_{iy}^2 & P_{iy}P_{iz} \\ P_{iz}P_{ix} & P_{iz}P_{iy} & P_{iz}^2 \end{pmatrix} \quad (56)$$

The momentum tensor is diagonalized to,

$$\begin{pmatrix} \lambda_1 & 0 & 0 \\ 0 & \lambda_2 & 0 \\ 0 & 0 & \lambda_3 \end{pmatrix} \quad (57)$$

The λ s are normalized to be $\sum_{i=1}^3 \lambda_i = 1$, and named to be $\lambda_1 > \lambda_2 > \lambda_3$. In case $\lambda_1 \gg \lambda_2, \lambda_3$, the event shape is linear. In case $\lambda_1 > \lambda_2 \gg \lambda_3$, the event shape is planar. In case λ_3 is large, the event shape is neither linear nor planar. The definition and meaning of aplanarity, sphericity and transverse sphericity (S_T) are in Table 14.

name	definition	meaning
Aplanarity	$\frac{3}{2}\lambda_3$	Range is [0,0.5]. Aplanarity \rightarrow 0.5 means the event is not planar.
Sphericity	$\frac{3}{2}(\lambda_2 + \lambda_3)$	Range is [0,1]. Sphericity \rightarrow 1 means the event is not linear.
S_T	$2\frac{\lambda_2}{\lambda_1+\lambda_2}$	Range is [0,1]. $S_T \rightarrow$ 1 means the event is planar.

Table 14: Definition and meaning of variables

Safe aplanarity The definition of safe-aplanarity is similar to the aplanarity. The only difference is to divide the momentum tensor by the momentum of each jet:

$$\sum_{i=1}^{N_{jets}} \begin{pmatrix} P_{ix}^2 & P_{ix}P_{iy} & P_{ix}P_{iz} \\ P_{iy}P_{ix} & P_{iy}^2 & P_{iy}P_{iz} \\ P_{iz}P_{ix} & P_{iz}P_{iy} & P_{iz}^2 \end{pmatrix} / |P_i| \quad (58)$$

Though the first motivation to introduce this variable is for infra-red collinear safety of jet events, the jets clustered with the anti-kt algorithm is already collinear safe. Therefore this variable is considered only for the sensitivity comparison.

5.2.2 Thrust

Thrust and Transverse Thrust(T_t) [61] is the event shape variable to evaluate the non-linearity of events. The definition of thrust in this analysis is:

$$\text{Thrust} = 1 - \frac{\sum_{ijet} |\hat{T} \cdot \vec{p}_i|}{\sum_i |\vec{p}_i|}, \quad (59)$$

where \hat{T} is the direction which make the sum of projected jet momentum maximum. This variable is used to evaluate the event is linear or not. The event is linear in the limit of Thrust $\rightarrow 0$, and the difference from 0 means the event is not linear.

The definition of Transverse thrust in this analysis is

$$T_t = 1 - \max \frac{\sum_{ijet} |\vec{n}_t \cdot \vec{p}_{ti}|}{\sum_i |\vec{p}_{ti}|}, \quad (60)$$

where \vec{n}_t is the direction in transverse plane which makes the sum of projected jet p_T maximum. The event in the transverse plane is linear in the limit of $T_t \rightarrow 0$, and the difference from 0 means the event is not linear.

5.2.3 Comparison of event shape variables

In this section, six variables, including aplanarity, are studied in point of sensitivity.

MC samples

- Signal sample: gluino direct-decay simplified model, $m(\tilde{g}) = 1.6$ TeV and $m(\tilde{\chi}_1^0) = 250$ GeV, is used as a bench mark
- BG samples: $Z(\rightarrow \nu\nu)$ +jets, $W(\rightarrow l\nu)$ +jets, and $t\bar{t}$ samples are used

Pre-selection To compare the shape variables, 4 jets pre-selections (Table 15) are applied for the samples. This is because more than 3 quarks or gluons are produced from the signal.

Simple Optimization The simple common cut combination of some promising variables used in the previous search [59](Table 16) are used in addition to the shape variables. And the scanned cut values for each event shape variables are in Table 17. The optimization is executed by changing all the cut combinations to maximize the significance,

$$\text{Significance} = \frac{N_{\text{Signal}}}{\sqrt{N_{\text{BG}} + \sigma_{\text{stat}}^2 + (N_{\text{BG}}\sigma_{\text{sys}})^2}}, \quad (61)$$

variable	cuts
E_T^{miss} [GeV] >	250
$p_T(j_1)$ [GeV] >	130
$p_T(j_4)$ [GeV] >	60
$\Delta\phi(\text{jet}_{1,2,(3)}, \mathbf{E}_T^{\text{miss}})_{\text{min}}$ >	0.4
$\Delta\phi(\text{jet}_{i>3}, \mathbf{E}_T^{\text{miss}})_{\text{min}}$ >	0.2

Table 15: 4jets Pre-selection for the comparison of shape variables

where N_{Signal} and N_{BG} are number of signal and background events, σ_{stat} is MC statistical uncertainty, and σ_{syst} is overall systematic uncertainty on estimated background events. This significance is maximized under these conditions:

- $\sigma_{\text{syst}}/N_{\text{BG}} = 20\%$
- $N_{\text{Signal}} \geq 1$ and $N_{\text{BG}} \geq 1$
- Target integrated luminosity: $\int \text{Ldt} = 3.0 \text{ fb}^{-1}$

The first condition is from the typical error from previous analysis [59]. The second condition is to avoid the over-training with very tight cut and small number of events in CRs.

variable	scanned values
E_T^{miss} [GeV] >	[250,600] with 50 intervals
$m_{\text{eff}}(N_j \geq 4, p_T^{\text{jet}} > 60\text{GeV})[\text{TeV}] >$	[1.8, 2.8] with 0.2 intervals
$E_T^{\text{miss}}/m_{\text{eff}}(4_j) >$	0.00, 0.02, 0.05, 0.07, 0.10, 0.12, 0.15

Table 16: Common cut combination

The optimization results and the distributions of shape variables for signal and BGs, after pre-selections and all the other cuts, are in Table 18-23, and Figure 20-25. "After all the other cuts" means the all cuts are applied except for the cut of the plotted variable. Because of a E_T^{miss} cut, $E_T^{\text{miss}}/m_{\text{eff}}(4_j)$ is of no use.

Results The summary of significance for each shape variable is in Table 24. Among the variables aplanarity shows the best performance. Therefore, aplanarity is added to final optimization.

variable	scanned values
Aplanarity >	[0.02,0.10] with 0.02 intervals
Safe Aplanarity >	[0.01,0.10] with 0.01 intervals
Sphericity >	[0.02,0.30] with 0.02 intervals
S_T >	[0.02,0.30] with 0.02 intervals
Thrust >	[0.02,0.30] with 0.02 intervals
T_T >	[0.02,0.2] with 0.02 intervals

Table 17: Cut values for event shape variables

variable	cutvalue
Aplanarity >	0.04
E_T^{miss} [GeV] >	600
$m_{\text{eff}}(N_{j,p_T>60\text{GeV}} \geq 4)$ [TeV]>	2.6
$E_T^{\text{miss}}/m_{\text{eff}}(4_j)$ >	0.0

Table 18: Optimized cuts with using aplanarity.

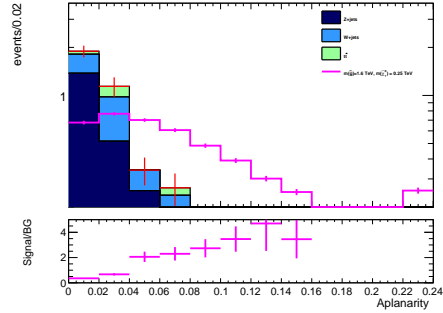


Figure 20: Aplanarity distribution after all the other cuts (including pre-selections). The (dark blue/blue/green) histogram shows ($Z(\rightarrow \nu\nu) + jets/W(\rightarrow \ell\nu) + jets/t\bar{t}$) BG processes. The (red/magenta) line shows the (SM total/signal) histogram. The lower pad shows the signal to BG ratio of number of events per bin.

variable	cutvalue
Safe aplanarity >	0.09
E_T^{miss} [GeV] >	450
$m_{\text{eff}}(N_{j,pT>60\text{GeV}} \geq 4)$ [TeV]>	2.4
$E_T^{\text{miss}}/m_{\text{eff}}(4_j)$ >	0.0

Table 19: Optimized cuts with using safe aplanarity.

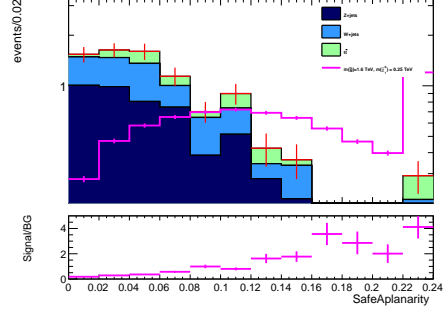


Figure 21: Safe aplanarity distribution after all the other cuts.

variable	cutvalue
Sphericity >	0.2
E_T^{miss} [GeV] >	500
$m_{\text{eff}}(N_{j,pT>60\text{GeV}} \geq 4)$ [TeV]>	2.4
$E_T^{\text{miss}}/m_{\text{eff}}(4_j)$ >	0.0

Table 20: Optimized cuts with using sphericity.

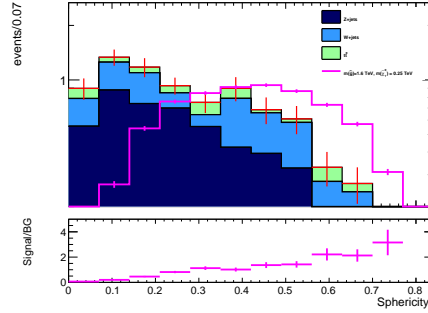


Figure 22: Sphericity distribution after all the other cuts.

variable	cutvalue
S_T >	0.18
E_T^{miss} [GeV] >	600
$m_{\text{eff}}(N_{j,pT>60\text{GeV}} \geq 4)$ [TeV]>	2.6
$E_T^{\text{miss}}/m_{\text{eff}}(4_j)$ >	0.0

Table 21: Optimized cuts with using S_T .

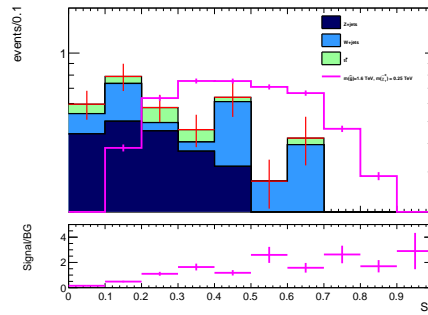


Figure 23: S_T distribution after all the other cuts.

variable	cutvalue
Thrust >	0.22
E_T^{miss} [GeV] >	550
$m_{\text{eff}}(N_{j, p_T > 60 \text{ GeV}} \geq 4)$ [TeV] >	2.6
$E_T^{\text{miss}} / m_{\text{eff}}(4_j)$ >	0.0

Table 22: Optimized cuts with using thrust.

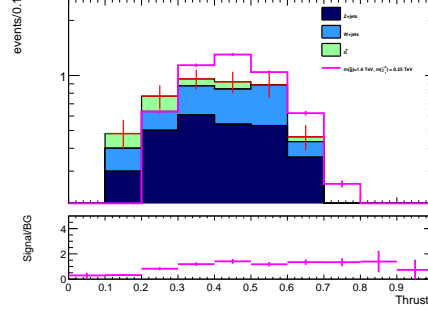


Figure 24: Thrust distribution after all the other cuts.

variable	cutvalue
T_T >	0.14
E_T^{miss} [GeV] >	600
$m_{\text{eff}}(N_{j, p_T > 60 \text{ GeV}} \geq 4)$ [TeV] >	2.6
$E_T^{\text{miss}} / m_{\text{eff}}(4_j)$ >	0.0

Table 23: Optimized cuts with using T_T .

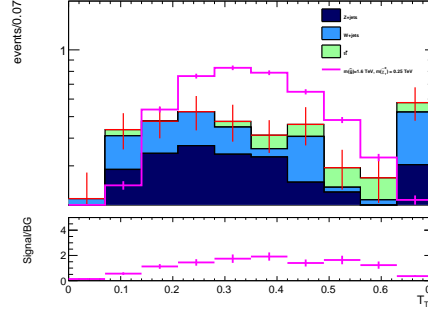


Figure 25: T_T distribution after all the other cuts.

variable	cut value	significance	N_{Signal}	N_{BG}
Aplanarity	> 0.04	$3.0^{+0.18}_{-0.15}$	3.42 ± 0.04	1.22 ± 0.13
Safe aplanarity	> 0.09	$2.66^{+0.12}_{-0.11}$	5.02 ± 0.04	3.09 ± 0.24
Sphericity	> 0.2	$2.43^{+0.09}_{-0.08}$	6.16 ± 0.05	5.2 ± 0.3
S_T	> 0.18	$2.37^{+0.10}_{-0.09}$	4.47 ± 0.04	3.12 ± 0.23
T_T	> 0.14	$2.16^{+0.08}_{-0.07}$	4.59 ± 0.04	3.83 ± 0.25
Thrust	> 0.22	$2.14^{+0.08}_{-0.07}$	4.98 ± 0.04	4.51 ± 0.28

Table 24: Significance of shape variables. The variables are sorted in descending order of significance. The errors show the statistical error on the MC samples.

5.2.4 Jets Systematic effects for aplanarity

In this section, the jets systematic effects for aplanarity are studied in comparison with number of jets selection(6-jets) which shows the best performance for large $m(\tilde{g})$ and small $m(\tilde{\chi}_1^0)$ region in Run1 search. It can be suspected that aplanarity is strongly affected by jets systematics, since aplanarity reflects the arrangement of jets. In such case, the sensitivity for signal events become worse, even though aplanarity have the discriminant power. Therefore, this study is very important.

Selections for the study 6jet region ($N_{jet} \geq 6, p_T^{jet} > 60$ GeV) is prepared to compare the systematic effects, since 6jet region showed the best sensitivity for the target signal in previous search [59]. The optimization method is the same as in the Sec. 5.2.3. For the 6 jets selection, $E_T^{miss}/m_{eff}(6_j)$ cut is used instead of E_T^{miss} for following the previous search. And the optimized selections are shown in Table 25.

varriable	4jet+aplanarity	6jet
$N_{jet}(p_T > 60 \text{ GeV}) \geq$	4	6
$E_T^{miss} [\text{GeV}] >$	600	-
$m_{eff}(p_T^{jet} > 60 \text{ GeV})[\text{TeV}] >$	2.6	2.4
Aplanarity >	0.04	-
$E_T^{miss}/m_{eff}(6_j) >$	-	0.15

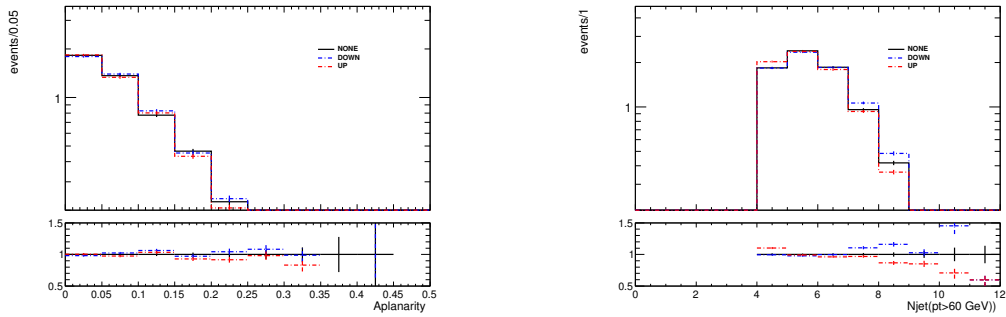
Table 25: Selections of 4jet+aplanarity region and 6jet region for the study.

Uncertainties used for the study The used MC sample are the same as the study in Sec.5.2.3. To evaluate the jet related systematic effects, these 5 components of jet systematics are considered.

- Theory uncertainty
 - ISR : Initial state radiation (ISR) uncertainty. The nominal scale for the first emission in MLM matching in MADGRAPH is multiplied by factors of 0.5 and 2.0.
 - FSR : Final state radiation (FSR) uncertainty. The nominal Λ value used in running α_s is multiplied by factors of 0.5 and 2.0.
 - Scale: The nominal values used for the variation of the factorization and renormalization scales are multiplied by factors of 0.5 and 2.0.

- ME-PS matching: The nominal jet matching scale to separate the parton generation in Matrix-Element (ME) and Parton Shower (PS) is multiplied by factors of 0.5 and 2.0.
- experimental uncertainty
 - JES : The Jet Energy Scale (JES) uncertainty. This arises from the comparison of jets from data and MC. In run1, the uncertainty is about 1.5% (This value is justified as in Figure 58) for jet p_T about 60 GeV. Jet p_T is scaled by $100 \pm 1.5\%$ to evaluate this uncertainty simply.

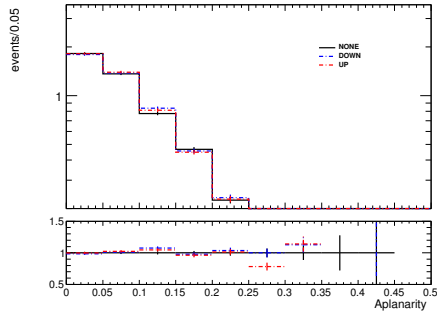
The distributions of aplanarity and N_{jet} after all the other cuts for each region are in figure 27-30.



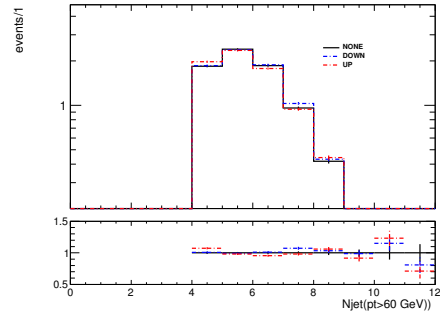
(a) Aplanarity distributions after all the other cuts of 4jet region.

(b) N_{jet} distributions after all the other cuts of 6jet region.

Figure 26: Aplanarity and N_{jet} distributions for ISR systematic variations. (Black/Blue/Red) solid lines show (nominal/scale-down/scale-up) variation.

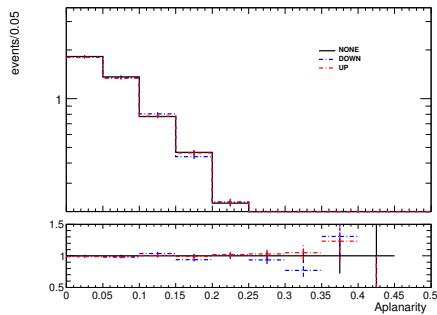


(a) Aplanarity distributions after all the other cuts of 4jet region.

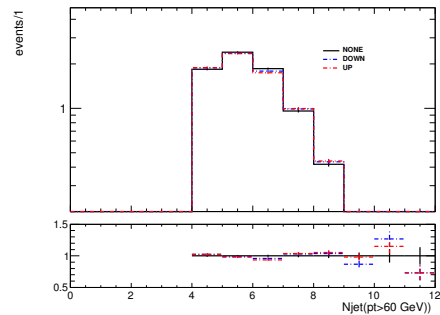


(b) N_{jet} distributions after all the other cuts of 6jet region.

Figure 27: Aplanarity and N_{jet} distributions for FSR systematic variations. (Black/Blue/Red) solid lines show (nominal/scale-down/scale-up) variation.

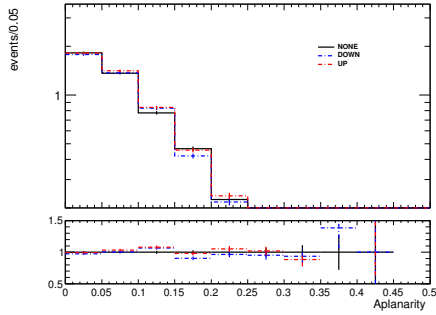


(a) Aplanarity distributions after all the other cuts of 4jet region.

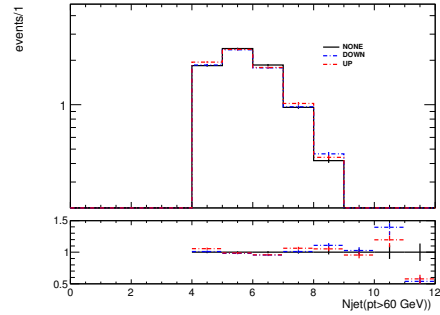


(b) N_{jet} distributions after all the other cuts of 6jet region.

Figure 28: Aplanarity and N_{jet} distributions for Scale systematic variations. (Black/Blue/Red) solid lines show (nominal/scale-down/scale-up) variation.

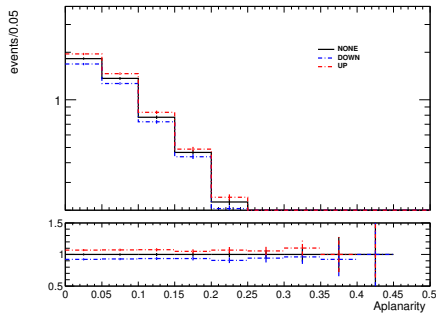


(a) Aplanarity distributions after all the other cuts of 4jet region.

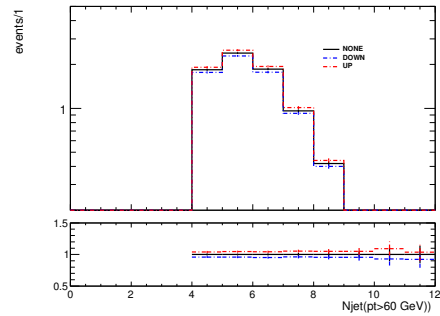


(b) N_{jet} distributions after all the other cuts of 6jet region.

Figure 29: Aplanarity and N_{jet} distributions for ME-PS matching systematic variations. (Black/Blue/Red) solid lines show (nominal/scale-down/scale-up) variation.



(a) Aplanarity distributions after all the other cuts of 4jet region.



(b) N_{jet} distributions after all the other cuts of 6jet region.

Figure 30: Aplanarity and N_{jet} distributions for JES systematic variations. (Black/Blue/Red) solid lines show (nominal/scale-down/scale-up) variation.

Results The systematic effects for aplanarity and N_{jet} are summarized in Table 26. Except for a JES systematic, all the systematic effects for aplanarity are small compared to $N_{\text{jet}} \geq 6$ selection. In total, the systematic uncertainty effects with aplanarity cut is comparable to N_{jet} selection.

The large JES systematic effect for 4jet region is strangely large. From the definition as written in 5.2.1, the scale of eigenvalue is normalized to calculate aplanarity. In fact, this JES effects are from E_T^{miss} . The Figure 31(a) shows the JES systematic effects only after the $N_{\text{jet}} \geq 4$. The systematic uncertainty effect is summarized in Table 27. Then, the systematic uncertainty from JES for aplanarity cut is very small compared to N_{jet} selection.

component	4jets+aplanarity	6jets
ISR	+2.9% -1.7%	+4.7% -5.9%
FSR	+2.9% -0.0%	+2.5% -2.5%
Scale	+0.0% -1.0%	+0.0% -1.6%
ME-PS matching	+0.4% -0.0%	+0.05% -0.8%
JES	+7.0% -6.8%	+4.9% -4.6%
Total uncertainty	8.1 % -7.1 %	7.2 % -8.1 %

Table 26: Summary of the systematic effects for 4jets region and 6jet region.

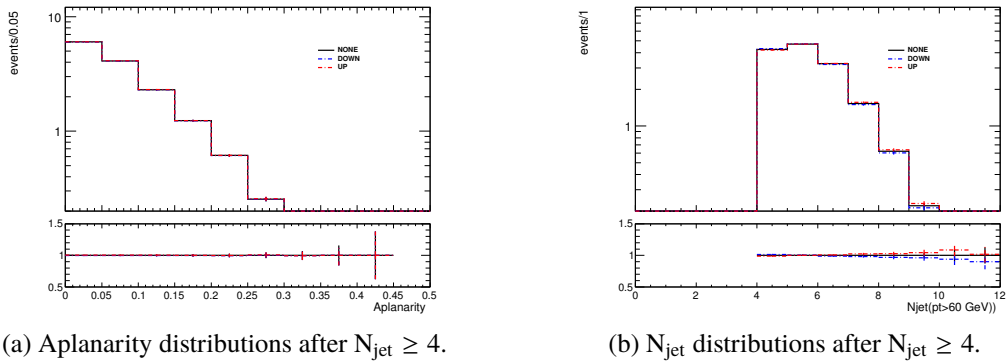


Figure 31: Aplanarity and N_{jet} distributions for JES systematic variations. (Black/Blue/Red) solid lines show (nominal/scale-down/scale-up) variation.

component	4jets+aplanarity	6jets
JES	+0.25% -0.25%	+1.5% -1.8%

Table 27: JES variation effects for 4jet region and 6jet region only after the $N_{\text{jet}} \geq 4$ cut.

5.3 Optimization procedure

The overview of the procedure is

1. Optimize with TMVA for all the signal points (TMVA is described in Appendix B)
2. Select some signal points to determine signal regions
3. Determine cuts with distribution after all the other cuts

This optimization is dedicated for the 3σ reach of $\tilde{g}-\tilde{g}$ signal. For the optimization, all the SM Monte Carlo samples described in Sec. 3.2 are used. The definition of the significance used in the optimization is described in Sec. 5.3.1.

5.3.1 Definition of significance

If the number of events is not small the very simple significance (Z) can be used, as

$$Z = \frac{n_{\text{sig}}}{\sqrt{n_{\text{BG}} + (\sigma_{\text{BG}})^2}}, \quad (62)$$

where n_{sig} and n_{BG} are number of signal and background events, and σ_{BG} is the uncertainty of the background estimation. However, this significance is derived with approximation that n_{BG} and n_{sig} are not small. In my analysis, the SRs are determined to make the BG events small. In such case, the alternative evaluation method is needed.

Therefore in this analysis, the other simple way to evaluate Z which is introduced in [62] is used. This is a solution for frequentist to the problem that a measurement of the number of events in SR and a measurement of the number of events in the control region (CR) to estimate the number of events in SR. In SR, the measurement x distributed as Poisson around $n_{\text{sig}} + n_{\text{BG}}$. The estimated events from CR y distributed as Poisson around $\tau \cdot n_{\text{BG}}$, where $\tau = \frac{n_{\text{BG}}}{\sigma_{\text{BG}}^2}$, and uncertainty in BG estimation is taken into account with τ . In summary, the probability density function (p.d.f) become,

$$P(x, y | n_{\text{sig}} + n_{\text{BG}}, \tau) = \text{Pois}(x | n_{\text{sig}} + n_{\text{BG}}) \cdot \text{Pois}(y | \tau n_{\text{BG}}) \quad (63)$$

From this, the p -value is calculated as

$$p = \frac{B\left(\frac{1}{1+\tau}, n_{\text{sig}} + n_{\text{BG}}, 1 + n_{\text{BG}} \cdot \tau\right)}{B\left(n_{\text{sig}} + n_{\text{BG}}, 1 + n_{\text{BG}} \cdot \tau\right)}, \quad (64)$$

where B of numerator is a incomplete beta function and of denominator is beta function. Then the significance (Z) is evaluated with the a one-tailed test of Gaussian distribution,

$$Z = \sqrt{2}\text{erf}^{-1}(1 - 2p), \quad (65)$$

where erf is the error function. Thanks to the appropriate treatment of estimated n_{BG} with Poisson p.d.f, the evaluation of Z become much realistic for the measurement of small number of events compared to Eq.62.

Conditions in calculating significance The conditions for calculating significance is as follows,

- $\sigma_{BG}/N_{BG} = 30\%$
- $N_{\text{Signal}} \geq 1$ and $N_{BG} \geq 1$
- Target integrated luminosity: $\int Ldt = 3.0 \text{ fb}^{-1}$

The first condition is from the typical error from previous analysis [59]. The second condition is to avoid the over-training with very tight cut and small number of events in CRs.

5.3.2 Optimization with TMVA

The details of the Genetic Algorithm (GA) in TMVA[63] is described in Appendix. B. Pre-selections for input samples of BGs and signals are in Table 28. For the five Njet cuts regions ($N=[2,6]$), the optimization method is applied after the pre-selection. The variables used in optimization are in Table 29.

variable	condition
number of lepton ==	0
\vec{E}_T^{miss} [GeV] >	200
$p_T^{\text{jet}_{1st}}$ [GeV] >	200
$\min \Delta\phi(\text{jet}_{1,2,(3)}, \vec{E}_T^{\text{miss}})$ >	0.4
$\min \Delta\phi(\text{jet}_{i>3}, \vec{E}_T^{\text{miss}})$ >	0.2
number of jet ($p_T > 50 \text{ GeV}$) [GeV] \geq	N

Table 28: Pre-selection for the Njet region.

variable
\vec{E}_T^{miss}
$p_T^{\text{jet}}{}_{1st}$
$p_T^{\text{jet}}{}_{2nd}$
$p_T^{\text{jet}}{}_{3rd}$
$p_T^{\text{jet}}{}_{4th}$
$m_{\text{eff}}(p_T^{\text{jet}} > 50\text{GeV})$
Aplanarity
$E_T^{\text{miss}}/m_{\text{eff}}(N_j)$ or $E_T^{\text{miss}}/\sqrt{H_T}$
Only in 2jet region
$\Delta\phi(\text{jet}_{1,2,(3)}, E_T^{\text{miss}})_{\text{min}}$
$\Delta\phi(\text{jet}_{i>3}, E_T^{\text{miss}})_{\text{min}}$

Table 29: Scanned variables for optimization.

5.3.3 Results of optimization with TMVA

The 3σ sensitivity reaches with the best optimized cuts for each signal point are in Figure 32. From the gluino direct-decay models(Figure 32(a)), three typical points are selected for final signal region. From the gluino onestep-decay models(Figure 32(b)), one typical point is selected for final signal region.

For the different signal models, four points near the 3σ -reach line are selected (Table 30). The resultant cuts from the raw outputs of TMVA are summarized in Table 31.

5.3.4 Distribution check with TMVA results

The distribution after all the other cuts are checked to avoid :

1. the local minimum of TMVA optimization
2. the meaningless cut which is already applied intrinsically after the other cuts.
If this cut remains, it would become difficult to get enough events in loosened control regions which are used in background estimation (Chapter 6)

As an example, the distributions for SR4jL after all the other cuts are shown in Figure 33, and 34. For each variable, dedicated check is done in point of S/B enhancement, as follows.

SR name	signal points	description
SR4jL	$(m(\tilde{g}), m(\tilde{\chi}_1^0)) = (1400, 200)$ (GeV)	Glauino direct-decay model. This point is selected as a typical point of large mass gap sample. This mass relation is similar to the typical SUSY-model like mSUGRA and AMSB.
SR4jM	$(m(\tilde{g}), m(\tilde{\chi}_1^0)) = (1200, 600)$ (GeV)	Glauino direct-decay model. This point is selected as a typical point of middle mass gap sample.
SR2jC	$(m(\tilde{g}), m(\tilde{\chi}_1^0)) = (812, 787)$ (GeV)	Glauino direct-decay model. This point is selected as a typical point of compressed mass sample. Since the mass gap is small, the N_{jet} cannot be high. Therefore, 2jet region shows highest sensitivity.
SR6jL	$(m(\tilde{g}), m(\tilde{\chi}_1^\pm), m(\tilde{\chi}_1^0)) = (1385, 705, 25)$ (GeV)	Glauino one-step-decay model. This point is selected as a typical point of large mass gap sample. Since the decay-chain is long, N_{jet} become high. Therefore, 6jet region shows highest sensitivity.

Table 30: The selected mass points on the 3σ reach. Descriptions for each signal mass points are described.

1. Aplanarity : aplanarity > 0.03 cut is chosen.
2. E_T^{miss} : $E_T^{\text{miss}} > 470$ GeV cut is chosen.
3. m_{eff} : $m_{\text{eff}} > 2000$. GeV is chosen.
4. $p_T^{\text{jet}}{}_{1st}$: No $p_T^{\text{jet}}{}_{1st}$ cut is applied, since the cut is already applied intrinsically by the other cuts.
5. $p_T^{\text{jet}}{}_{2nd}$: No $p_T^{\text{jet}}{}_{2nd}$ cut is applied, since the cut is already applied intrinsically by the other cuts.
6. $p_T^{\text{jet}}{}_{3rd}$: No $p_T^{\text{jet}}{}_{3rd}$ cut is applied, since the cut doesn't have significant effects.
7. $p_T^{\text{jet}}{}_{4th}$: No $p_T^{\text{jet}}{}_{4th}$ cut is applied, since the cut doesn't have significant effects.
8. $E_T^{\text{miss}}/m_{\text{eff}}(Nj = 4)$: No $E_T^{\text{miss}}/m_{\text{eff}}(Nj = 4)$ cut is applied, since the cut is already applied intrinsically by the other cuts.

variable	cut values			
Region	SR2jC	SR4jL	SR4JM	SR6jL
E_T^{miss} [GeV] >	800	470.5	485.7	269.1
$p_T^{\text{jet}}_{1st}$ [GeV] >	750.0	273.8	200.	218.4
$p_T^{\text{jet}}_{2nd}$ [GeV] >	50.0	84.5	138.5	210.7
$p_T^{\text{jet}}_{3rd}$ [GeV] >	-	56.4	55.9	106.3
$p_T^{\text{jet}}_{4th}$ [GeV] >	-	83.9	90.3	142.1
$m_{\text{eff}}(\text{incl.})$ [GeV] >	1900.	1948.5	1363.7	1776.4
Aplanarity	0.	0.020	0.039	0.066
$E_T^{\text{miss}}/m_{\text{eff}}(N_j)$	0.25	0.	0.	0.07
Only optimized in 2jet region				
$\min \Delta\phi(\text{jet}_{1,2,(3)}, \mathbf{E}_T^{\text{miss}})$	0.4			
$\min \Delta\phi(\text{jet}_{i>3}, \mathbf{E}_T^{\text{miss}})$	0.2			

Table 31: The raw result of TMVA cut optimization.

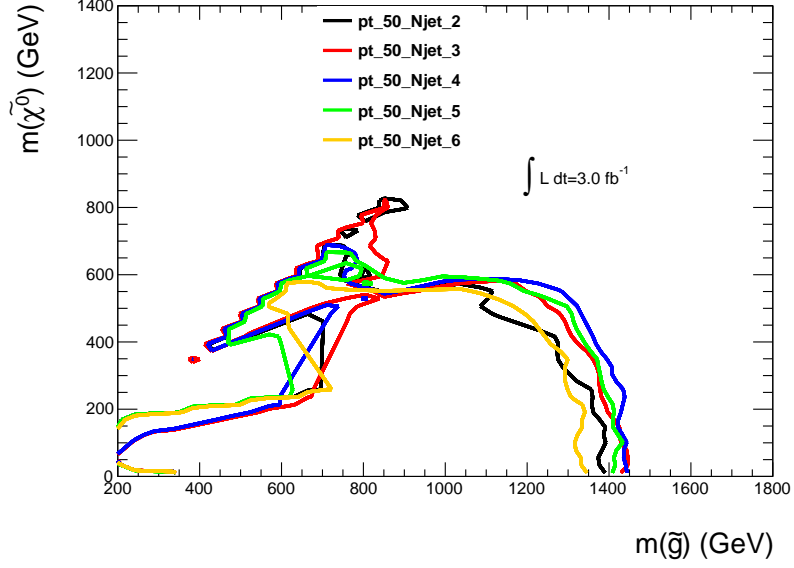
9. $\Delta\phi(\text{jet}_{1,2,(3)}, \mathbf{E}_T^{\text{miss}})$: $\Delta\phi(\text{jet}_{1,2,(3)}, \mathbf{E}_T^{\text{miss}}) > 0.4$ is applied to reduce multi-jets backgrounds.
10. $\min \Delta\phi(\text{jet}_{i>3}, \mathbf{E}_T^{\text{miss}})$: $\min \Delta\phi(\text{jet}_{i>3}, \mathbf{E}_T^{\text{miss}}) > 0.2$ is applied to reduce multi-jets backgrounds.

5.3.5 The optimized SRs

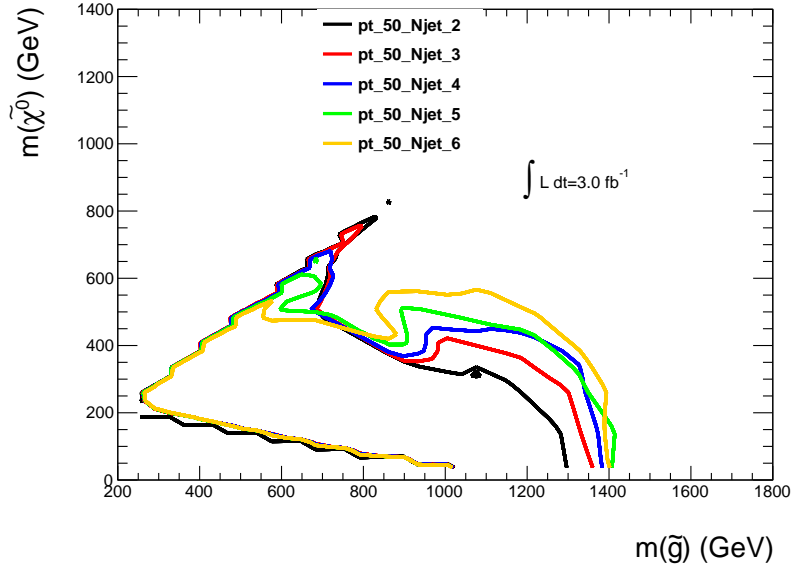
In real event selection with data, some selections related to data acquisition is applied (e.g. trigger and cleaning). A baseline selection including such selection is summarized in Table 32. The final SRs definitions after the baseline selection are determined as in Table 33. The MC expected distributions of variables in all SRs after all the other cuts are in Figure 35-38, and it can be seen that the final cuts effectively select signal events.

selection	description
cleaning	cleaning cuts described in Section 4.8
trigger	E_T^{miss} trigger
$E_T^{\text{miss}} >$	200 GeV
$p_T^{\text{jet}}{}_{1st} >$	200 GeV
$p_T^{\text{jet}}{}_{2nd} >$	50 GeV

Table 32: Baseline selection for SR event selection.



(a) $\tilde{g}\tilde{g} \rightarrow q\bar{q}q\bar{q}\tilde{\chi}_1^0\tilde{\chi}_1^0$ samples.



(b) $\tilde{g}\tilde{g} \rightarrow q\bar{q}q\bar{q}\tilde{\chi}_1^+\tilde{\chi}_1^- \rightarrow q\bar{q}q\bar{q}W^\pm W^\pm\tilde{\chi}_1^0\tilde{\chi}_1^0$ ($m(\tilde{\chi}_1^\pm) = (m(\tilde{g}) + m(\tilde{\chi}_1^0))/2$) samples.

Figure 32: Expected 3σ sensitivity reach with $\int Ldt = 3.0\text{fb}^{-1}$. The cuts are optimized for each signal point. (Black/Red/Blue/Green/Orange) solid lines show the reach for (2/3/4/5/6)jet region.

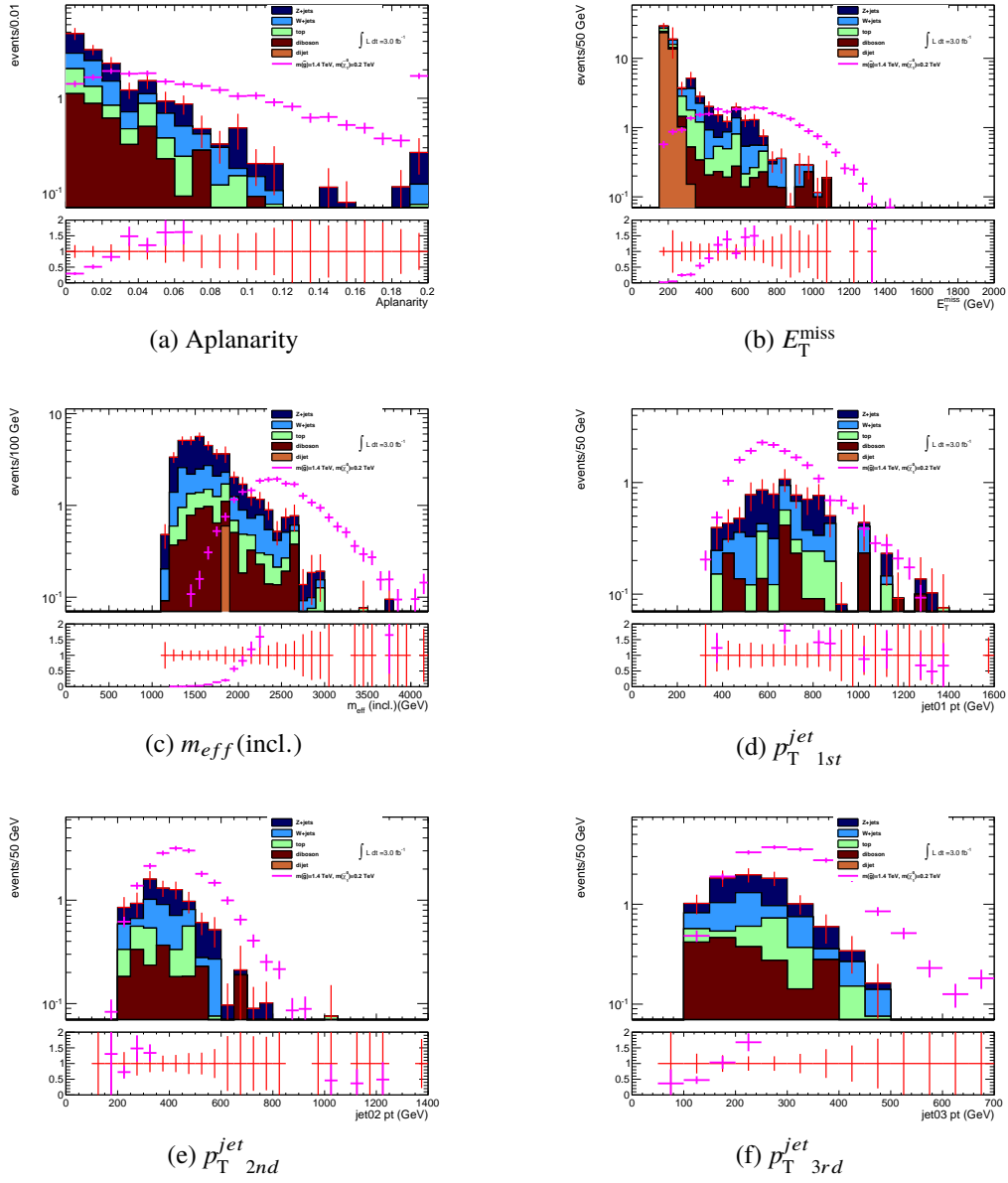


Figure 33: Distributions of variables after all the other cuts. $\int L dt = 3.0 \text{ fb}^{-1}$. The lower pad shows the ratio of signal events to background events.

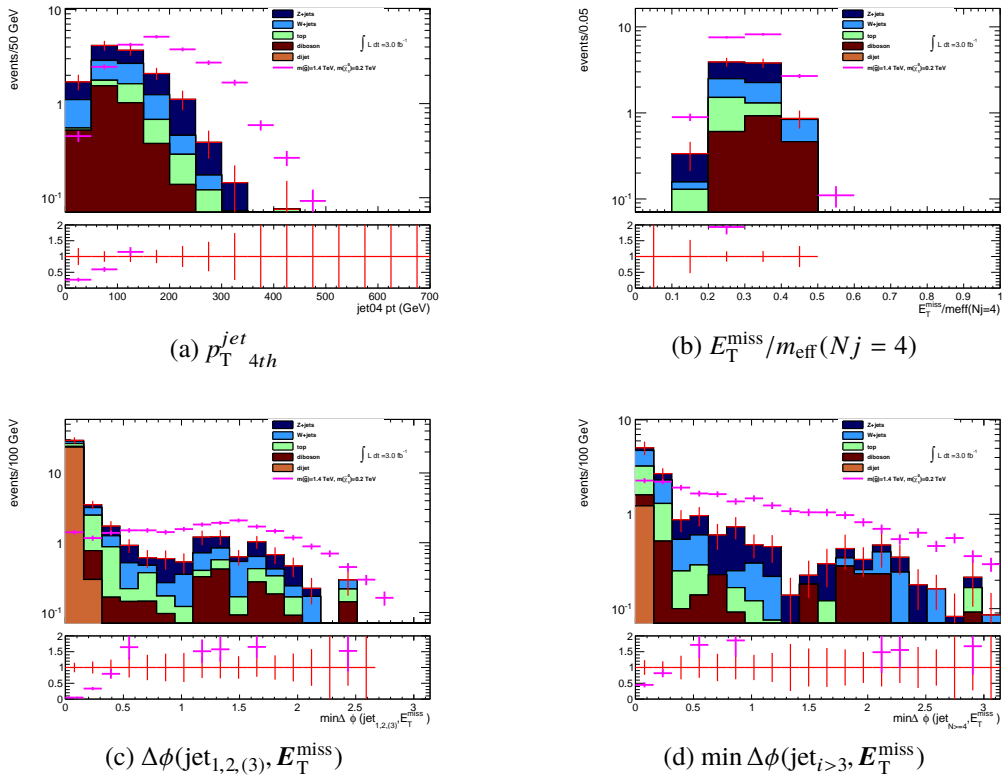


Figure 34: Distributions of variables after all the other cuts. $\int L dt = 3.0 \text{ fb}^{-1}$. The lower pad shows the ratio of signal events to background events.

	SR2jC	SR4jL	SR4jM	SR6jL
$N_{jet}(p_T > 50 \text{ GeV}) \geq$	2	4	4	6
$E_T^{\text{miss}} [\text{GeV}] >$	800.	470.	450.	400
Aplanarity $>$	-	0.03	0.07	0.07
$m_{\text{eff}}(\text{incl.}) [\text{GeV}] >$	1900	2000	1600	1850
$\min \Delta\phi(\text{jet}_{1,2,(3)}, \mathbf{E}_T^{\text{miss}}) >$	0.4			
$\min \Delta\phi(\text{jet}_{i>3}, \mathbf{E}_T^{\text{miss}}) >$	-	0.2		
Target signal	$(m(\tilde{g}), m(\tilde{\chi}_1^0)) = (812, 787) [\text{GeV}]$	$(m(\tilde{g}), m(\tilde{\chi}_1^0)) = (1400, 200) [\text{GeV}]$	$(m(\tilde{g}), m(\tilde{\chi}_1^0)) = (1200, 600) [\text{GeV}]$	$(m(\tilde{g}), m(\tilde{\chi}_1^\pm), m(\tilde{\chi}_1^0)) = (1385, 705, 25) [\text{GeV}]$

Table 33: The selection criteria for each singal region.

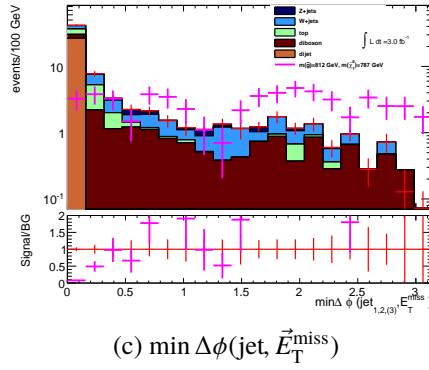
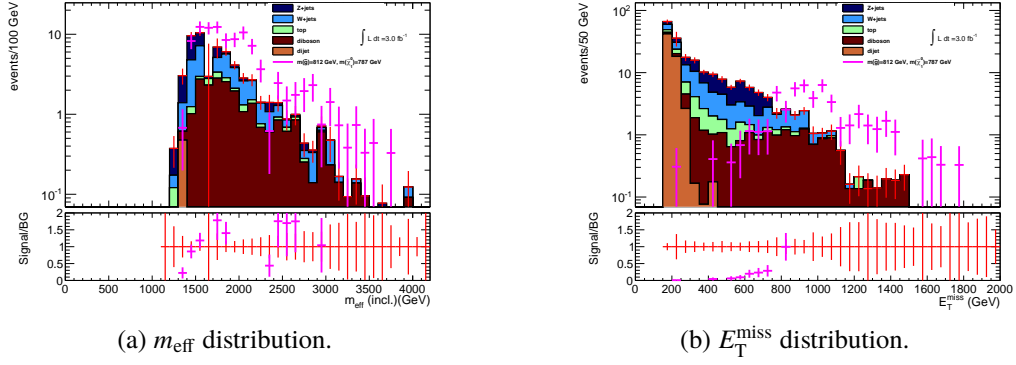
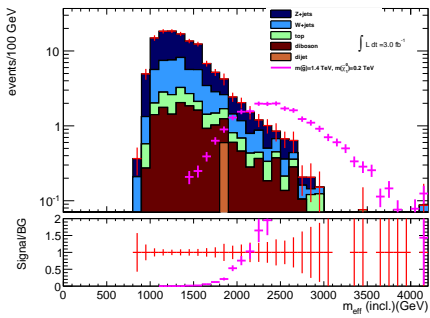
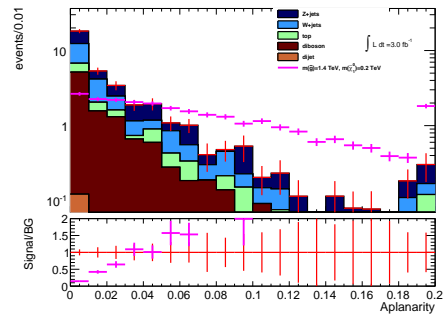


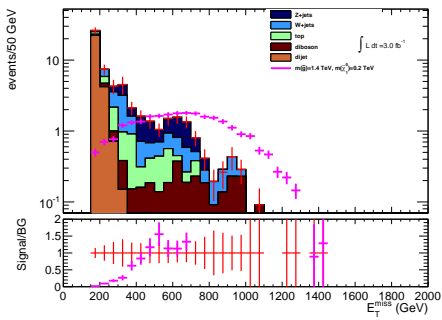
Figure 35: Distributions of each variable used in SR2jC after all the other cuts. Signal sample is the gluino direct-decay model : $(m(\tilde{g}), m(\tilde{\chi}_1^0)) = (812, 787)$ [GeV]. The lower pad shows ratio of signal events to background events.



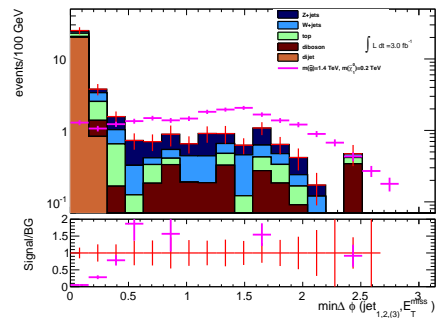
(a) m_{eff} distribution.



(b) Aplanarity distribution.

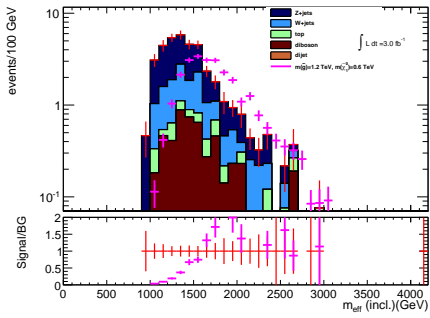


(c) E_T^{miss} distribution.

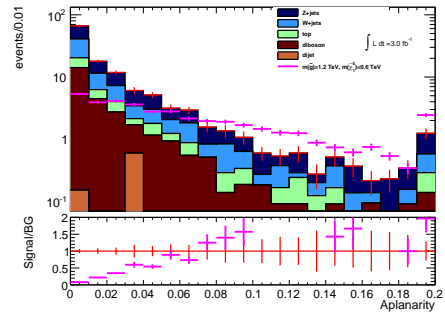


(d) $\min \Delta \phi (\text{jet}, \vec{E}_T^{\text{miss}})$ distribution.

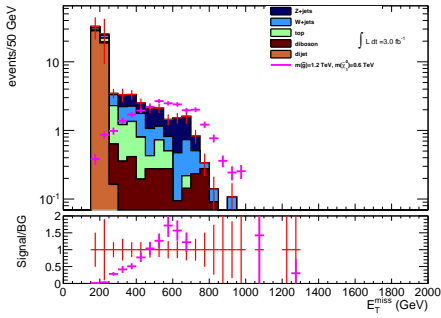
Figure 36: Distributions of each variable used in SR4jL after all the other cuts. Signal sample is the gluino direct-decay model : $(m(\tilde{g}), m(\tilde{\chi}_1^0)) = (1400, 200) [\text{GeV}]$. The lower pad shows ratio of signal events to background events.



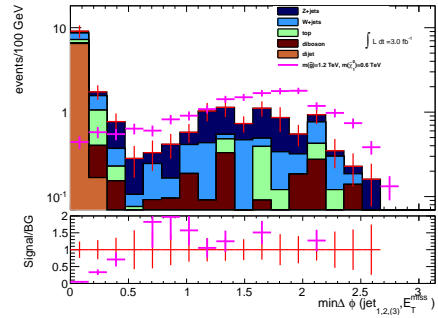
(a) m_{eff} distribution.



(b) Aplanarity distribution.

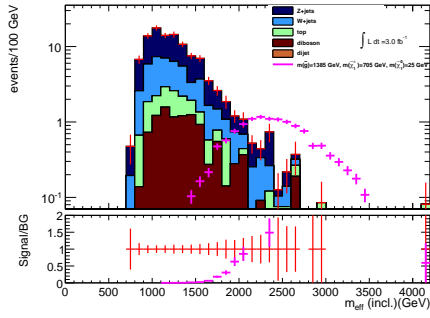


(c) E_T^{miss} distribution.

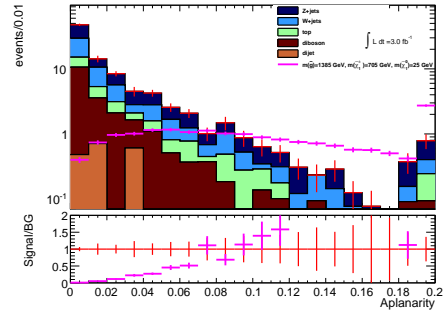


(d) $\min \Delta\phi(\text{jet}, \vec{E}_T^{\text{miss}})$

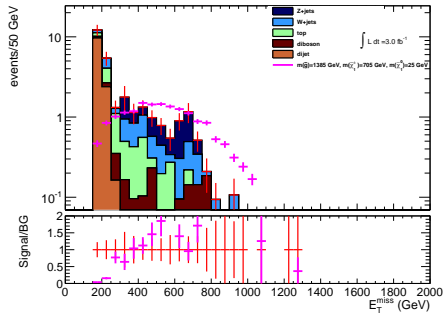
Figure 37: Distributions of each variable used in SR4jM after all the other cuts. Signal sample is the gluino direct-decay model $:(m(\tilde{g}), m(\tilde{\chi}_1^0)) = (1200, 600)$ [GeV]. The lower pad shows ratio of signal events to background events.



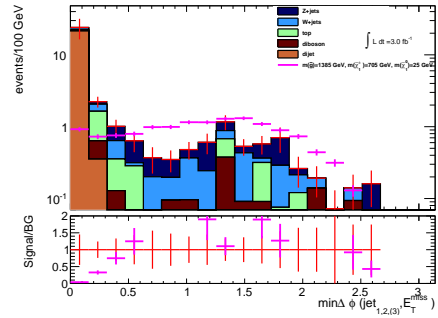
(a) m_{eff} distribution.



(b) Aplanarity distribution.



(c) E_T^{miss} distribution.



(d) $\min \Delta\phi(\text{jet}, \vec{E}_T^{\text{miss}})$

Figure 38: Distributions of each variable used in SR6jL after all the other cuts. Signal sample is the gluino onestep-decay model $:(m(\tilde{g}), m(\tilde{\chi}_1^\pm), m(\tilde{\chi}_1^0)) = (1385, 705, 25)$ [GeV]. The lower pad shows ratio of signal events to background events.

6 Background estimation

SM processes in signal region (SR) become the background (BG) events. The precise estimation of BG events is needed for higher signal sensitivity. In this chapter, the BG estimation methods used in this analysis are explained. For the BG estimation, many control regions (CRs) are prepared. In each CR, contributed SM processes are selected, and the events are used for SM BG estimation in SRs. These CRs are summarized in Sec. 6.11.

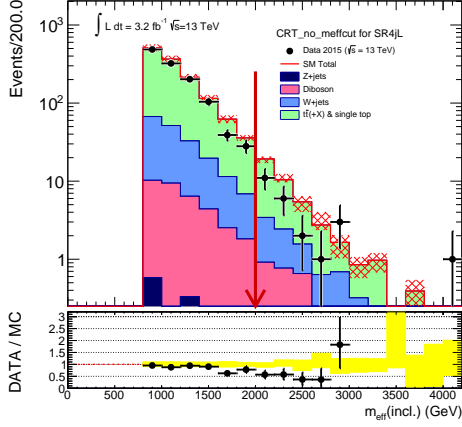
One way to estimate the SM backgrounds in SR is to use MC simulated samples. To remove the difference of acceptance between data and MC samples, some CRs are prepared. For example, as described in 6.1, a CR where SM W +jets events are enhanced is prepared to normalize the number of events, and the normalization factor is also used for W +jets SM process in a SR.

Another way to estimate the SM backgrounds is to use theoretical assumption. To estimate the hard $Z(\rightarrow \nu\nu)$ +jets BGs, γ +jets events are used as described in Sec.6.4. For this estimation, various CRs are prepared.

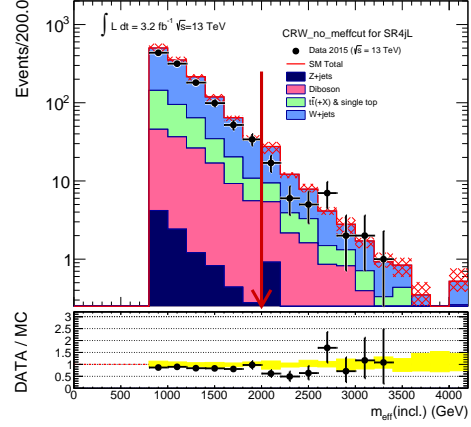
6.1 Top BGs and W BGs

Top and W +jets BGs in a SR are estimated with MC samples. To correct the difference in acceptance between data and MC, these MC samples are normalized in 1-lepton (e or μ) and $30 \text{ GeV} < m_{\text{T}}(\ell, \mathbf{E}_{\text{T}}^{\text{miss}})^1 < 100 \text{ GeV}$ region. This selection enhances the event with W boson which decays to $\ell\nu$. In the region, b-tagged ($N_{\text{Bjet}} \geq 1$) event is used for normalization of top MC samples (μ_{Top}) and b-veto ($N_{\text{Bjet}} = 0$) event is used for normalization of W +jets samples (μ_{W}). The b-tagged region is named top control region (CRT) and the SM process, $t\bar{t} \rightarrow b\bar{b}W(qq)W(\ell\nu)$, is enriched. The b-vetoed region is named W control region (CRW) and the SM process, $W(\rightarrow \ell\nu)$ +jets, is enriched. The μ_{Top} and μ_{W} are fit simultaneously in both CRT and CRW, since b-tag or b-veto migration exists because of the b-tag efficiency. In SR, the process W decays to hadronic decaying tau is dominant. To select the similar kinematic phase space, leptons in CRT and CRW are dealt as jets to reproduce the hadronic tau decay. The m_{eff} distributions in CRT and CRW for SR4jL signal region are shown in Figure 39, and the nominal number of events estimated with MC samples is normalized to the number of observed events in high m_{eff} region. The summary of top and W CRs is in Table 34.

¹ $m_{\text{T}}(\ell, \mathbf{E}_{\text{T}}^{\text{miss}}) = \sqrt{2E_{\text{T}}^{\text{miss}} p_{\text{T}}^{\ell}(1 - \cos \phi)}$, where $\phi = \Delta\phi(\mathbf{p}_{\text{T}}^{\ell}, \mathbf{E}_{\text{T}}^{\text{miss}})$



(a) m_{eff} distribution in CRT for SR4jL.



(b) m_{eff} distribution in CRW for SR4jL.

Figure 39: m_{eff} distribution in top CR and W CR. The normalizations of the MC samples are before the fit. In the high m_{eff} region (larger than the point indicated by red arrow), the number of events estimated with MC samples is normalized to that of observed data. The red shaded band in SM total and yellow band in ratio plot show MC statistical error plus systematic errors. The systematic errors are from generator uncertainties and JES uncertainty described in Sec.7.4.

6.2 Multi-jet BGs

The multi-jet background in high E_T^{miss} region is mainly from mis-measurement of jet momentum. The imbalance from jets momentum causes E_T^{miss} . The heavy flavour hadrons which decay semi-leptonically also make E_T^{miss} due to missing neutrinos. In such events, the $\min \Delta\phi(\text{jet}, \mathbf{E}_T^{\text{miss}})$ and E_T^{miss} is small. Therefore, the number of multi-jets events is very small after $\min \Delta\phi(\text{jet}, \mathbf{E}_T^{\text{miss}})$ and E_T^{miss} cuts. For the estimation of this BG events, multi-jets MC samples are used. To correct the discrepancies of acceptance and cross section for data and MC, multi-jet MC is normalized in the QCD multi-jets CR (CRQ) where inverted $\min \Delta\phi(\text{jet}, \mathbf{E}_T^{\text{miss}})$ cut is imposed. The fit parameter for normalization is $\mu_{\text{Multijets}}$.

6.3 Diboson BGs

The BG events from WW, WZ, and ZZ processes are estimated with MC samples. The CRs for these processes are not prepared, since these processes have small production cross sections. Though pure CRs for these processes can be prepared by requiring two or three leptons, branching ratios for two or three leptons are very small and enough events cannot be prepared in small integrated luminosity case.

sample name	top	W	top loose	W loose	top very loose	W very loose
region for constraint	CRW,CRT		CRTL	-	CRTVL	-
fit value	μ_{Top}	μ_{W}	μ_{TopL}	-	μ_{TopVL}	-
process for constraint	$t\bar{t} \rightarrow b\bar{b}W(qq)W(\ell\nu)$	$W(\ell\nu)+\text{jets}$	$t\bar{t} \rightarrow b\bar{b}W(qq)W(\ell\nu)$	-	$t\bar{t} \rightarrow b\bar{b}W(qq)W(\ell\nu)$	-
Lepton is dealt as	jet		$E_{\text{T}}^{\text{miss}'} = E_{\text{T}}^{\text{miss}} + \vec{p}_{\text{T}}^{\ell}$			
used regions	SR, CRY, CRYMA, CRYMa, VRZMa, VRWMA, VRWma, VRZII, VRZIIa	SR, CRY, CRYMA, CRYMa, VRZII, VRZIIa	CRWL, CRZII, CRYmA, CRYma, VRWmA, VRZIIa	CRZII, CRYmA, CRYma, VRZIIa	CRWVL, CRZIIVL	CRTVL, CRZIIVL
description compared to SR-like cuts	$E_{\text{T}}^{\text{miss}}$, aplanarity, min $\Delta\phi$ cuts are loosened.		m_{eff} cut and aplanarity cuts are inverted.		$E_{\text{T}}^{\text{miss}'}$ and m_{eff} cuts are inverted. No min $\Delta\phi$ and aplanarity cuts.	

Table 34: Summary of implementation of top and W CRs. (top or W) loose and very loose samples are used in data-driven γ replacement described in Sec.6.5.

6.4 $Z(\rightarrow \nu\nu)+\text{jets}$ BG estimation with γ replacement

$Z(\rightarrow \nu\nu)+\text{jets}$ background is the dominant BG in SR. The simple way to estimate this BG is using $Z(\rightarrow \ell\ell)+\text{jets}$ events in 2 lepton region where the events are very pure. However, the ratio of Branching Ratio (BR) is small, $\frac{BR(Z\rightarrow ee)+BR(Z\rightarrow\mu\mu)}{BR(Z\rightarrow\nu\nu)} = 6/20$. Therefore, small number of events can be obtained in tight CR with similar selection to SR. In such case, it is difficult to estimate $Z(\rightarrow \nu\nu)+\text{jets}$ events in SR. To avoid this problem, γ replace method[64, 65] is used in this analysis. This method uses the theoretical basis that the $\gamma+\text{jets}$ and $Z+\text{jets}$ are produced with the same diagram (Figure 40).

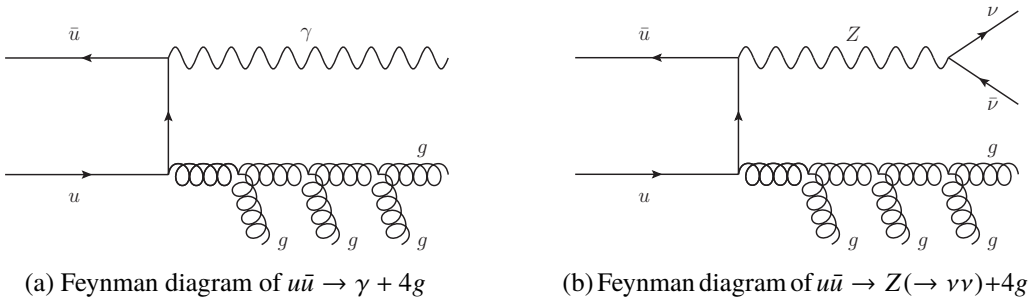


Figure 40: Feynman diagrams of $u\bar{u} \rightarrow V + 4g$.

There are some differences between $Z+\text{jets}$ and $\gamma+\text{jets}$ events which should be

taken into account:

- Difference in reconstruction efficiency and cross section between Z and γ
- Difference in couplings of partons with bosons (Z or γ)
- Difference in mass of Z and γ

The reconstruction efficiency and cross section of γ +jets event have to be normalized to $Z(\rightarrow \nu\nu)$ +jets events and the correction is described in Sec.6.5.

The difference in coupling make difference in number of jets in the production. If the same number of jets cut is imposed for γ +jets selection as for SR selection, this difference is negligible.

The difference in mass is solved by selecting high boson p_T region. Since the mass difference become negligible in high boson p_T region, the difference in boson p_T distribution of Z and γ is negligible. From the previous research [64], the p_T ratio of V+jets (V=Z and γ) follows empirical rule,

$$R = R_0 \left(\frac{p_T^2}{p_T^2 + M_Z^2} \right)^n, \quad (66)$$

where R_0 is the constant value, M_Z is the mass of Z-boson, and n is constant determined empirically. At the limit M_Z is negligible compared to boson p_T , the R become constant R_0 . $n \approx 1.2$ is determined empirically in Ref.[64] from the distributions as in the Figure 41. With this rule, The $|R-R_0|$ is at most 5% when $p_T^V > 400$ GeV(Figure 42).

Thus, if the region where p_T^V is high enough can be prepared, behaviour of Z+jets events is similar to that of γ +jets events and can be estimated with γ +jets events except for cross section and acceptance differences. This is solved by the data-driven γ replacement method described in Sec.6.5. In the CR of γ (CRY) of this estimation method, $E_T^{\text{miss}'} = |\vec{p}_T^\gamma + \vec{E}_T^{\text{miss}}|$ is used for event selection, and the same selection criteria as SR are imposed to reproduce the E_T^{miss} cut to the $Z(\rightarrow \nu\nu)$ events in SRs.

The other subject to be accounted is the purity in CRs of γ . For the control of γ +jets events, the high purity of γ is important. This estimation is described in Sec.6.10.

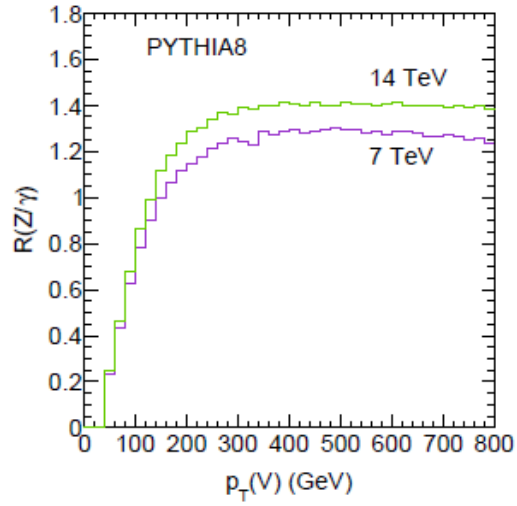


Figure 41: The boson p_T ratio for the process $pp \rightarrow V + 1parton$ from PYTHIA8 [64].

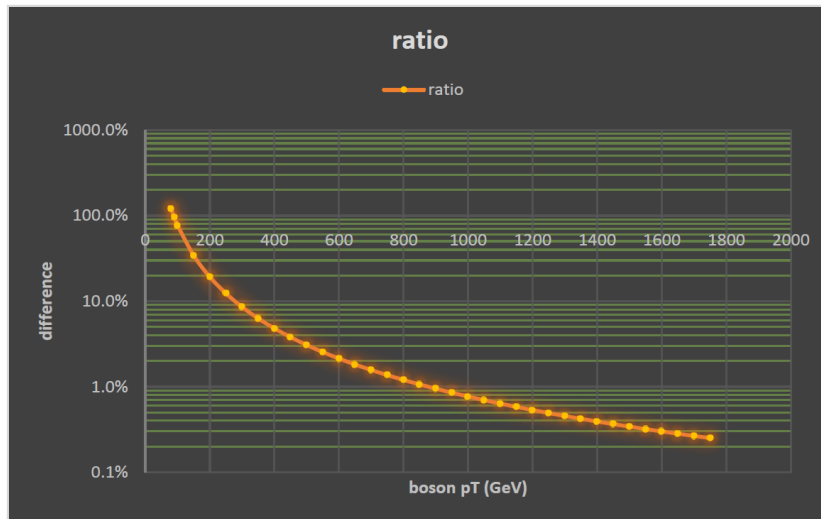


Figure 42: The $|R-R_0|$ distribution of Eq. 66.

6.5 Data-driven γ replacement

In the case that p_T of the vector boson is high enough, the difference in distributions between Z and γ are small. And the difference is only for the cross section and acceptance. In the case that E_T^{miss} cut in SR and $E_T^{\text{miss}'}$ cut in γ +jets selection are tight (E_T^{miss} or $E_T^{\text{miss}'} \gtrsim 400$ GeV), the WXYZ method described Sec.6.7 is used in this analysis. Moreover, to enhance the γ +jets events, ABCD method using γ +jets events described in Sec.6.6 is used. Though this BG estimation method is no one tried before, the validity of this method is well studied. In previous analysis [59], the γ to Z correction is derived with MC samples, hence the estimated number of $Z(\rightarrow \nu\nu)$ +jets events has large systematic uncertainty due to the generator. To avoid such uncertainty and experimental one (e.g JES uncertainty), this data-driven BG estimation is adopted in this analysis.

6.6 ABCD method for γ +jets CR

In most of the Signal Regions (SRs), the dominant Background (BG) process is $Z(\rightarrow \nu\nu)$ +jets events. This number of events can be estimated with using γ +jets events in γ +jets CR (CRY) which is determined by the similar kinematic selection criteria as SR.

Since tight selection criteria are needed for higher sensitivity of signals, number of events in CRY inevitably becomes small after the tight selection. Therefore, enhancement of number of events in CRY is needed.

In SR4jL, SR4jM, and SR6jL, effective mass (m_{eff}) and aplanarity cuts are used. Effective mass reflects the mass scale of the center of production system, and aplanarity reflects the non-planarity of the jet events. Therefore, these two variables are quite independent.

In this section, ABCD method with m_{eff} and aplanarity are studied. The general description of ABCD method is described in Appendix C.

6.6.1 Selection

For this study, a simple selection is applied (Table 35). $N_j(p_T > 60 \text{ GeV}) \geq 4$ cut is applied since aplanarity cut is mainly used in 4-jet region. $E_T^{\text{miss}'}$ means absolute value of the vector sum of γ transverse momentum and \vec{E}_T^{miss} , i.e. $E_T^{\text{miss}'} = |\vec{p}_T^\gamma + \vec{E}_T^{\text{miss}}|$.

For the ABCD method with m_{eff} and aplanarity, the four regions in Table 36 are prepared. The four regions are also shown in Figure 43.

Variable	Cut Value
Number of Leptons	$== 0$
$N_j(p_T > 60 \text{ GeV})$	≥ 4
$\min\Delta\phi(\text{jet}_{1,2,3}, E_T^{\text{miss}})$	> 0.4
$\min\Delta\phi(\text{jet}_{N_j \geq 4}, E_T^{\text{miss}})$	> 0.2
$p_T(j_1)$	$> 130 \text{ GeV}$
E_T^{miss}	$> 600 \text{ GeV}$

Table 35: Selections used in the study of ABCD method in γ CR.

Region name	cut condition
A	$m_{\text{eff}} > 2600 \text{ GeV} \& \text{ aplanarity} > 0.04$
B	$m_{\text{eff}} > 2600 \text{ GeV} \& \text{ aplanarity} \leq 0.04$
C	$2600 \text{ GeV} > m_{\text{eff}} > 1600 \text{ GeV} \& \text{ aplanarity} > 0.04$
D	$2600 \text{ GeV} > m_{\text{eff}} > 1600 \text{ GeV} \& \text{ aplanarity} \leq 0.04$

Table 36: Regions for ABCD method. The number of events in A region need to be estimated from the number of events in the other regions.

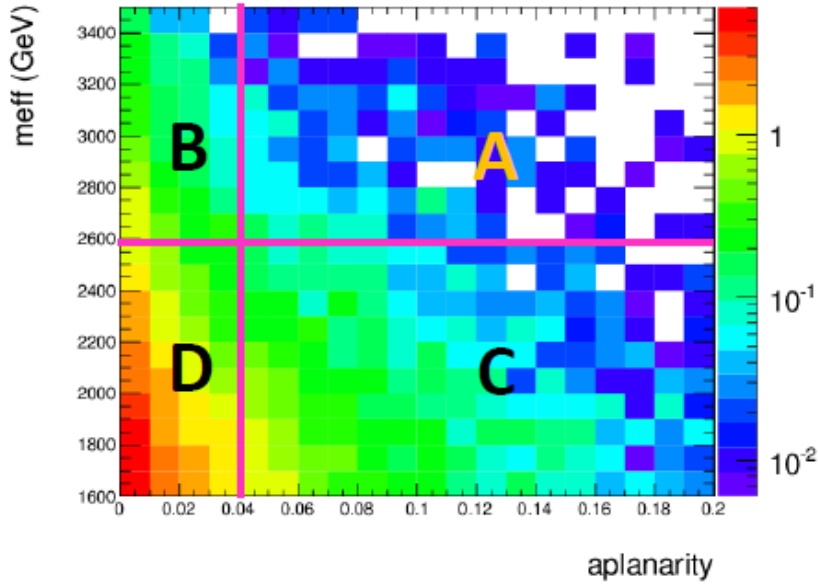


Figure 43: 2D distribution of m_{eff} vs aplanarity, and definitions of four regions. $\int L dt = 3.0 \text{ fb}^{-1}$. Aplanarity is divided into 20 bins and the range is $[0.0, 0.2]$. m_{eff} is divided into 19 bins and the range is $[1600, 2000]$ (GeV). The nominal γ +jets MC sample described in Sec.6.6.2 is used.

6.6.2 Monte Carlo sample

For the study of systematic errors due to the γ +jets event generators, one nominal Monte Carlo (MC) truth sample and four systematic MC truth samples are generated (Table 37). All the MC are generated with SHERPA. The distributions of m_{eff} and aplanarity for each sample are shown in Fig 44. Cross sections used for systematic samples are the same as nominal MC.

Varied parameters	Generator	Number of Events
Nominal	Sherpa 1.8	4500000
Factorization scale 0.25	Sherpa 2.1	4500000
Factorization scale 4.0	Sherpa 2.1	4500000
Renormalization scale 0.25	Sherpa 2.1	4500000
Renormalization scale 4.0	Sherpa 2.1	4500000

Table 37: γ +jets MC samples used in this analysis.

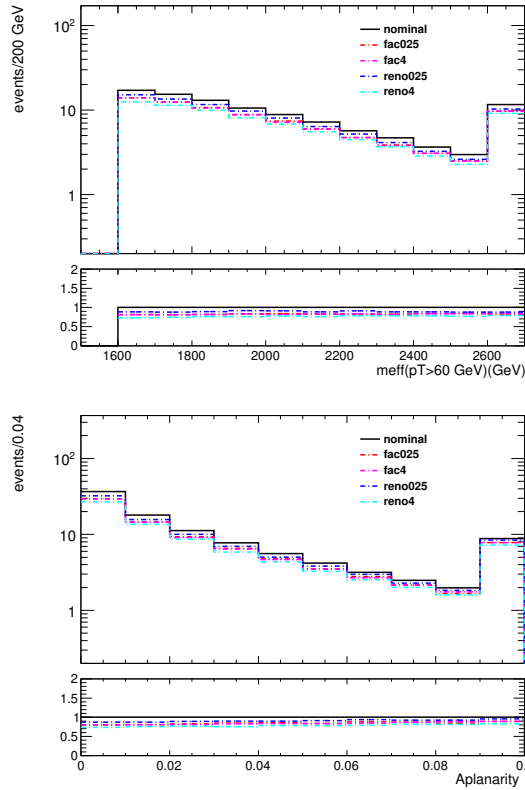


Figure 44: Distributions of m_{eff} and aplanarity for the γ +jets MC samples with varying QCD parameters. $\int \text{Ldt} = 3.0 \text{ fb}^{-1}$

6.6.3 Evaluation of the 2D correlation

The correlation of m_{eff} and aplanarity was evaluated after the selection shown in Table 35. 2D histogram of the variables is plotted in Figure 43. With this histogram, the correlation factor is calculated to be 0.0124. Thus the ABCD method can be applicable for m_{eff} and aplanarity, since correlation factor is small compared to 1.0.

6.6.4 Systematic Uncertainty in γ ABCD method

The actual uncertainty for ABCD is evaluated in this section. Because of weak correlation, this equation can be assumed,

$$A(CRY) \simeq B \times \frac{C}{D}, \quad (67)$$

where A, B, C, and D show the number of events in each corresponding region.

Therefore, the value to evaluate difference can be written as,

$$R - 1 = \frac{A}{B} \times \frac{D}{C} - 1, \quad (68)$$

,where $R = \frac{A}{B} \times \frac{D}{C}$.

$R - 1$ value is calculated for each systematic sample (Table 38).

Varied parameters	$R - 1$	$R - 1$ error (MC stat.)
Nominal	0.01622	0.00027
Factorization scale 0.25	-0.04401	0.00075
Factorization scale 4.0	-0.02619	0.00045
Renormalization scale 0.25	0.00071	0.00001
Renormalization scale 4.0	-0.02653	0.00047

Table 38: $R - 1$ values for each systematic sample

As a result, the $R - 1$ value and uncertainties for $R - 1$ are,

$$(R - 1) = 0.01622 \pm 0.00027(\text{MC stat.}) \pm 0.043(\text{syst.}), \quad (69)$$

where uncertainty of each systematic sample is half of the difference from the nominal sample. An expected number of events in region A is 2.98 ± 0.04 (MC stat. error) and in region B is 11.6 ± 0.08 (MC stat. error). Therefore, 3.89 times of events can be gained, and statistical error of observed number of events can be decreased from $\sim 58\%$ to $\sim 29\%$ only with increasing systematic uncertainty by at most $\sim 4\%$.

6.7 WXYZ method

Philosophy of this method is the following:

- (1) Since the major background in SR is $Z(\rightarrow \nu\nu)$ +jets events, this number should be reliably estimated by using number of events in various CRs, not relying on the MC simulation as much as possible.
- (2) The ratios between numbers of events in one CR to the other CR (scale factors) should be evaluated in two CRs where reasonably large number of events are expected.

The definitions of each CRs are summarized in Table 48 in Sec.6.11 and it would help to understand the method.

This is the method to estimate X ($Z \rightarrow \nu\nu$) events in SR using $W(W \rightarrow \ell\nu)$, $Y(\gamma)$, and $Z(Z \rightarrow \ell\ell)$ events in each CR. In high vector boson p_T region, the ratio of p_T^V distributions for γ and Z, as well as that for γ and W are flat, since the mass differences are negligible. Using this fact, the $Z(\rightarrow \nu\nu)$ +jets in SR are estimated with γ +jets in CR of γ (CRY) where similar selections are applied to SR. At this point, the key issue is to normalize the number of γ +jets events to that of $Z(\rightarrow \nu\nu)$ +jets events. This is represented in equation,

$$N_{\text{SR}}^{Z(\nu\nu),\text{expected}} = N_{\text{CRY}}^{\gamma+\text{jets,data}} \cdot \text{SF} \left(\frac{Z(\nu\nu) + \text{jets}}{\gamma + \text{jets}} \right), \quad (70)$$

where SF means Scale Factor. One of the simple ideas is to prepare SF in loose CR and normalize γ +jets events to $Z(\rightarrow \ell\ell)$ +jets events. However, the number of $Z(\rightarrow \ell\ell)$ +jets events become too small with tight p_T^Z cut. In order to avoid this problem, $W(\rightarrow \ell\nu)$ +jets events are used intermediately for the normalization. Similar to the relation between Z+jets and γ +jets, W+jets and γ +jets behave similarly with high p_T^V cut. Therefore, at first, number of γ +jets events are once normalized to number of $W(\rightarrow \ell\nu)$ +jets events in loose CR as in the Figure 45. This CR is defined with the same $E_T^{\text{miss}/2}$ cut but with inverted aplanarity and m_{eff} cuts.

² $E_T^{\text{miss}'} = |\mathbf{E}_T^{\text{miss}} + p_T(\gamma)|$ for γ , and $E_T^{\text{miss}'} = |\mathbf{E}_T^{\text{miss}} + p_T(\text{lepton})|$ for $W(\rightarrow \ell\nu)$. For the case of $W(\rightarrow \ell\nu)$, the neutrino p_T^{ν} is already included in \vec{E}_T^{miss} . Therefore $E_T^{\text{miss}'}$ is missing p_T^W of W boson. For large p_T^W , where W boson mass is negligible, p_T^W and p_T^γ are expected to have similar distributions.

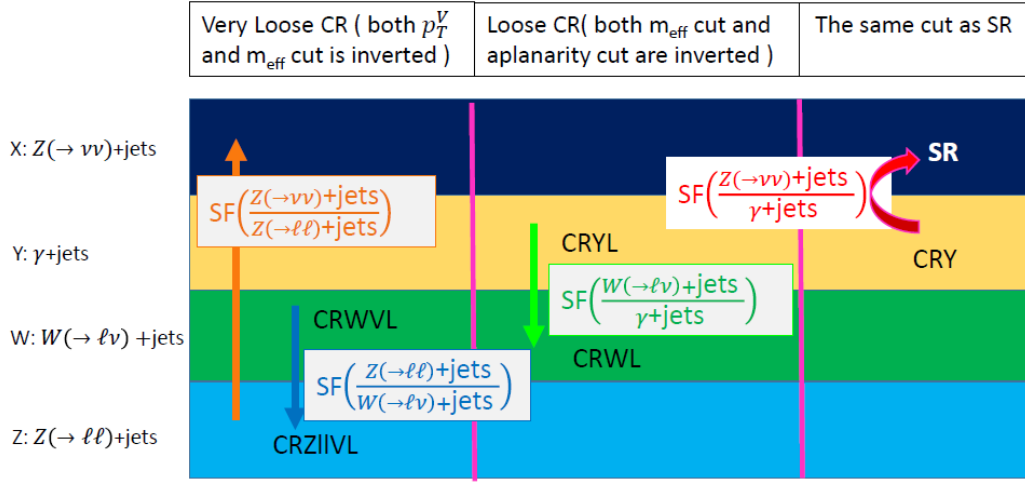


Figure 45: Conceptual figure of the WXYZ method. There are three types of CRs. First is the tight CR which has similar kinematic cut as SR. Second is the loose(L) CR where m_{eff} cut and aplanarity cut are inverted to the selection imposed in SR. Third is the very loose (VL) CR where p_T^V cut and m_{eff} cut are inverted to the selection imposed in SR. In tight CR, a γ CR is named as CRY. In Loose CR, the γ CR is named as CRYL, and a CR for $W(\rightarrow \ell\nu)+jets$ is named as CRWL, which means loose CR of W. In very loose CR, a CR for $W(\rightarrow \ell\nu)+jets$ is named as CRWVL, which means very loose CR of W, and a CR for $Z(\rightarrow \ell\ell)+jets$ is named as CRZIIVL, which means very loose CR of $Z(\rightarrow \ell\ell)$. The $SF\left(\frac{Z(\rightarrow \nu\nu)+jets}{\gamma+jets}\right)$ is the ratio of number of events in SR ($Z(\rightarrow \nu\nu)$) to CRY. The $SF\left(\frac{W(\rightarrow \ell\nu)+jets}{\gamma+jets}\right)$ is the ratio of number of events in CRWL to CRYL. The $SF\left(\frac{Z(\rightarrow \ell\ell)+jets}{W(\rightarrow \ell\nu)+jets}\right)$ is the ratio of number of events in CRZIIVL to CRWVL. The $SF\left(\frac{Z(\rightarrow \nu\nu)+jets}{Z(\rightarrow \ell\ell)+jets}\right)$ is the correction factor of lepton acceptance and branching ratio. The WXYZ method assume that $SF\left(\frac{Z(\rightarrow \nu\nu)+jets}{\gamma+jets}\right) = SF\left(\frac{W(\rightarrow \ell\nu)+jets}{\gamma+jets}\right) \cdot SF\left(\frac{Z(\rightarrow \ell\ell)+jets}{W(\rightarrow \ell\nu)+jets}\right) \cdot SF\left(\frac{Z(\rightarrow \nu\nu)+jets}{Z(\rightarrow \ell\ell)+jets}\right)$. Such SF is evaluated in the CR where reasonably large number of events is expected for the corresponding data sample.

These are represented with equation,

$$\begin{aligned} \text{SF} \left(\frac{Z(\nu\nu) + \text{jets}}{\gamma + \text{jets}} \right) &= \text{SF} \left(\frac{W(\ell\nu) + \text{jets}}{\gamma + \text{jets}} \right) \cdot \text{SF} \left(\frac{Z(\nu\nu) + \text{jets}}{W(\ell\nu) + \text{jets}} \right) \\ &= \frac{N_{\text{CRWL}}^{W(\ell\nu)+\text{jets,data}}}{N_{\text{CRYL}}^{\gamma+\text{jets,data}}} \cdot \text{SF} \left(\frac{Z(\nu\nu) + \text{jets}}{W(\ell\nu) + \text{jets}} \right), \end{aligned} \quad (71)$$

where CRUL (U=W or γ) is loose CR with the same $E_T^{\text{miss}'}$ cut in CRY and with inverted m_{eff} and Aplanarity cut.

Secondly, the $W(\rightarrow \ell\nu)+\text{jets}$ events are normalized to $Z(\rightarrow \ell\ell)$ events in very loose CR, where inverted $E_T^{\text{miss}'}$ cut is applied as shown in Figure 45. The mass difference between W and Z is negligible compared to the minimum $E_T^{\text{miss}'}$ cut > 200 GeV which is applied for very loose CRs. These are represented with equation,

$$\text{SF} \left(\frac{Z(\nu\nu) + \text{jets}}{W(\ell\nu) + \text{jets}} \right) = \frac{N_{\text{CRZIIVL}}^{Z(\ell\ell)+\text{jets,data}}}{N_{\text{CRWVL}}^{W(\ell\nu)+\text{jets,data}}} \cdot \text{SF} \left(\frac{Z(\nu\nu) + \text{jets}}{Z(\ell\ell) + \text{jets}} \right), \quad (72)$$

where CRUVL (first U=ZII or W) is the very loose CR with inverted $E_T^{\text{miss}'}$ cut of CRYL or CRWL. The $\text{SF} \left(\frac{Z(\nu\nu)+\text{jets}}{Z(\ell\ell)+\text{jets}} \right)$ includes the lepton acceptance correction and BR correction. In this analysis, this SF is calculated from MC,

$$\text{SF} \left(\frac{Z(\nu\nu) + \text{jets}}{Z(\ell\ell) + \text{jets}} \right) = \frac{N_{\text{VRZVL}}^{Z(\nu\nu)+\text{jets,MC}}}{N_{\text{CRZIIVL}}^{Z(\ell\ell)+\text{jets,MC}}}, \quad (73)$$

Summarizing Eq. (70, 71, 72, and 73):

$$N_{\text{SR}}^{Z(\nu\nu),\text{expected}} = N_{\text{CRY}}^{\gamma+\text{jets,data}} \cdot \frac{N_{\text{CRWL}}^{W(\ell\nu)+\text{jets,data}}}{N_{\text{CRYL}}^{\gamma+\text{jets,data}}} \cdot \frac{N_{\text{CRZIIVL}}^{Z(\ell\ell)+\text{jets,data}}}{N_{\text{CRWVL}}^{W(\ell\nu)+\text{jets,data}}} \cdot \frac{N_{\text{VRZVL}}^{Z(\nu\nu)+\text{jets,MC}}}{N_{\text{CRZIIVL}}^{Z(\ell\ell)+\text{jets,MC}}} \quad (74)$$

This is the basic of the WXYZ method.

6.7.1 Small Corrections for WXYZ method

There are some assumption in WXYZ method and they are put aside in Sec.6.7.

At first, in Eq. (71), it is assumed that

$$R_{Z/Y} := \frac{N_{SR}^{Z(\nu\nu)} \cdot N_{CRYL}^{\gamma+jets}}{N_{CRY}^{\gamma+jets} \cdot N_{VRZL}^{Z(\nu\nu)}} \simeq 1, \quad (75)$$

where VRZL is the 0-lepton loose cut region whose cut is similar to CRYL. If $(R_{Z/Y} - 1)$ evaluated by MC is not zero, the value $R_{Z/Y}$ should be multiplied to $N_{CRYL}^{\gamma+jets}$ and the difference from 1 should be considered as uncertainty.

Secondly, in Eq. (72), it is assumed that

$$R_{Z/W} := \frac{N_{CRZIII}^{Z(\ell\ell)+jets} \cdot N_{CRWVL}^{W(\ell\nu)+jets}}{N_{CRWL}^{W(\ell\nu)+jets} \cdot N_{CRZIIIVL}^{Z(\ell\ell)+jets}} \simeq 1, \quad (76)$$

If $(R_{Z/W} - 1)$ evaluated by MC is not zero, the value $R_{Z/W}$ should be multiplied to $N_{CRZIIIVL}^{Z(\ell\ell)+jets}$ and the difference from 1 should be considered as uncertainty.

6.7.2 WXYZ method with ABCD method

For the estimation of $Z \rightarrow \nu\nu$ BG in SR with m_{eff} and aplanarity cut, ABCD method with m_{eff} and aplanarity (Sec.6.6) is also used. For the ABCD method, the CRY in Sec.6.7 is renamed as CRYMA, which means the CR of γ where both m_{eff} cut and aplanarity cut are imposed. In the naming scheme for CRs, the followings are used,

- M : m_{eff} cut is imposed.
- A : aplanarity cut is imposed.
- m : Inverted m_{eff} cut is imposed.
- a : Inverted aplanarity cut is imposed.

For ABCD method, 3 additional CR for $\gamma+jets$ is needed,

- CRYMa: A CR of γ where m_{eff} cut and inverted aplanarity cut are imposed.
- CRYmA: A CR of γ where inverted m_{eff} cut, and aplanarity cut are imposed.
- CRYma: A CR of γ where inverted m_{eff} cut, and inverted aplanarity cut are imposed.

Using these regions, ABCD method can be written:

$$N_{CRYMA}^{\gamma+jets,data} = \frac{N_{CRYMa}^{\gamma+jets,data} \cdot N_{CRYmA}^{\gamma+jets,data}}{N_{CRYma}^{\gamma+jets,data}}. \quad (77)$$

If the correction factor is needed for ABCD method, Eq. (77) is corrected,

$$\begin{cases} N_{CRYMA}^{\gamma+jets,data} = \frac{(N_{CRYMa}^{\gamma+jets,data} \cdot R_{YABCD}) \cdot N_{CRYmA}^{\gamma+jets,data}}{N_{CRYma}^{\gamma+jets,data}} \\ R_{YABCD} := \frac{N_{CRYMA}^{\gamma+jets,MC} \cdot N_{CRYma}^{\gamma+jets,MC}}{N_{CRYMa}^{\gamma+jets,MC} \cdot N_{CRYmA}^{\gamma+jets,MC}} \end{cases} \quad (78)$$

Including all Eq. (74, 76, 75, 78),

$$N_{SR}^{Z(\nu\nu),expected} = \frac{(N_{CRYMa}^{\gamma+jets,data} \cdot R_{YABCD}) \cdot N_{CRYmA}^{\gamma+jets,data}}{N_{CRYma}^{\gamma+jets,data}} \cdot \frac{N_{CRWL}^{W(\ell\nu)+jets,data} \cdot R_{Z/Y}}{N_{CRYma}^{\gamma+jets,data}} \cdot \frac{N_{CRZIIVL}^{Z(\ell\ell)+jets,data} \cdot R_{Z/W}}{N_{CRWVL}^{W(\ell\nu)+jets,data}} \cdot \frac{N_{VRZVL}^{Z(\nu\nu)+jets,MC}}{N_{CRZIIVL}^{Z(\ell\ell)+jets,MC}}, \quad (79)$$

where CRYma is also used as CRYL.

6.7.3 WXYZ method without ABCD method

As in the Table 33, aplanarity cut is not imposed for SR2jC. For the background estimation in SR2jC, WXYZ method without ABCD method is used. This is the same as Eq.74 with correction factors Eq.75 and Eq.76. To use the same naming scheme as WXYZ method with ABCD method, WXYZ method without ABCD method is written as,

$$N_{SR}^{Z(\nu\nu),expected} = N_{CRYMA}^{\gamma+jets,data} \cdot \frac{N_{CRWL}^{W(\ell\nu)+jets,data} \cdot R_{Z/Y}}{N_{CRYma}^{\gamma+jets,data}} \cdot \frac{N_{CRZIIVL}^{Z(\ell\ell)+jets,data} \cdot R_{Z/W}}{N_{CRWVL}^{W(\ell\nu)+jets,data}} \cdot \frac{N_{VRZVL}^{Z(\nu\nu)+jets,MC}}{N_{CRZIIVL}^{Z(\ell\ell)+jets,MC}}, \quad (80)$$

where CRYMA is the CRY, and CRYma is the region m_{eff} cut is inverted. Because aplanarity cut is not applied, the "A" and "a" in the names of CRs are meaningless.

6.7.4 Fitting implementation of ABCD and WXYZ method

The implementation of simultaneous fit is very complex for solving the correlation among many CRs. For this, the same variable (ε in this section) should be used in

different CRs to transfer the correlation effects. The definition of fit parameter is in Table 39. These parameters are simultaneously fitted in the all control regions. To avoid the local minimum, initial value is obtained from MC estimation. However, the parameters can freely change $\pm 100\%$ from the nominal value. The same number of CRs are prepared as these fit parameters. Therefore, all the parameters are determined, unless other nuisance parameters.

In addition to these fit parameters, there are correction factors Rs as in Eq.(75, 76, and 78), and

$$SF_{\ell\ell/\nu\nu} = \frac{N_{\text{CRZIIVL}}^{Z(\ell\ell)+\text{jets,MC}}}{N_{\text{VRZVL}}^{Z(\nu\nu)+\text{jets,MC}}}, \quad (81)$$

where the numerator and denominator of SF are inverted for technical requirement. R correction factors are evaluated with using MC. For the conservative estimation, the fit range (error) of Rs are set to include 1.0. $SF_{\ell\ell/\nu\nu}$ values are derived from full simulated MC.

Now all the materials are prepared. The actual fitting implementations are described in following paragraphs.

Practical implementation of WXYZ with ABCD method

Summarizing all Eq. (79, 81) and Table 39, the practical implementation with fit parameters are,

$$\begin{aligned} (\mu_Z)_{\text{SR}} = & \frac{(\mu_Z \cdot \varepsilon_{YMA} \cdot \varepsilon_{YMa} \cdot R_{YABCD})_{\text{CRYMa}} \cdot (\mu_Z \cdot \varepsilon_{YMA} \cdot \varepsilon_{YmA})_{\text{CRYmA}}}{(\mu_Z \cdot \varepsilon_{YMA} \cdot \varepsilon_{YMa} \cdot \varepsilon_{YmA})_{\text{CRYma}}} \\ & \cdot \frac{(\mu_Z \cdot \varepsilon_{YMA} \cdot \varepsilon_{YMa} \cdot \varepsilon_{YmA} \cdot \varepsilon_{WL} \cdot R_{Z/Y})_{\text{CRWL}}}{(\mu_Z \cdot \varepsilon_{YMA} \cdot \varepsilon_{YMa} \cdot \varepsilon_{YmA})_{\text{CRYma}}} \\ & \cdot \frac{(\mu_Z \cdot \varepsilon_{\text{CRZIIVL}} \cdot R_{Z/W} \cdot SF_{\ell\ell/\nu\nu})_{\text{CRZIIVL}}}{(\mu_Z \cdot \varepsilon_{YMA} \cdot \varepsilon_{WL} \cdot \varepsilon_{\text{CRZIIVL}})_{\text{CRWVL}}}. \end{aligned} \quad (82)$$

As you can calculate, all the parameters (ε) in right hand side are cancelled in total.

Practical implementation of WXYZ without ABCD method

Summarizing all Eq. (80, 81) and Table 39, the practical implementation with fit parameters are,

$$\begin{aligned} (\mu_Z)_{\text{SR}} = & (\mu_Z \cdot \varepsilon_{YMA})_{\text{CRYMA}} \cdot \frac{(\mu_Z \cdot \varepsilon_{YMA} \cdot \varepsilon_{Yma} \cdot \varepsilon_{WL} \cdot R_{Z/Y})_{\text{CRWL}}}{(\mu_Z \cdot \varepsilon_{YMA} \cdot \varepsilon_{Yma})_{\text{CRYma}}} \\ & \cdot \frac{(\mu_Z \cdot \varepsilon_{\text{CRZIIVL}} \cdot R_{Z/W} \cdot SF_{\ell\ell/\nu\nu})_{\text{CRZIIVL}}}{(\mu_Z \cdot \varepsilon_{YMA} \cdot \varepsilon_{WL} \cdot \varepsilon_{\text{CRZIIVL}})_{\text{CRWVL}}}. \end{aligned} \quad (83)$$

variable	definition	description
μ_Z	$N_{SR}^{Z(\nu\nu)}$	Number of Z+jets events in SR.
ϵ_{YMA}	$\frac{N_{CRYMA}^{\gamma+jets}}{N_{SR}^{Z(\nu\nu)}}$	Ratio of number of events in CRYMA (γ +jets) to SR(Z+jets).
ϵ_{YmA}	$\frac{N_{CRYmA}^{\gamma+jets}}{N_{CRYMA}^{\gamma+jets}}$	Ratio of number of events in CRYmA (γ +jets) to CRYMA (γ +jets). This is not used in WXYZ method without ABCD method.
ϵ_{YMa}	$\frac{N_{CRYMa}^{\gamma+jets}}{N_{CRYMA}^{\gamma+jets}}$	Ratio of number of events in CRYMa (γ +jets) to CRYMA (γ +jets). This is not used in WXYZ method without ABCD method.
ϵ_{Yma}	$\frac{N_{CRYma}^{\gamma+jets}}{N_{CRYMA}^{\gamma+jets}}$	Ratio of number of events in CRYma (γ +jets) to CRYMA (γ +jets). This is not used in WXYZ method with ABCD method, since $\epsilon_{Yma} = \epsilon_{YmA} \cdot \epsilon_{YMa}$.
ϵ_{WL}	$\frac{N_{CRWL}^{W(\ell\nu)+jets}}{N_{CRYma}^{\gamma+jets}}$	Ratio of number of events in CRWL ($W(\ell\nu) + jets$) to CRYma (γ +jets).
$\epsilon_{CRZIIVL}$	$\frac{N_{VRZVL}^{Z(\nu\nu)+jets}}{N_{SR}^{Z(\nu\nu)+jets}}$	Ratio of number of events in VRZVL(Z+jets) to SR(Z+jets).

Table 39: Definitions of fit parameters in simultaneous fit. The fitted values and scan ranges are listed in Table 43-46 for different SRs.

Validation region (VR) with WXYZ method

Using all the information in previous sections, some validation regions can be implemented as described in Table 40. The "One photon", "One lepton", "Two lepton", and "No lepton" definitions and pre-selections are described afterwards in Table 47. The details of the selections are summarized afterwards in Sec.6.12.

Region Name	implementation in WXYZ+ABCD	implementation in WXYZ w/o ABCD	Description
CRYMA	$\mu_Z \cdot \varepsilon_{YMA}$	-	"One photon" VR when WXYZ w/o ABCD is used.
VRZll	$\mu_Z \cdot SF_{\ell\ell/\nu\nu}$		"Two lepton", $Z(\ell\ell)$ VR with similar kinematic selection criteria as SR.
VRZllmA	$\mu_Z \cdot \varepsilon_{mA} \cdot SF_{\ell\ell/\nu\nu}$	-	"Two lepton", $Z(\ell\ell)$ VR.
VRZllMa	$\mu_Z \cdot \varepsilon_{Ma} \cdot SF_{\ell\ell/\nu\nu} \cdot R_{YABCD}$	-	"Two lepton", $Z(\ell\ell)$ VR.
VRZMa	$\mu_Z \cdot \varepsilon_{Ma} \cdot R_{YABCD}$	-	"No lepton" VR.
VRZma	$\mu_Z \cdot \varepsilon_{Ma} \cdot \varepsilon_{mA}$	$\mu_Z \cdot \varepsilon_{ma}$	"No lepton" VR.
VRWMA	$\mu_Z \cdot \varepsilon_{YMA} \cdot \varepsilon_{WL}$		"One lepton", $W(\rightarrow \ell\nu)$ VR.
VRWmA	$\mu_Z \cdot \varepsilon_{YMA} \cdot \varepsilon_{mA} \cdot \varepsilon_{WL}$	-	"One lepton", $W(\rightarrow \ell\nu)$ VR.
VRWMa	$\mu_Z \cdot \varepsilon_{YMA} \cdot \varepsilon_{Ma} \cdot \varepsilon_{WL} \cdot R_{YABCD}$	-	"One lepton", $W(\rightarrow \ell\nu)$ VR.

Table 40: All the possible implementation of VRs with ε s and R s in (ABCD+)WXYZ method. The naming scheme, e.g. MA, is the same as described in Sec.6.7.2 and Sec.6.7.3. The "One photon", "One lepton", "Two lepton", and "No lepton" definitions and pre-selections are in Table 47.

6.7.5 Removing contaminating events in CRs

The contaminating events in CRs have to be removed. The MC samples are used to remove the contamination as follows

- CRWL: Diboson, Z+jets and top MCs are used to remove the contamination. The nominal diboson MC sample is used. The normalization factor of Z+jets MCs (μ_{ZL}) is fitted in CRZlIL. The normalization factor of Top MCs (μ_{TopL}) is fitted in CRTL.
- CRWVL : Diboson, Z+jets and top MCs are used to remove the contamination. The nominal diboson and Z+jets MC samples are used. The normalization factor of Top MCs (μ_{TopVL}) is fitted in CRTVL.

- CRZIIVL: Diboson, W+jets and top MCs are used to remove the contamination. The nominal diboson and W+jets MC samples are used. The normalization factor of Top MCs (μ_{TopVL}) is fitted in CRTVL.
- CRZLIII: Diboson, W+jets and top MCs are used to remove the contamination. The nominal diboson and W+jets MC samples are used. The normalization factor of Top MCs (μ_{TopL}) is fitted in CRTL.
- CRTL : Diboson, W+jets and Z+jets MCs are used to remove the contamination. The nominal diboson and W+jets MC samples are used. The normalization factor of Z+jets MCs (μ_{ZL}) is fitted in CRZIII.
- CRTVL: Diboson, W+jets and Z+jets MCs are used to remove the contamination. The nominal MC samples are used.

The details of top and W MC usage are summarized in Table 34.

6.8 γ/Z and W/Z check

Before the usage of WXYZ method described in Sec6.7, some points given below should be checked:

1. The number of event ratio (γ/Z) of m_{eff} and aplanarity distribution after the tight p_T^V cut. Because Z/γ ratio is extrapolated from high m_{eff} and aplanarity regions to low m_{eff} and aplanarity region, the flatness of the ratio distribution is needed.
2. The number of event ratio (W/Z) of E_T^{miss} distribution after the inverted m_{eff} cut. Because W/Z ratio is Z/W ratio is extrapolated from low E_T^{miss} to high E_T^{miss} region, the flatness of the ratio distribution is needed.

For the study of γ/Z ratio or W/Z ratio, the baseline selection (Table 41) is prepared. These studies are done with truth SHERPA samples calculated at leading order, and jet and E_T^{miss} smearing described in Sec.3.2 are applied.

For the study of γ/Z ratio, the distributions are checked as in Figure 46. Since the ratio plot is flat, it is acceptable to extrapolate γ/Z ratio along aplanarity and m_{eff} .

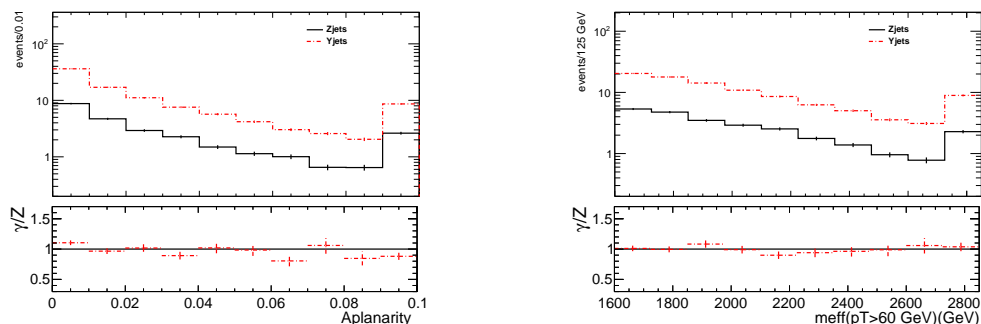
For the study of W/Z ratio, the distributions are checked as in Figure 47. Since the ratio plot is flat, it is acceptable to extrapolate W/Z ratio along E_T^{miss} .

³ E_T^{miss} for Z sample, and $|\vec{E}_T^{\text{miss}} + \vec{p}_T(\gamma)|$ for γ sample.

⁴ E_T^{miss} for Z sample, and $|\vec{E}_T^{\text{miss}} + \vec{p}_T(\text{lepton})|$ for W($\ell\nu$) sample.

variable name	cut value
$N_{\text{lep}} =$	0
$N_{\text{jet}}(p_{\text{T}} > 60\text{GeV}) \geq$	4
$p_{\text{T}}(j_{1st}) >$	130 GeV
$\min \Delta\phi(\text{jet}_{1,2,(3)}, \mathbf{E}_{\text{T}}^{\text{miss}'}) >$	0.4
$\min \Delta\phi(\text{jet}_{i>3}, \mathbf{E}_{\text{T}}^{\text{miss}'}) >$	0.2

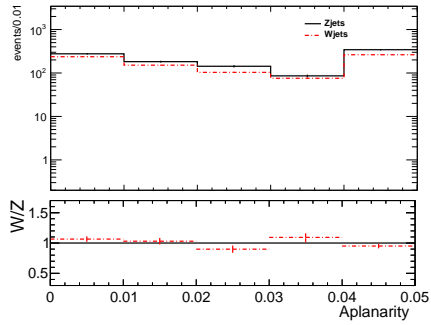
Table 41: Baseline selection for the study of γ/Z ratio and W/Z ratio. In $Z(\nu\nu)$ sample, $\mathbf{E}_{\text{T}}^{\text{miss}'}$ is vector sum of \vec{p}_{T} of neutrinos. In $W(\ell\nu)$ sample, $\mathbf{E}_{\text{T}}^{\text{miss}'}$ is vector sum of p_{T} of neutrinos and a lepton. In γ sample, $\mathbf{E}_{\text{T}}^{\text{miss}'}$ is vector sum of \vec{p}_{T} of neutrinos and γ .



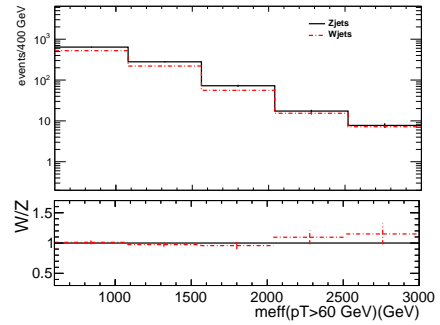
(a) Aplanarity distribution after the $m_{\text{eff}} > 1600$ GeV cut in addition.

(b) m_{eff} distribution.

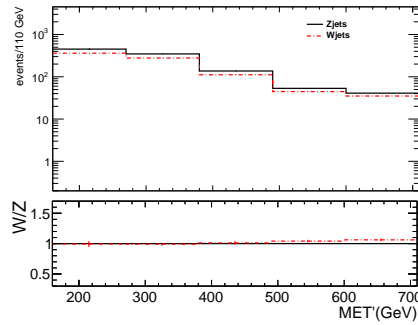
Figure 46: In addition to the baseline cut (Table 41), $E_{\text{T}}^{\text{miss}'} > 600$ GeV cut ³ is applied for MC event samples. Overflow bin is merged into the highest bin. In each figure, the lower plot shows the ratio of distributions for γ +jets and $Z(\nu\nu)$ +jets events after the normalization.



(a) Aplanarity distribution.



(b) m_{eff} distribution.



(c) E_T^{miss} or $E_T^{\text{miss}'}$ distribution.

Figure 47: In addition to the baseline cut (Table 41), $E_T^{\text{miss}'} > 200$ GeV cut⁴ is applied for MC event samples. Overflow bin is merged into the highest bin. In each figure, the lower plot shows the ratio of distributions for $W(\ell\nu)$ +jets and $Z(\nu\nu)$ +jets events after the normalization.

6.9 Expectation from MCs

Expected number of events in each CR is summarized in Table 42. In **SR2jC**, CRYMa and CRYmA don't exist since no aplanarity cut is applied. The expected number of events in each region is not small, hence it is good for background estimation.

	SR2jC	SR4jL	SR4jM	SR6jL
SR	24.8 ± 0.2	5.02 ± 0.07	6.0 ± 0.1	1.41 ± 0.05
CRYMA	58.6 ± 0.7	10.4 ± 0.3	12.8 ± 0.4	2.7 ± 0.2
CRYMa	-	21.4 ± 0.5	86 ± 1	8.1 ± 0.3
CRYmA	-	90 ± 1	29.3 ± 0.7	6.2 ± 0.3
CRYma	55.0 ± 0.8	186 ± 1	228 ± 2	21.6 ± 0.7
CRWL	19.9 ± 0.2	62.7 ± 0.7	75.4 ± 0.9	7.2 ± 0.3
CRWVL	3074 ± 27	493 ± 11	439 ± 10	34.6 ± 2.2
CRZIIVL	567 ± 5	95 ± 2	84 ± 2	8.1 ± 0.8

Table 42: Expected number of events in each CRs. The error is MC statistical errors.

The evaluated parameters for data-driven BG estimation with MCs are in Table (43, 44, 45, 46). The estimated value with MC is set as initial value in fitting to avoid local minimum. The fit range (or error) for the main parameters like ε_* is set to be $\pm 100\%$ of the initial value. The $SF_{\ell\ell/\nu\nu}$ value and errors are from expected ratio and statistical error estimated with MC for each.

About the correction factors (Rs), they ideally expected to be $\simeq 1$. Therefore, the maximum between MC statistical error and the difference from 1 is set as uncertainties for fit. Since the values of all fit parameters (ε_*) are determined with all the CRs unless correction factor Rs, errors from R result in uncertainties of this method.

Parameter	Value	Error from MC	Error for fit
μ_Z	24.8	± 0.2	$\pm 100\%$
ε_{YMA}	2.35	± 0.03	$\pm 100\%$
ε_{Yma}	0.94	± 0.01	$\pm 100\%$
ε_{WL}	0.363	± 0.007	$\pm 100\%$
$\varepsilon_{CRZIIVL}$	136	± 1	$\pm 100\%$
Correction factors and uncertainties.			
$SF_{\ell\ell/\nu\nu}$	0.168	± 0.001	± 0.001
$R_{Z/Y}$	1.29	± 0.04	± 0.29
$R_{Z/W}$	0.893	± 0.04	± 0.11

Table 43: SR2jC: The estimated parameters with MC and errors for fit. The MC statistical error is calculated from first-order approximation of error propagation.

Parameter	Value	Error from MC	Error for fit
μ_Z	5.02	± 0.02	$\pm 100\%$
ε_{YMA}	2.09	± 0.08	$\pm 100\%$
ε_{YMa}	2.04	± 0.09	$\pm 100\%$
ε_{YmA}	8.6	± 0.3	$\pm 100\%$
ε_{WL}	0.338	± 0.005	$\pm 100\%$
$\varepsilon_{CRZIIVL}$	135	± 3	$\pm 100\%$
Correction factors and uncertainties.			
$SF_{\ell\ell/\nu\nu}$	0.140	± 0.004	± 0.004
R_{ABCD}	1.01	± 0.04	± 0.04
$R_{Z/Y}$	1.39	± 0.05	± 0.39
$R_{Z/W}$	1.01	± 0.04	± 0.04

Table 44: SR4jL: The estimated parameters with MC and errors for fit. The MC statistical error is calculated from first-order approximation of error propagation.

Parameter	Value	Error from MC	Error for fit
μ_Z	6.0	± 0.1	$\pm 100\%$
ε_{YMA}	2.12	± 0.08	$\pm 100\%$
ε_{YMa}	6.7	± 0.2	$\pm 100\%$
ε_{YmA}	2.3	± 0.1	$\pm 100\%$
ε_{WL}	0.330	± 0.005	$\pm 100\%$
$\varepsilon_{CRZIIVL}$	99	± 2	$\pm 100\%$
Correction factors and uncertainties.			
$SF_{\ell\ell/\nu\nu}$	0.141	± 0.005	± 0.005
R_{ABCD}	1.16	± 0.05	± 0.16
$R_{Z/Y}$	1.39	± 0.05	± 0.39
$R_{Z/W}$	1.04	± 0.04	± 0.04

Table 45: SR4jM: The estimated parameters with MC and errors for fit. The MC statistical error is calculated from first-order approximation of error propagation.

Parameter	Value	Error from MC	Error for fit
μ_Z	1.41	± 0.05	$\pm 100\%$
ε_{YMA}	1.8	± 0.1	$\pm 100\%$
ε_{YMa}	3.0	± 0.2	$\pm 100\%$
ε_{YmA}	2.3	± 0.3	$\pm 100\%$
ε_{WL}	0.33	± 0.01	$\pm 100\%$
$\varepsilon_{CRZIIVL}$	41	± 2	$\pm 100\%$
Correction factors and uncertainties.			
$SF_{\ell\ell/\nu\nu}$	0.143	± 0.01	± 0.01
R_{ABCD}	1.13	± 0.13	± 0.13
$R_{Z/Y}$	1.32	± 0.13	± 0.32
$R_{Z/W}$	0.95	± 0.10	± 0.10

Table 46: SR6jL: The estimated parameters with MC and errors for fit. The MC statistical error is calculated from first-order approximation of error propagation.

6.10 Purity estimation in γ CR

For the γ replace, the purity of γ +jets events in γ CR is very important. In γ CR, the main component is true γ +jets events and the rest is multi-jet events with a faking photon (fake-photon). The data-driven purity estimation is needed since the fake-photon behaviour of MCs is not reliable, because hard π^0 production in the hadronic fragmentation may not be described by the hadronization models.

The first candidate method to estimate fake-photon is ABCD method as described in Appendix C using photon ID and isolation. However, this method does not work since photon ID and isolation cut have strong correlation as described in Appendix A.2.2. The other way to estimate fake photon events is ABCD method with correction Appendix C.1. For this method, data and MC distributions are compared.

6.10.1 Data/MC comparison

For the ABCD method with correction, the good estimation of ε ($\frac{N_B}{N_A}$ or $\frac{N_C}{N_A}$ in Appendix C.1) for true photon events is needed. In this section, the MC and data are compared for the variables used in isolation cut and Tight ID cut after the Loose ID selection.

The Loose ID selections are:

- After the photon trigger
- No electron or muon
- Exact one Loose ID photon ($p_T > 130 \text{ GeV}$)
- $N_{\text{jet}}(p_T > 50 \text{ GeV}) \geq 2$

Used data correspond to $\int \text{Ldt} = 1.46 \text{ fb}^{-1}$.

The distributions of isolation variables are in Figure 48. The ε of $\frac{N_{\text{Non-Iso}}}{N_{\text{Iso}}}$ can be used since the MC to data ratio distributions are flat.

The distributions of ID related variables are shown in Figure 49 and 50. In most of variables, the MC to data ratio distributions are not flat. Especially, the MC cannot estimate the data events in the regions which are not-Tight but Loose as shown in Fig. 49. The actual boolean plots of each cut used in Tight ID are shown in Figure 51. It is clear that ε of $\frac{N_{\text{Non-Tight}}}{N_{\text{Tight}}}$ cannot be used. Therefore, the ABCD method cannot be used for the purity estimation even with correction with R (Appendix C.1).

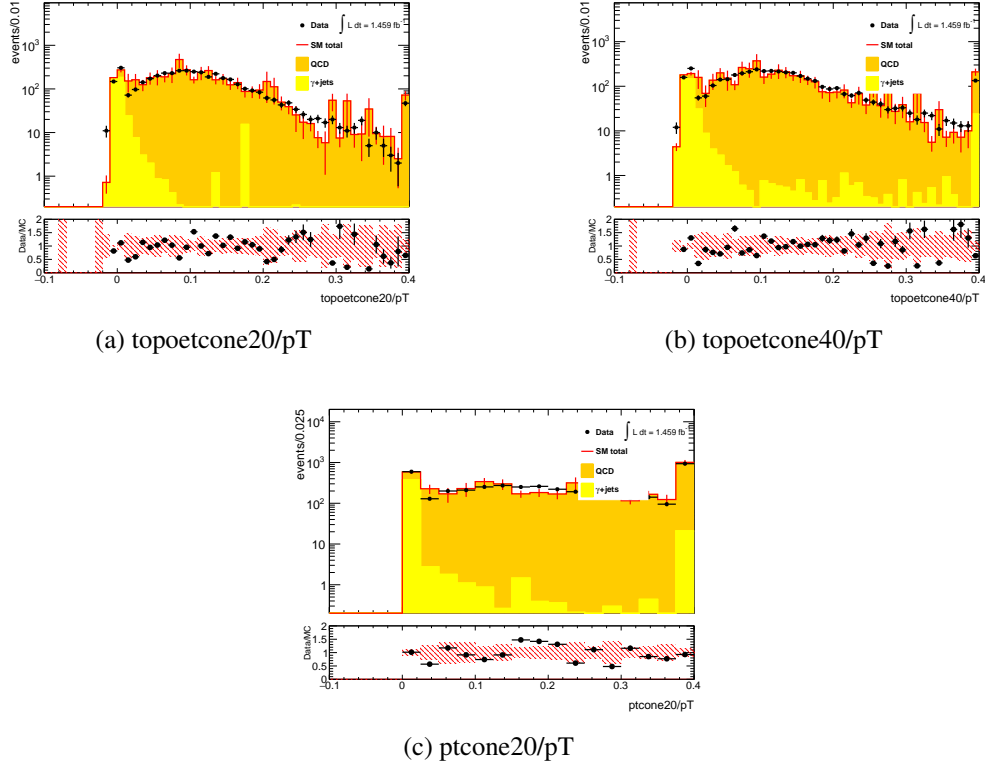


Figure 48: Distributions of isolation variables after Loose photon selection. The yellow histogram is estimated true photon MC samples, the orange histogram is estimated fake photon from QCD multi-jet MC samples, and dots are observed data events.

6.10.2 Purity estimation with isolation template fitting

From the study in previous section, we got that the MC can be used only after Tight ID cut. Therefore, the one way to estimate the purity of photons is to fit the template of isolation variables from MCs after the Tight ID cut. In the isolation cuts, two variables are used: $\text{topoetcone}X$ and $\text{ptcone}X$ as described in Sec.4.3.3. In such case, the 2D distributions should be used as template. However, in low data stat. case, we cannot prepare enough number of events for fitting. To fulfil these requirements, 2-bin template of isolation cut (iso & non-iso) is used.

To select the clean γ events, one photon and one jet events are selected:

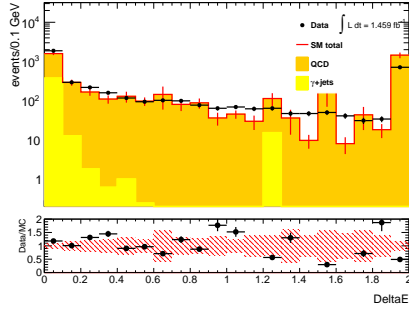
- After the one-photon trigger
- No electron or muon

- Exact one Tight ID photon ($p_T > 130 \text{ GeV}$)
- Exact one jet($p_T > 130 \text{ GeV}$) & veto 2nd jet($p_T > 50 \text{ GeV}$)
- $\Delta\phi(\text{jet}_1, \mathbf{E}_T^{\text{miss}'})_{\text{min}} > 1.0$

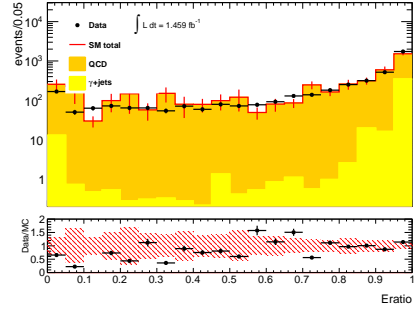
After the fit, the purity as a function of photon p_T is estimated as shown in Figure 52. As expected, the purity becomes higher as photon p_T becomes higher. In high photon p_T region, the purity is about $96\pm 2\%$. This is pure enough to neglect the fake photon contamination compared to the other systematic uncertainties. However, this is not the realistic case. It is expected that the purity becomes worse if the jets are close to a photon. Therefore, $\gamma+2\text{jet}$ events are selected:

- After the one-photon trigger
- No electron or muon
- Exact one Tight ID photon ($p_T > 130 \text{ GeV}$)
- leading jet($p_T > 130 \text{ GeV}$) & 2nd jet($p_T > 50 \text{ GeV}$) & veto 3rd jet($p_T > 50 \text{ GeV}$)
- $\Delta\phi(\text{jet}_{1,2}, \mathbf{E}_T^{\text{miss}'})_{\text{min}}$ regions : Low[0.4,2.0], High[2.0,3.14], and All[0.4,3.14]

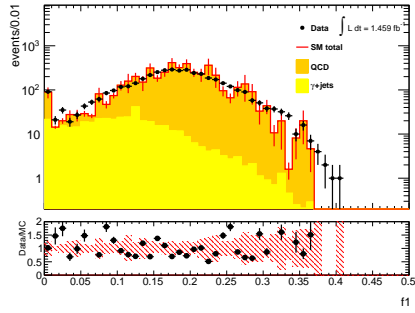
With these $\Delta\phi(\text{jet}_{1,2}, \mathbf{E}_T^{\text{miss}'})_{\text{min}}$ variations, the effect of jets near the photon is taken into account. The results of purity vs. photon p_T is shown in Figure 53. Even in the case jets are near a photon, the purity is about $96\pm 2\%$ and the contamination of fake photon is negligible.



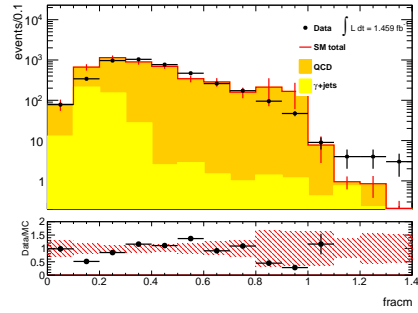
(a) DeltaE



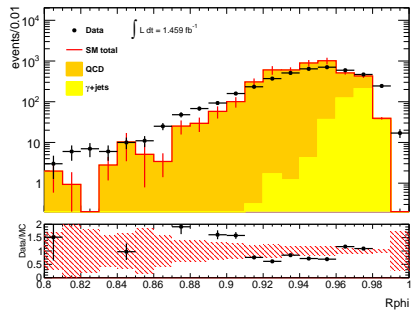
(b) Eratio



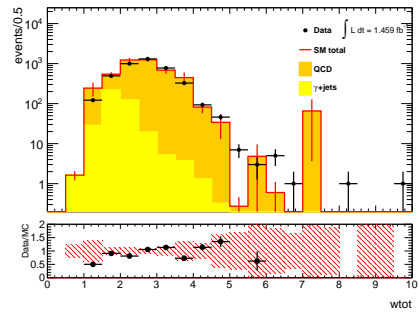
(c) f1



(d) fracm

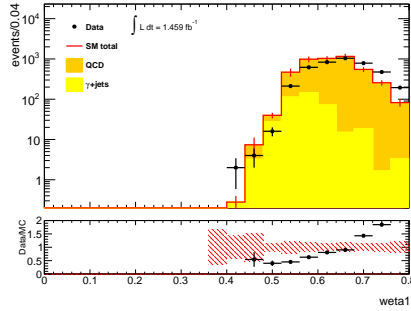


(e) Rphi

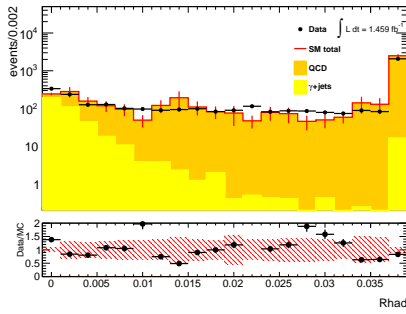


(f) wtot

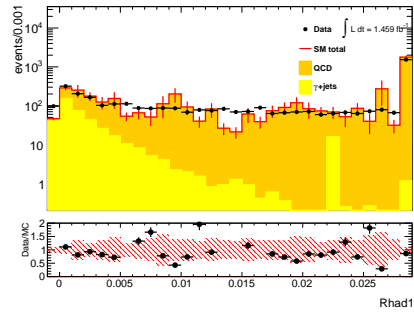
Figure 49: Distributions of ID related variables after Loose photon selection. The yellow histogram is estimated true photon MC samples, the orange histogram is estimated fake photon from QCD multi-jet MC samples, and dots are observed date events.



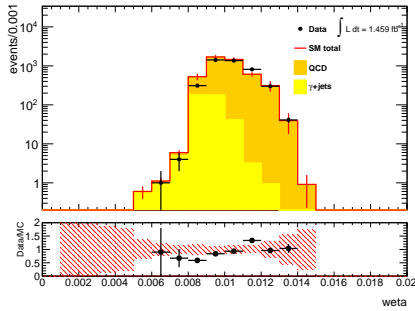
(a) weta1



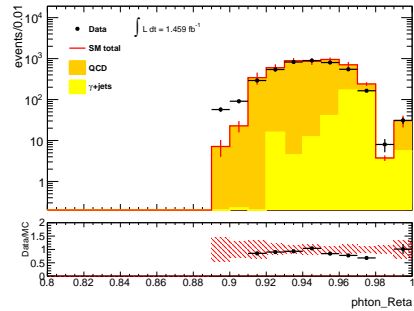
(b) Rhad (loose cut is applied in Loose ID)



(c) Rhad1 (loose cut is applied in Loose ID)



(d) weta2 (loose cut is applied in Loose ID)



(e) Reta (loose cut is applied in Loose ID)

Figure 50: Distributions of ID related variables after Loose photon selection. Except for weta1, all these variables are also used in Loose ID selection. The yellow histogram is estimated true photon MC samples, the orange histogram is estimated fake photon from QCD multi-jet MC samples, and dots are observed data events.

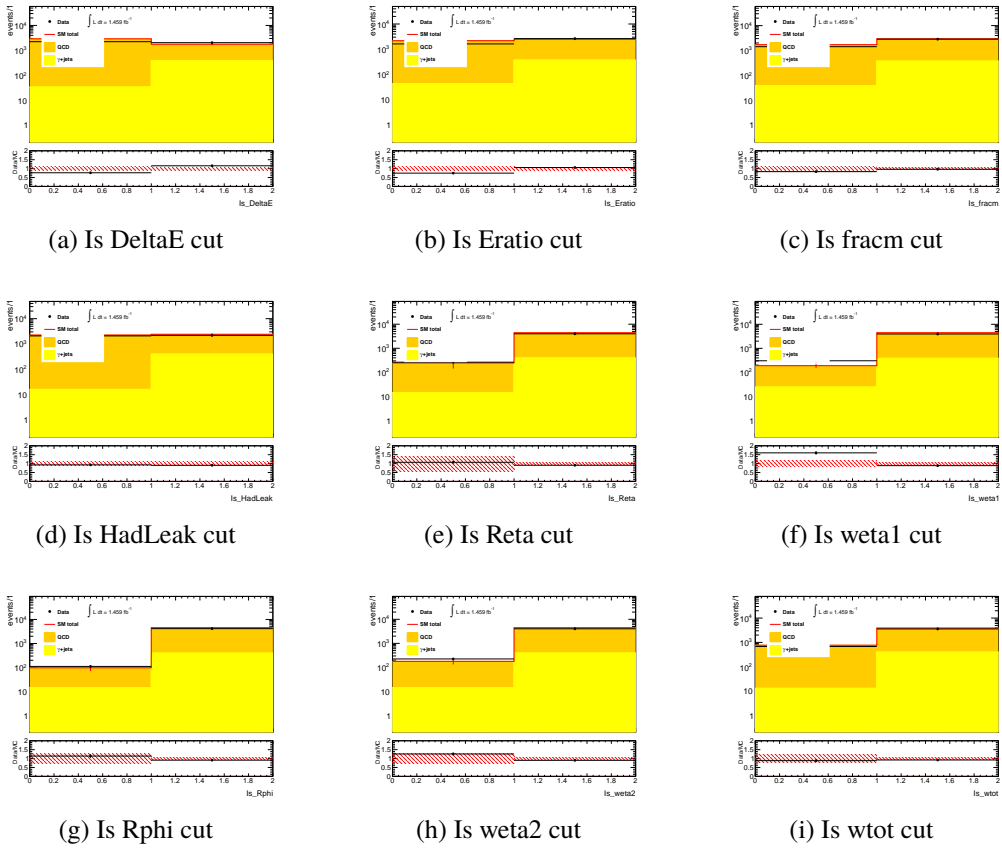


Figure 51: Distributions of boolean used in Tight ID after Loose photon selection. The yellow histogram is estimated true photon MC samples, the orange histogram is estimated fake photon from QCD multi-jet MC samples, and dots are observed data events.

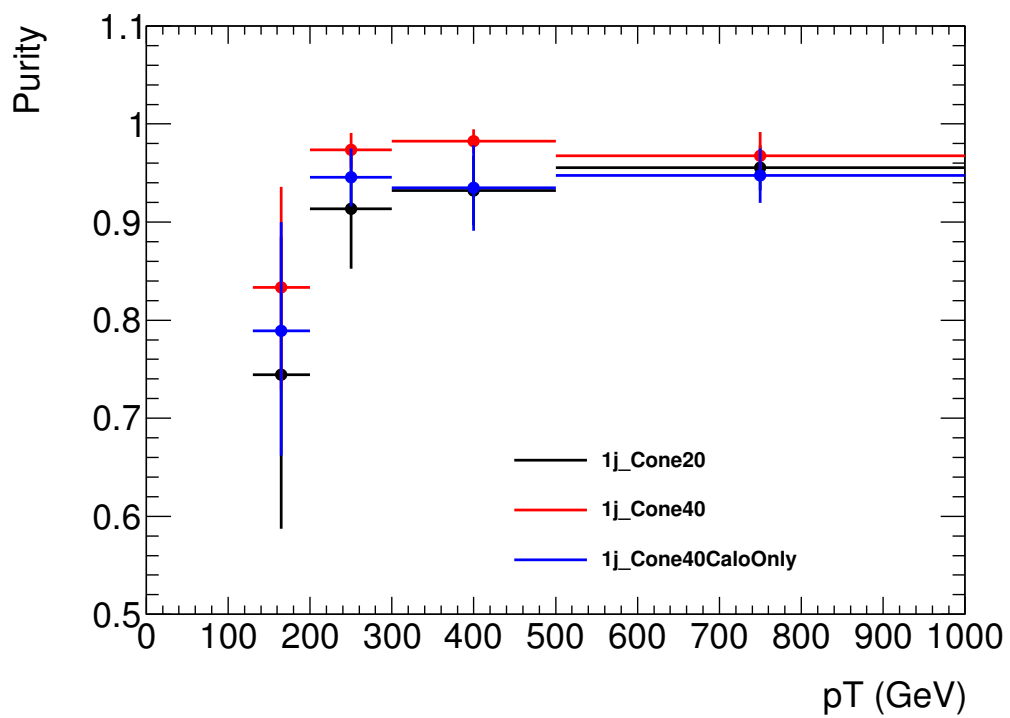


Figure 52: Purity vs. photon p_T distribution with $\gamma+1$ jet events. (Black/Red/Blue) histograms show the purity for (Cone20/Cone40/Cone40CaloOnly) isolation cut.

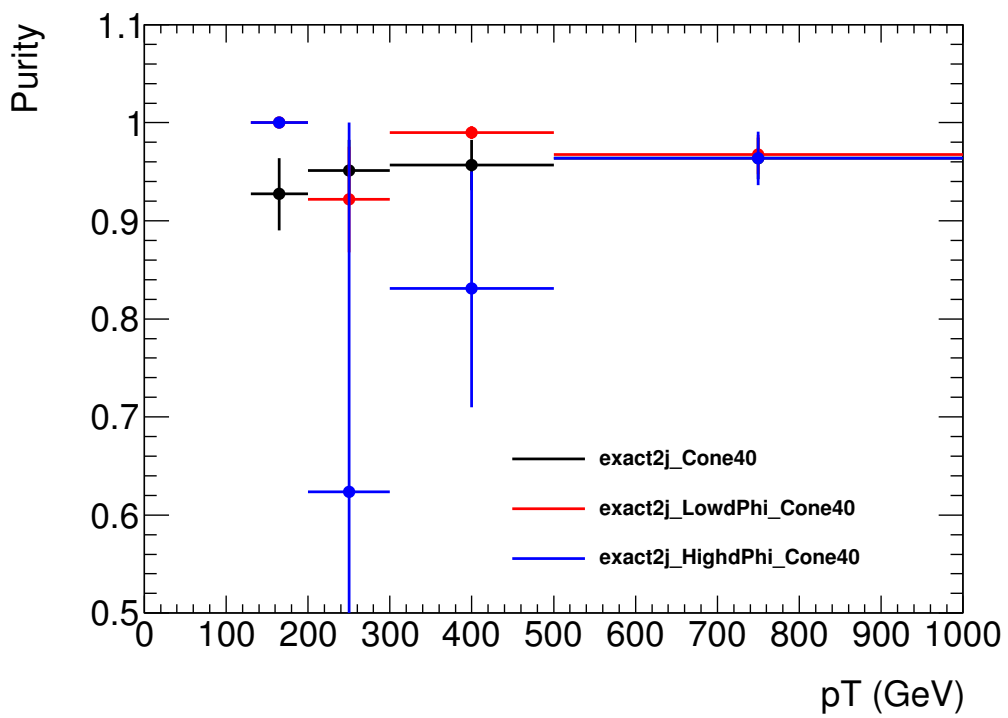


Figure 53: Purity vs. photon p_T distribution with $\gamma+2$ jet events. Isolation cut is Cone40. (Black/Red/Blue) histograms show the purity for (All/Low/High) $\Delta\phi$ region.

6.11 Summary of CRs

In previous sections, many CRs are introduced. In this section, all the CRs used in this analysis are summarized.

The classification and pre-selection of one or two leptons, one photon, and no lepton regions are summarized in Table 47. With the classification, the detailed cuts applied for each CRs are summarized in Table 48.

CR type	One photon	One lepton		Two lepton	No lepton
Target process	γ +jets	$t\bar{t} \rightarrow b\bar{b}W(qq)W(\ell\nu)$	$W(\ell\nu)$ +jets	$Z(\rightarrow \ell\ell)$ +jets	multi-jets
Trigger	one-photon	one-electron or one-muon			E_T^{miss} trigger
Cleaning	The same as SRs				
Object selection	1 signal photon, no e/μ	1 signal e/μ , $p_{T\ell} > 25\text{GeV}$		2 oposit sign signal e/μ (2nd $p_{T\ell} > 10$ GeV)	no e/μ
B-jet selection	-	$N_{Bjet} \geq 1$	$N_{Bjet} = 0$	-	-
Mass related selection	-	$30 < m_T(E_T^{\text{miss}}, \vec{p}_{T\ell}) < 100\text{ GeV}$		$66 < m_{\ell\ell} < 116\text{ GeV}$	-
Extra description	$E_T^{\text{miss}'} =$ $ E_T^{\text{miss}} + \vec{p}_{T\gamma} $ is dealt as E_T^{miss}	1. ℓ is dealt as jet 2. $E_T^{\text{miss}'} = E_T^{\text{miss}} + \vec{p}_{T\ell} $ is dealt as E_T^{miss}		$E_T^{\text{miss}'} =$ $ E_T^{\text{miss}} + \sum_{i=1}^2 \vec{p}_{T\ell,i} $ is dealt as E_T^{miss}	use normal E_T^{miss}
$E_T^{\text{miss}(')} >$	200 GeV				
$p_{T, 1st}^{\text{jet}} >$	200 GeV				
$p_{T, 2nd}^{\text{jet}} >$	50 GeV				

Table 47: Control region (CR) type classification with object. These are pre-selections for the CRs and validation regions. The used triggers are described in Sec.4.7.1.

CR name	$\Delta\phi$ cut	tight $E_T^{\text{miss}}(\prime)$ cut	m_{eff} cut	aplanarity cut	usage of the CR
CR type : one photon region					
CRYMA	+	+	+	+	fitting data-driven parameters.
CRYMa	+	+	+	-	fitting data-driven parameters.
CRYmA	+	+	-	+	fitting data-driven parameters.
CRYma	+	+	-	-	fitting data-driven parameters.
CR type : one lepton region, lepton is dealt as jet					
CRT	non	non	+	non	fitting μ_{Top} and μ_W .
CRW	non	non	+	non	fitting μ_{Top} and μ_W .
CR type : one lepton region, $E_T^{\text{miss}\prime} = E_T^{\text{miss}} + \vec{p}_{T\ell} $ is dealt as E_T^{miss}					
CRWL	+	+	-	-	fitting data-driven parameters.
CRTL	+	+	-	-	fitting μ_{TopL} .
CRWVL	non	-	-	non	fitting data-driven parameters.
CRTVL	non	-	-	non	fitting μ_{TopVL} .
CR type : two lepton region					
CRZIIL	+	+	-	-	fitting μ_{ZL} .
CRZIIVL	non	-	-	non	fitting data-driven parameters.
CR type : No lepton region					
CRQ	-	+	+	non	fitting μ_{ZL} .

Table 48: The summary table of all CRs. "+" means the cut is applied, "-" means the inverted cut is applied, and "non" means the cut is not applied to the CR.

6.12 Strategy of validation regions

To validate the background estimation method, validation regions (VRs) are needed. Before SRs are opened, the agreement between observed and estimated events in VRs are checked. The previous analyses depend more on MC simulated samples. In this analysis, numbers of events in various CRs are used, hence to justify the method, checks using validation regions are very important. Using VRs, the BG estimation method is validated quantitatively.

In (ABCD+)WXYZ method, various regions can be assigned as validation region candidates as described in Table 40. The validation regions are chosen with reasonable selection as summarized in Table 49.

6.13 Fit results for control regions and validation regions

The background only fit except for SRs is executed with maximum log likelihood method which is described afterwards in Sec.7.1. The estimated and observed events in validation regions (VRs) are checked before the unblinding of the SRs. Fit results of CRs are in Table 50-67.

The numbers of estimated events and observed events in validation regions (VRs) are in Table 58-66. The comparisons of observed estimated number of events in VRs are plotted in Figure 54-55.

The estimated events show good agreement with observed data in VRs. Therefore SRs are unblinded. The (ABCD+)WXYZ method is very complex and the method which was not used in previous analyses. The agreement in VRs shows the new possibility for the BG estimation method more reliable than the previous BG estimation methods which depend mainly on MC samples.

region	description
"No lepton" validation regions	
VRZMa	Inverted aplanarity cut is applied. Since top and W samples are normalized in tight m_{eff} CRs, this region is one of the best VRs for SR estimation. This region cannot be prepared for SR2jC, since aplanarity cut is not applied.
VRZma	Inverted m_{eff} and inverted aplanarity cut are applied. Since top and W samples are normalized only in tight m_{eff} CRs, this region is not necessarily validate the BG estimation. Therefore, this region is only used for SR2jC where VRZMa cannot be used.
"One lepton" validation regions. $E_{\text{T}}^{\text{miss}'} = \mathbf{E}_{\text{T}}^{\text{miss}} + \vec{p}_{\text{T}}^{\ell} $ is dealt as $E_{\text{T}}^{\text{miss}}$	
VRWMA	SR-like cuts are applied. This region have possibility of disagreement, since the W+jets to γ +jets ratio is determined in the region with inverted m_{eff} and inverted aplanarity cuts. However, this region is one of the best VRs since the kinematic selection is similar to SR.
VRWma	Inverted aplanarity cut is applied. This region have possibility of disagreement, since ABCD method ϵ s are determined in γ +jets region.
VRWmA	Inverted m_{eff} cut is applied. This region have possibility of disagreement, since ABCD method ϵ s are determined in γ +jets region.
Two lepton validation regions. $E_{\text{T}}^{\text{miss}'} = \mathbf{E}_{\text{T}}^{\text{miss}} + \sum_{i=1}^2 \vec{p}_{\text{T}}^{\ell,i} $ is dealt as $E_{\text{T}}^{\text{miss}}$	
VRZII	SR-like cuts are applied. This region is one of the best VRs except for the small number of events, since the kinematic selection is similar to SR selection. The possibility of disagreement is from the lepton acceptance.
VRZIIma	Inverted aplanarity cut is applied. This region have possibility of disagreement, since ABCD method ϵ s are determined in γ +jets region.
VRZIImA	Inverted m_{eff} cut is applied. This region have possibility of disagreement, since ABCD method ϵ s are determined in γ +jets region.
One photon validation regions. $E_{\text{T}}^{\text{miss}'} = \mathbf{E}_{\text{T}}^{\text{miss}} + \vec{p}_{\text{T}}^{\gamma} $ is dealt as $E_{\text{T}}^{\text{miss}}$	
CRYMA	SR-like cuts are applied. This region is the validation region for ABCD method in γ +jets region.

Table 49: The summary of validation regions (VRs). The features of each VR is described. The implementation of each VR is described in Table 40. In each VR, discrepancies between expected and observed number of events are investigated.

SR2jC channel	CRT	CRW	CRQ	CRYMA	CRYma	CRWL
Observed events	37	73	21	100	82	31
Fitted bkg events	37.00 ± 6.08	72.98 ± 8.54	21.00 ± 4.58	99.98 ± 9.68	81.96 ± 8.72	31.11 ± 5.00
Fitted Multijets events	0.00 ± 0.00	0.00 ± 0.00	16.37 ± 4.61	0.00 ± 0.00	0.00 ± 0.00	0.00 ± 0.00
Fitted Wjets events	6.62 ± 1.44	46.43 ± 9.37	0.00 ± 0.00	1.29 ± 0.36	0.00 ± 0.00	0.00 ± 0.00
Fitted Zjets events	0.09 ± 0.03	1.43 ± 0.09	0.00 ± 0.00	0.00 ± 0.00	0.00 ± 0.00	0.00 ± 0.00
Fitted GAMMAjets events	0.00 ± 0.00	0.00 ± 0.00	0.00 ± 0.00	0.00 ± 0.00	0.00 ± 0.00	0.00 ± 0.00
Fitted Top events	26.34 ± 6.55	8.10 ± 2.29	0.00 ± 0.00	0.33 ± 0.19	0.00 ± 0.00	0.00 ± 0.00
Fitted Diboson events	3.95 ± 0.39	17.02 ± 1.73	4.62 ± 0.54	0.53 ± 0.04	0.41 ± 0.16	4.71 ± 0.72
Fitted TopL events	0.00 ± 0.00	0.00 ± 0.00	0.00 ± 0.00	0.00 ± 0.00	0.44 ^{+0.66} _{-0.44}	3.12 ± 2.82
Fitted TopVL events	0.00 ± 0.00	0.00 ± 0.00	0.00 ± 0.00	0.00 ± 0.00	0.00 ± 0.00	0.00 ± 0.00
Fitted WjetsL events	0.00 ± 0.00	0.00 ± 0.00	0.00 ± 0.00	0.00 ± 0.00	1.52 ± 0.31	0.00 ± 0.00
Fitted WjetsVL events	0.00 ± 0.00	0.00 ± 0.00	0.00 ± 0.00	0.00 ± 0.00	0.00 ± 0.00	0.00 ± 0.00
Fitted ZjetsL events	0.00 ± 0.00	0.00 ± 0.00	0.00 ± 0.00	0.00 ± 0.00	0.00 ± 0.00	0.59 ± 0.32
Fitted ZjetsVL events	0.00 ± 0.00	0.00 ± 0.00	0.00 ± 0.00	0.00 ± 0.00	0.00 ± 0.00	0.00 ± 0.00
Fitted CRYMA events	0.00 ± 0.00	0.00 ± 0.00	0.00 ± 0.00	97.83 ± 9.69	0.00 ± 0.00	0.00 ± 0.00
Fitted CRYMa events	0.00 ± 0.00	0.00 ± 0.00	0.00 ± 0.00	0.00 ± 0.00	0.00 ± 0.00	0.00 ± 0.00
Fitted CRYmA events	0.00 ± 0.00	0.00 ± 0.00	0.00 ± 0.00	0.00 ± 0.00	0.00 ± 0.00	0.00 ± 0.00
Fitted CRYma events	0.00 ± 0.00	0.00 ± 0.00	0.00 ± 0.00	0.00 ± 0.00	79.58 ± 8.80	0.00 ± 0.00
Fitted CRYL events	0.00 ± 0.00	0.00 ± 0.00	0.00 ± 0.00	0.00 ± 0.00	0.00 ± 0.00	0.00 ± 0.00
Fitted CRWL events	0.00 ± 0.00	0.00 ± 0.00	0.00 ± 0.00	0.00 ± 0.00	0.00 ± 0.00	22.69 ± 5.48
Fitted CRWVL events	0.00 ± 0.00	0.00 ± 0.00	0.00 ± 0.00	0.00 ± 0.00	0.00 ± 0.00	0.00 ± 0.00
Fitted CRZiVL events	0.00 ± 0.00	0.00 ± 0.00	0.00 ± 0.00	0.00 ± 0.00	0.00 ± 0.00	0.00 ± 0.00

Table 50: **SR2jC** : Background fit results for the control regions CRT, CRW, CRQ, CRYMA, CRYma and CRWL, for an integrated luminosity of $\int L dt = 3.2 \text{ fb}^{-1}$. The errors are the statistical plus systematic uncertainties.

SR2jC channel	CRTL	CRZiIL	CRWVL	CRZiIVL	CRTVL
Observed events	9	8	4020	721	2603
Fitted bkg events	8.98 ± 2.97	8.00 ± 2.83	4018.11 ± 69.36	720.93 ± 26.35	2603.21 ± 79.46
Fitted Multijets events	0.00 ± 0.00	0.00 ± 0.00	0.00 ± 0.00	0.00 ± 0.00	0.00 ± 0.00
Fitted Wjets events	0.00 ± 0.00	0.00 ± 0.00	0.00 ± 0.00	0.00 ± 0.00	0.00 ± 0.00
Fitted Zjets events	0.00 ± 0.00	0.00 ± 0.00	0.00 ± 0.00	0.00 ± 0.00	0.00 ± 0.00
Fitted GAMMAjets events	0.00 ± 0.00	0.00 ± 0.00	0.00 ± 0.00	0.00 ± 0.00	0.00 ± 0.00
Fitted Top events	0.00 ± 0.00	0.00 ± 0.00	0.00 ± 0.00	0.00 ± 0.00	0.00 ± 0.00
Fitted Diboson events	0.67 ± 0.28	0.43 ± 0.29	324.55 ± 16.74	73.43 ± 4.37	73.97 ± 5.34
Fitted TopL events	5.89 ± 3.10	0.05 ^{+0.65} _{-0.05}	0.00 ± 0.00	0.00 ± 0.00	0.00 ± 0.00
Fitted TopVL events	0.00 ± 0.00	0.00 ± 0.00	449.64 ± 138.98	59.80 ± 17.86	2105.64 ± 617.60
Fitted WjetsL events	2.38 ± 0.81	0.00 ± 0.00	0.00 ± 0.00	0.00 ± 0.00	0.00 ± 0.00
Fitted WjetsVL events	0.00 ± 0.00	0.00 ± 0.00	0.00 ± 0.00	0.12 ^{+0.16} _{-0.12}	414.28 ^{+554.24} _{-414.28}
Fitted ZjetsL events	0.04 ± 0.02	7.53 ± 2.91	0.00 ± 0.00	0.00 ± 0.00	0.00 ± 0.00
Fitted ZjetsVL events	0.00 ± 0.00	0.00 ± 0.00	60.01 ± 7.60	0.00 ± 0.00	9.33 ± 2.75
Fitted CRYMA events	0.00 ± 0.00	0.00 ± 0.00	0.00 ± 0.00	0.00 ± 0.00	0.00 ± 0.00
Fitted CRYMa events	0.00 ± 0.00	0.00 ± 0.00	0.00 ± 0.00	0.00 ± 0.00	0.00 ± 0.00
Fitted CRYmA events	0.00 ± 0.00	0.00 ± 0.00	0.00 ± 0.00	0.00 ± 0.00	0.00 ± 0.00
Fitted CRYma events	0.00 ± 0.00	0.00 ± 0.00	0.00 ± 0.00	0.00 ± 0.00	0.00 ± 0.00
Fitted CRYL events	0.00 ± 0.00	0.00 ± 0.00	0.00 ± 0.00	0.00 ± 0.00	0.00 ± 0.00
Fitted CRWL events	0.00 ± 0.00	0.00 ± 0.00	0.00 ± 0.00	0.00 ± 0.00	0.00 ± 0.00
Fitted CRWVL events	0.00 ± 0.00	0.00 ± 0.00	3183.92 ± 152.07	0.00 ± 0.00	0.00 ± 0.00
Fitted CRZiIVL events	0.00 ± 0.00	0.00 ± 0.00	0.00 ± 0.00	587.58 ± 31.78	0.00 ± 0.00

Table 51: **SR2jC** : Background fit results for the control regions CRTL, CRZiIL, CRWVL, CRZiIVL, and CRTVL, for an integrated luminosity of $\int L dt = 3.2 \text{ fb}^{-1}$. The errors are the statistical plus systematic uncertainties.

SR4jL channel	CRT	CRW	CRQ	CRYMa	CRYma	CRYmA
Observed events	24	40	104	31	243	133
Fitted bkg events	24.01 ± 4.90	39.99 ± 6.33	104.01 ± 10.20	30.97 ± 6.38	243.13 ± 32.98	132.93 ± 18.22
Fitted Multijets events	0.00 ± 0.00	0.00 ± 0.00	95.39 ± 10.23	0.00 ± 0.00	0.00 ± 0.00	0.00 ± 0.00
Fitted Wjets events	4.05 ± 1.34	23.15 ± 7.18	0.00 ± 0.00	0.53 ± 0.21	0.00 ± 0.00	0.00 ± 0.00
Fitted Zjets events	0.07 ± 0.02	1.10 ± 0.40	0.00 ± 0.00	0.00 ± 0.00	0.00 ± 0.00	0.00 ± 0.00
Fitted GAMMAjets events	0.00 ± 0.00	0.00 ± 0.00	0.00 ± 0.00	0.00 ± 0.00	0.00 ± 0.00	0.00 ± 0.00
Fitted Top events	17.08 ± 5.33	4.87 ± 2.02	0.00 ± 0.00	0.30 ± 0.15	0.00 ± 0.00	0.00 ± 0.00
Fitted Diboson events	2.80 ± 0.36	10.87 ± 1.37	8.62 ± 0.83	0.20 ± 0.04	1.49 ± 0.21	1.17 ± 0.18
Fitted TopL events	0.00 ± 0.00	0.00 ± 0.00	0.00 ± 0.00	0.00 ± 0.00	4.20 ± 1.79	0.98 ± 0.54
Fitted TopVL events	0.00 ± 0.00	0.00 ± 0.00	0.00 ± 0.00	0.00 ± 0.00	0.00 ± 0.00	0.00 ± 0.00
Fitted WjetsL events	0.00 ± 0.00	0.00 ± 0.00	0.00 ± 0.00	0.00 ± 0.00	5.15 ± 3.64	2.78 ± 0.42
Fitted WjetsVL events	0.00 ± 0.00	0.00 ± 0.00	0.00 ± 0.00	0.00 ± 0.00	0.00 ± 0.00	0.00 ± 0.00
Fitted ZjetsL events	0.00 ± 0.00	0.00 ± 0.00	0.00 ± 0.00	0.00 ± 0.00	0.00 ± 0.00	0.00 ± 0.00
Fitted ZjetsVL events	0.00 ± 0.00	0.00 ± 0.00	0.00 ± 0.00	0.00 ± 0.00	0.00 ± 0.00	0.00 ± 0.00
Fitted CRYMA events	0.00 ± 0.00	0.00 ± 0.00	0.00 ± 0.00	0.00 ± 0.00	0.00 ± 0.00	0.00 ± 0.00
Fitted CRYMa events	0.00 ± 0.00	0.00 ± 0.00	0.00 ± 0.00	29.95 ± 6.37	0.00 ± 0.00	0.00 ± 0.00
Fitted CRYmA events	0.00 ± 0.00	0.00 ± 0.00	0.00 ± 0.00	0.00 ± 0.00	0.00 ± 0.00	127.99 ± 18.14
Fitted CRYma events	0.00 ± 0.00	0.00 ± 0.00	0.00 ± 0.00	0.00 ± 0.00	232.28 ± 33.30	0.00 ± 0.00
Fitted CRYL events	0.00 ± 0.00	0.00 ± 0.00	0.00 ± 0.00	0.00 ± 0.00	0.00 ± 0.00	0.00 ± 0.00
Fitted CRWL events	0.00 ± 0.00	0.00 ± 0.00	0.00 ± 0.00	0.00 ± 0.00	0.00 ± 0.00	0.00 ± 0.00
Fitted CRWL events	0.00 ± 0.00	0.00 ± 0.00	0.00 ± 0.00	0.00 ± 0.00	0.00 ± 0.00	0.00 ± 0.00
Fitted CRZIVL events	0.00 ± 0.00	0.00 ± 0.00	0.00 ± 0.00	0.00 ± 0.00	0.00 ± 0.00	0.00 ± 0.00

Table 52: **SR4jL** : Background fit results for the control regions CRT, CRW, CRQ, CRYMa, CRYma and CRYmA, for an integrated luminosity of $\int L dt = 3.2 \text{ fb}^{-1}$. The errors are the statistical plus systematic uncertainties.

SR4jL channel	CRWL	CRTL	CRZIL	CRWVL	CRZIVL	CRTVL
Observed events	97	78	15	680	116	1034
Fitted bkg events	97.00 ± 9.63	77.96 ± 9.35	15.01 ± 3.87	680.03 ± 57.05	116.02 ± 10.56	1033.90 ± 32.62
Fitted Multijets events	0.00 ± 0.00	0.00 ± 0.00	0.00 ± 0.00	0.00 ± 0.00	0.00 ± 0.00	0.00 ± 0.00
Fitted Wjets events	0.00 ± 0.00	0.00 ± 0.00	0.00 ± 0.00	0.00 ± 0.00	0.00 ± 0.00	0.00 ± 0.00
Fitted Zjets events	0.00 ± 0.00	0.00 ± 0.00	0.00 ± 0.00	0.00 ± 0.00	0.00 ± 0.00	0.00 ± 0.00
Fitted GAMMAjets events	0.00 ± 0.00	0.00 ± 0.00	0.00 ± 0.00	0.00 ± 0.00	0.00 ± 0.00	0.00 ± 0.00
Fitted Top events	0.00 ± 0.00	0.00 ± 0.00	0.00 ± 0.00	0.00 ± 0.00	0.00 ± 0.00	0.00 ± 0.00
Fitted Diboson events	16.45 ± 2.38	4.84 ± 0.41	4.04 ± 0.55	89.17 ± 7.56	20.20 ± 1.69	27.69 ± 2.82
Fitted TopL events	12.53 ± 4.65	59.14 ± 18.60	1.16 ± 0.60	0.00 ± 0.00	0.00 ± 0.00	0.00 ± 0.00
Fitted TopVL events	0.00 ± 0.00	0.00 ± 0.00	0.00 ± 0.00	137.89 ± 28.85	20.48 ± 4.73	895.76 ± 166.95
Fitted WjetsL events	0.00 ± 0.00	13.87 ± 13.26	0.01 ± 0.01	0.00 ± 0.00	0.00 ± 0.00	0.00 ± 0.00
Fitted WjetsVL events	0.00 ± 0.00	0.00 ± 0.00	0.00 ± 0.00	0.00 ± 0.00	0.03 ± 0.02	106.81 ^{+158.04} _{-106.81}
Fitted ZjetsL events	0.59 ± 0.24	0.11 ± 0.05	9.79 ± 3.96	0.00 ± 0.00	0.00 ± 0.00	0.00 ± 0.00
Fitted ZjetsVL events	0.00 ± 0.00	0.00 ± 0.00	0.00 ± 0.00	11.99 ± 1.82	0.00 ± 0.00	3.63 ± 0.66
Fitted CRYMA events	0.00 ± 0.00	0.00 ± 0.00	0.00 ± 0.00	0.00 ± 0.00	0.00 ± 0.00	0.00 ± 0.00
Fitted CRYMa events	0.00 ± 0.00	0.00 ± 0.00	0.00 ± 0.00	0.00 ± 0.00	0.00 ± 0.00	0.00 ± 0.00
Fitted CRYmA events	0.00 ± 0.00	0.00 ± 0.00	0.00 ± 0.00	0.00 ± 0.00	0.00 ± 0.00	0.00 ± 0.00
Fitted CRYma events	0.00 ± 0.00	0.00 ± 0.00	0.00 ± 0.00	0.00 ± 0.00	0.00 ± 0.00	0.00 ± 0.00
Fitted CRYL events	0.00 ± 0.00	0.00 ± 0.00	0.00 ± 0.00	0.00 ± 0.00	0.00 ± 0.00	0.00 ± 0.00
Fitted CRWL events	67.44 ± 10.16	0.00 ± 0.00	0.00 ± 0.00	0.00 ± 0.00	0.00 ± 0.00	0.00 ± 0.00
Fitted CRWVL events	0.00 ± 0.00	0.00 ± 0.00	0.00 ± 0.00	440.98 ± 60.77	0.00 ± 0.00	0.00 ± 0.00
Fitted CRZIVL events	0.00 ± 0.00	0.00 ± 0.00	0.00 ± 0.00	0.00 ± 0.00	75.31 ± 11.68	0.00 ± 0.00

Table 53: **SR4jL** : Background fit results for the control regions CRWL, CTRL, CRZIL, CRWVL, CRZIVL and CRTVL, for an integrated luminosity of $\int L dt = 3.2 \text{ fb}^{-1}$. The errors are the statistical plus systematic uncertainties.

SR4jM channel	CRT	CRW	CRQ	CRYMa	CRYma	CRYmA
Observed events	91	126	183	140	284	52
Fitted bkg events	90.99 ± 9.54	125.99 ± 11.23	182.97 ± 13.53	139.97 ± 24.39	283.88 ± 47.73	51.98 ± 10.72
Fitted Multijets events	0.00 ± 0.00	0.00 ± 0.00	167.47 ± 13.61	0.00 ± 0.00	0.00 ± 0.00	0.00 ± 0.00
Fitted Wjets events	16.22 ± 3.49	83.86 ± 12.42	0.00 ± 0.00	2.34 ± 0.48	0.00 ± 0.00	0.00 ± 0.00
Fitted Zjets events	0.20 ± 0.02	1.82 ± 0.15	0.00 ± 0.00	0.00 ± 0.00	0.00 ± 0.00	0.00 ± 0.00
Fitted GAMMAjets events	0.00 ± 0.00	0.00 ± 0.00	0.00 ± 0.00	0.00 ± 0.00	0.00 ± 0.00	0.00 ± 0.00
Fitted Top events	67.56 ± 10.60	15.32 ± 3.36	0.00 ± 0.00	0.98 ± 0.40	0.00 ± 0.00	0.00 ± 0.00
Fitted Diboson events	7.01 ± 0.41	25.00 ± 2.58	15.49 ± 1.45	1.05 ± 0.10	1.84 ± 0.14	0.33 ± 0.09
Fitted TopL events	0.00 ± 0.00	0.00 ± 0.00	0.00 ± 0.00	0.00 ± 0.00	4.92 ± 2.13	0.22 ± 0.19
Fitted TopVL events	0.00 ± 0.00	0.00 ± 0.00	0.00 ± 0.00	0.00 ± 0.00	0.00 ± 0.00	0.00 ± 0.00
Fitted WjetsL events	0.00 ± 0.00	0.00 ± 0.00	0.00 ± 0.00	0.00 ± 0.00	6.29 ± 4.51	0.79 ± 0.18
Fitted WjetsVL events	0.00 ± 0.00	0.00 ± 0.00	0.00 ± 0.00	0.00 ± 0.00	0.00 ± 0.00	0.00 ± 0.00
Fitted ZjetsL events	0.00 ± 0.00	0.00 ± 0.00	0.00 ± 0.00	0.00 ± 0.00	0.00 ± 0.00	0.00 ± 0.00
Fitted ZjetsVL events	0.00 ± 0.00	0.00 ± 0.00	0.00 ± 0.00	0.00 ± 0.00	0.00 ± 0.00	0.00 ± 0.00
Fitted CRYMA events	0.00 ± 0.00	0.00 ± 0.00	0.00 ± 0.00	0.00 ± 0.00	0.00 ± 0.00	0.00 ± 0.00
Fitted CRYMa events	0.00 ± 0.00	0.00 ± 0.00	0.00 ± 0.00	135.61 ± 24.38	0.00 ± 0.00	0.00 ± 0.00
Fitted CRYmA events	0.00 ± 0.00	0.00 ± 0.00	0.00 ± 0.00	0.00 ± 0.00	0.00 ± 0.00	50.64 ± 10.72
Fitted CRYma events	0.00 ± 0.00	0.00 ± 0.00	0.00 ± 0.00	0.00 ± 0.00	270.84 ± 48.10	0.00 ± 0.00
Fitted CRYL events	0.00 ± 0.00	0.00 ± 0.00	0.00 ± 0.00	0.00 ± 0.00	0.00 ± 0.00	0.00 ± 0.00
Fitted CRWL events	0.00 ± 0.00	0.00 ± 0.00	0.00 ± 0.00	0.00 ± 0.00	0.00 ± 0.00	0.00 ± 0.00
Fitted CRWVL events	0.00 ± 0.00	0.00 ± 0.00	0.00 ± 0.00	0.00 ± 0.00	0.00 ± 0.00	0.00 ± 0.00
Fitted CRZIVL events	0.00 ± 0.00	0.00 ± 0.00	0.00 ± 0.00	0.00 ± 0.00	0.00 ± 0.00	0.00 ± 0.00

Table 54: **SR4jM** : Background fit results for the control regions CRT, CRW, CRQ, CRYMa, CRYma and CRYmA, for an integrated luminosity of $\int L dt = 3.2 \text{ fb}^{-1}$. The errors are the statistical plus systematic uncertainties.

SR4jM channel	CRWL	CRTL	CRZIL	CRWVL	CRZIVL	CRTVL
Observed events	115	95	14	600	100	947
Fitted bkg events	115.12 ± 13.94	94.96 ± 10.47	14.00 ± 3.74	599.62 ± 67.87	100.12 ± 9.47	946.97 ± 30.83
Fitted Multijets events	0.00 ± 0.00	0.00 ± 0.00	0.00 ± 0.00	0.00 ± 0.00	0.00 ± 0.00	0.00 ± 0.00
Fitted Wjets events	0.00 ± 0.00	0.00 ± 0.00	0.00 ± 0.00	0.00 ± 0.00	0.00 ± 0.00	0.00 ± 0.00
Fitted Zjets events	0.00 ± 0.00	0.00 ± 0.00	0.00 ± 0.00	0.00 ± 0.00	0.00 ± 0.00	0.00 ± 0.00
Fitted GAMMAjets events	0.00 ± 0.00	0.00 ± 0.00	0.00 ± 0.00	0.00 ± 0.00	0.00 ± 0.00	0.00 ± 0.00
Fitted Top events	0.00 ± 0.00	0.00 ± 0.00	0.00 ± 0.00	0.00 ± 0.00	0.00 ± 0.00	0.00 ± 0.00
Fitted Diboson events	19.02 ± 2.26	5.23 ± 0.97	4.80 ± 0.72	75.83 ± 6.03	16.93 ± 1.11	23.67 ± 2.55
Fitted TopL events	14.25 ± 5.49	72.49 ± 23.16	1.32 ± 0.79	0.00 ± 0.00	0.00 ± 0.00	0.00 ± 0.00
Fitted TopVL events	0.00 ± 0.00	0.00 ± 0.00	0.00 ± 0.00	124.92 ± 25.16	19.00 ± 3.92	827.31 ± 142.10
Fitted WjetsL events	0.00 ± 0.00	17.13 ± 17.11	0.01 ^{+0.01} _{-0.01}	0.00 ± 0.00	0.00 ± 0.00	0.00 ± 0.00
Fitted WjetsVL events	0.00 ± 0.00	0.00 ± 0.00	0.00 ± 0.00	0.00 ± 0.00	0.03 ± 0.01	92.72 ^{+136.60} _{-92.72}
Fitted ZjetsL events	0.45 ± 0.22	0.11 ± 0.05	7.87 ± 3.91	0.00 ± 0.00	0.00 ± 0.00	0.00 ± 0.00
Fitted ZjetsVL events	0.00 ± 0.00	0.00 ± 0.00	0.00 ± 0.00	10.59 ± 1.70	0.00 ± 0.00	3.27 ± 0.65
Fitted CRYMA events	0.00 ± 0.00	0.00 ± 0.00	0.00 ± 0.00	0.00 ± 0.00	0.00 ± 0.00	0.00 ± 0.00
Fitted CRYMa events	0.00 ± 0.00	0.00 ± 0.00	0.00 ± 0.00	0.00 ± 0.00	0.00 ± 0.00	0.00 ± 0.00
Fitted CRYmA events	0.00 ± 0.00	0.00 ± 0.00	0.00 ± 0.00	0.00 ± 0.00	0.00 ± 0.00	0.00 ± 0.00
Fitted CRYma events	0.00 ± 0.00	0.00 ± 0.00	0.00 ± 0.00	0.00 ± 0.00	0.00 ± 0.00	0.00 ± 0.00
Fitted CRYL events	0.00 ± 0.00	0.00 ± 0.00	0.00 ± 0.00	0.00 ± 0.00	0.00 ± 0.00	0.00 ± 0.00
Fitted CRWL events	81.40 ± 14.40	0.00 ± 0.00	0.00 ± 0.00	0.00 ± 0.00	0.00 ± 0.00	0.00 ± 0.00
Fitted CRWVL events	0.00 ± 0.00	0.00 ± 0.00	0.00 ± 0.00	388.27 ± 70.10	0.00 ± 0.00	0.00 ± 0.00
Fitted CRZIVL events	0.00 ± 0.00	0.00 ± 0.00	0.00 ± 0.00	0.00 ± 0.00	64.16 ± 10.18	0.00 ± 0.00

Table 55: **SR4jM** : Background fit results for the control regions CRWL, CTRL, CRZIL, CRWVL, CRZIVL and CRTVL, for an integrated luminosity of $\int L dt = 3.2 \text{ fb}^{-1}$. The errors are the statistical plus systematic uncertainties.

SR6jL channel	CRT	CRW	CRQ	CRYMa	CRYma	CRYmA
Observed events	20	25	49	6	23	11
Fitted bkg events	20.00 ± 4.47	25.00 ± 5.00	48.99 ± 7.04	6.00 ± 2.64	22.96 ± 7.92	10.99 ± 4.34
Fitted Multijets events	0.00 ± 0.00	0.00 ± 0.00	46.19 ± 7.12	0.00 ± 0.00	0.00 ± 0.00	0.00 ± 0.00
Fitted Wjets events	5.24 ± 1.75	18.47 ± 5.36	0.00 ± 0.00	0.46 ± 0.24	0.00 ± 0.00	0.00 ± 0.00
Fitted Zjets events	0.05 ± 0.01	0.17 ± 0.07	0.00 ± 0.00	0.00 ± 0.00	0.00 ± 0.00	0.00 ± 0.00
Fitted GAMMAjets events	0.00 ± 0.00	0.00 ± 0.00	0.00 ± 0.00	0.00 ± 0.00	0.00 ± 0.00	0.00 ± 0.00
Fitted Top events	12.93 ± 5.01	2.10 ± 0.95	0.00 ± 0.00	0.14 ± 0.10	0.00 ± 0.00	0.00 ± 0.00
Fitted Diboson events	1.78 ± 0.20	4.26 ± 0.62	2.80 ± 0.76	0.11 ± 0.06	0.31 ± 0.12	0.12 ± 0.06
Fitted TopL events	0.00 ± 0.00	0.00 ± 0.00	0.00 ± 0.00	0.00 ± 0.00	1.23 ± 0.47	0.28 ± 0.18
Fitted TopVL events	0.00 ± 0.00	0.00 ± 0.00	0.00 ± 0.00	0.00 ± 0.00	0.00 ± 0.00	0.00 ± 0.00
Fitted WjetsL events	0.00 ± 0.00	0.00 ± 0.00	0.00 ± 0.00	0.00 ± 0.00	0.64 ± 0.21	0.20 ± 0.12
Fitted WjetsVL events	0.00 ± 0.00	0.00 ± 0.00	0.00 ± 0.00	0.00 ± 0.00	0.00 ± 0.00	0.00 ± 0.00
Fitted ZjetsL events	0.00 ± 0.00	0.00 ± 0.00	0.00 ± 0.00	0.00 ± 0.00	0.00 ± 0.00	0.00 ± 0.00
Fitted ZjetsVL events	0.00 ± 0.00	0.00 ± 0.00	0.00 ± 0.00	0.00 ± 0.00	0.00 ± 0.00	0.00 ± 0.00
Fitted CRYMA events	0.00 ± 0.00	0.00 ± 0.00	0.00 ± 0.00	0.00 ± 0.00	0.00 ± 0.00	0.00 ± 0.00
Fitted CRYMa events	0.00 ± 0.00	0.00 ± 0.00	0.00 ± 0.00	5.29 ± 2.65	0.00 ± 0.00	0.00 ± 0.00
Fitted CRYmA events	0.00 ± 0.00	0.00 ± 0.00	0.00 ± 0.00	0.00 ± 0.00	0.00 ± 0.00	10.39 ± 4.37
Fitted CRYma events	0.00 ± 0.00	0.00 ± 0.00	0.00 ± 0.00	0.00 ± 0.00	20.78 ± 7.97	0.00 ± 0.00
Fitted CRYL events	0.00 ± 0.00	0.00 ± 0.00	0.00 ± 0.00	0.00 ± 0.00	0.00 ± 0.00	0.00 ± 0.00
Fitted CRWL events	0.00 ± 0.00	0.00 ± 0.00	0.00 ± 0.00	0.00 ± 0.00	0.00 ± 0.00	0.00 ± 0.00
Fitted CRWL events	0.00 ± 0.00	0.00 ± 0.00	0.00 ± 0.00	0.00 ± 0.00	0.00 ± 0.00	0.00 ± 0.00
Fitted CRWVL events	0.00 ± 0.00	0.00 ± 0.00	0.00 ± 0.00	0.00 ± 0.00	0.00 ± 0.00	0.00 ± 0.00
Fitted CRZIVL events	0.00 ± 0.00	0.00 ± 0.00	0.00 ± 0.00	0.00 ± 0.00	0.00 ± 0.00	0.00 ± 0.00

Table 56: **SR6jL** : Background fit results for the control regions CRT, CRW, CRQ, CRYMa, CRYma and CRYmA, for an integrated luminosity of $\int L dt = 3.2 \text{ fb}^{-1}$. The errors are the statistical plus systematic uncertainties.

SR6jL channel	CRWL	CRTL	CRZIL	CRWVL	CRZIVL	CRTVL
Observed events	14	24	1	51	8	168
Fitted bkg events	14.01 ± 4.94	23.95 ± 4.88	1.10 ^{+2.70} _{-1.10}	50.93 ± 8.38	8.04 ± 2.24	168.00 ± 13.29
Fitted Multijets events	0.00 ± 0.00	0.00 ± 0.00	0.00 ± 0.00	0.00 ± 0.00	0.00 ± 0.00	0.00 ± 0.00
Fitted Wjets events	0.00 ± 0.00	0.00 ± 0.00	0.00 ± 0.00	0.00 ± 0.00	0.00 ± 0.00	0.00 ± 0.00
Fitted Zjets events	0.00 ± 0.00	0.00 ± 0.00	0.00 ± 0.00	0.00 ± 0.00	0.00 ± 0.00	0.00 ± 0.00
Fitted GAMMAjets events	0.00 ± 0.00	0.00 ± 0.00	0.00 ± 0.00	0.00 ± 0.00	0.00 ± 0.00	0.00 ± 0.00
Fitted Top events	0.00 ± 0.00	0.00 ± 0.00	0.00 ± 0.00	0.00 ± 0.00	0.00 ± 0.00	0.00 ± 0.00
Fitted Diboson events	2.44 ± 0.59	0.95 ± 0.28	0.67 ± 0.13	10.89 ± 1.60	2.76 ± 0.59	3.99 ± 0.80
Fitted TopL events	3.16 ± 1.04	20.58 ± 5.47	0.43 ± 0.28	0.00 ± 0.00	0.00 ± 0.00	0.00 ± 0.00
Fitted TopVL events	0.00 ± 0.00	0.00 ± 0.00	0.00 ± 0.00	16.92 ± 4.65	2.35 ± 0.84	147.81 ± 25.83
Fitted WjetsL events	0.00 ± 0.00	2.42 ± 2.12	0.00 ± 0.00	0.00 ± 0.00	0.00 ± 0.00	0.00 ± 0.00
Fitted WjetsVL events	0.00 ± 0.00	0.00 ± 0.00	0.00 ± 0.00	0.00 ± 0.00	0.00 ± 0.00	15.79 ^{+19.46} _{-15.79}
Fitted ZjetsL events	0.00 ± 0.10	0.00 ± 0.05	0.00 ± 2.68	0.00 ± 0.00	0.00 ± 0.00	0.00 ± 0.00
Fitted ZjetsVL events	0.00 ± 0.00	0.00 ± 0.00	0.00 ± 0.00	0.96 ± 0.18	0.00 ± 0.00	0.40 ^{+0.45} _{-0.40}
Fitted CRYMA events	0.00 ± 0.00	0.00 ± 0.00	0.00 ± 0.00	0.00 ± 0.00	0.00 ± 0.00	0.00 ± 0.00
Fitted CRYMa events	0.00 ± 0.00	0.00 ± 0.00	0.00 ± 0.00	0.00 ± 0.00	0.00 ± 0.00	0.00 ± 0.00
Fitted CRYmA events	0.00 ± 0.00	0.00 ± 0.00	0.00 ± 0.00	0.00 ± 0.00	0.00 ± 0.00	0.00 ± 0.00
Fitted CRYma events	0.00 ± 0.00	0.00 ± 0.00	0.00 ± 0.00	0.00 ± 0.00	0.00 ± 0.00	0.00 ± 0.00
Fitted CRYL events	0.00 ± 0.00	0.00 ± 0.00	0.00 ± 0.00	0.00 ± 0.00	0.00 ± 0.00	0.00 ± 0.00
Fitted CRWL events	8.42 ± 5.15	0.00 ± 0.00	0.00 ± 0.00	0.00 ± 0.00	0.00 ± 0.00	0.00 ± 0.00
Fitted CRWVL events	0.00 ± 0.00	0.00 ± 0.00	0.00 ± 0.00	22.16 ± 9.77	0.00 ± 0.00	0.00 ± 0.00
Fitted CRZIVL events	0.00 ± 0.00	0.00 ± 0.00	0.00 ± 0.00	0.00 ± 0.00	2.93 ± 2.36	0.00 ± 0.00

Table 57: **SR6jL** : Background fit results for the control regions CRWL, CTRL, CRZIL, CRWVL, CRZIVL and CRTVL, for an integrated luminosity of $\int L dt = 3.2 \text{ fb}^{-1}$. The errors are the statistical plus systematic uncertainties.

SR2jC channel	VRZma	VRZll	VRWMA
Observed events	35	5	32
Fitted bkg events	39.91 ± 7.65	6.34 ± 1.61	30.45 ± 6.98
Fitted Multijets events	0.00 ± 0.00	0.00 ± 0.00	0.00 ± 0.00
Fitted Zjets events	0.00 ± 0.00	0.00 ± 0.00	0.22 ± 0.13
Fitted Wjets events	0.00 ± 0.00	0.00 ± 0.00	0.00 ± 0.00
Fitted Top events	0.00 ± 0.00	0.15 ± 0.07	2.04 ± 1.00
Fitted Diboson events	5.13 ± 2.73	1.69 ± 1.00	6.47 ± 3.35
Fitted ZjetsL events	0.00 ± 0.00	0.00 ± 0.00	0.00 ± 0.00
Fitted TopL events	1.42 ± 1.09	0.00 ± 0.00	0.00 ± 0.00
Fitted WjetsL events	5.25 ± 0.58	0.00 ± 0.00	0.00 ± 0.00
Fitted VRZma events	28.10 ± 7.18	0.00 ± 0.00	0.00 ± 0.00
Fitted VRZll events	0.00 ± 0.00	4.51 ± 1.27	0.00 ± 0.00
Fitted VRWMA events	0.00 ± 0.00	0.00 ± 0.00	21.71 ± 6.13
MC exp. SM events	41.29	6.11	31.53
MC exp. Multijets events	0.00	0.00	0.00
MC exp. Zjets events	0.00	0.00	0.22
MC exp. Wjets events	0.00	0.00	0.00
MC exp. Top events	0.00	0.26	3.69
MC exp. Diboson events	5.13	1.69	6.47
MC exp. ZjetsL events	0.00	0.00	0.00
MC exp. TopL events	0.92	0.00	0.00
MC exp. WjetsL events	5.25	0.00	0.00
MC exp. VRZma events	29.98	0.00	0.00
MC exp. VRZll events	0.00	4.16	0.00
MC exp. VRWMA events	0.00	0.00	21.16

Table 58: **SR2jC** : Background fit results for the validation regions VRZma, VRZll, and VRWMA, for an integrated luminosity of $\int L dt = 3.2 \text{ fb}^{-1}$. Nominal MC expectations (normalised to MC cross-sections) are given for comparison. The errors are the statistical plus systematic uncertainties.

SR4jL channel	VRZMa	VRZll	VRZllmA	VRZllMa
Observed events	18	1	6	3
Fitted bkg events	17.15 ± 4.35	1.29 ± 0.50	7.01 ± 2.07	1.65 ± 0.61
Fitted Multijets events	0.09 ± 0.02	0.00 ± 0.00	0.00 ± 0.00	0.00 ± 0.00
Fitted Wjets events	2.74 ± 0.92	0.00 ± 0.00	0.00 ± 0.00	0.00 ± 0.00
Fitted Top events	1.40 ± 0.58	$0.00^{+0.01}_{-0.00}$	0.44 ± 0.28	$0.02^{+0.18}_{-0.02}$
Fitted Diboson events	5.43 ± 2.78	0.72 ± 0.43	2.09 ± 1.09	0.58 ± 0.36
Fitted TopL events	0.00 ± 0.00	0.00 ± 0.00	0.00 ± 0.00	0.00 ± 0.00
Fitted WjetsL events	0.00 ± 0.00	0.00 ± 0.00	0.00 ± 0.00	0.00 ± 0.00
Fitted VRZma events	0.00 ± 0.00	0.00 ± 0.00	0.00 ± 0.00	0.00 ± 0.00
Fitted VRZMa events	7.49 ± 3.15	0.00 ± 0.00	0.00 ± 0.00	0.00 ± 0.00
Fitted VRZmA events	0.00 ± 0.00	0.00 ± 0.00	0.00 ± 0.00	0.00 ± 0.00
Fitted VRZll events	0.00 ± 0.00	0.57 ± 0.26	0.00 ± 0.00	0.00 ± 0.00
Fitted VRZllMa events	0.00 ± 0.00	0.00 ± 0.00	0.00 ± 0.00	1.05 ± 0.44
Fitted VRZllmA events	0.00 ± 0.00	0.00 ± 0.00	4.48 ± 1.74	0.00 ± 0.00
MC exp. SM events	22.90	1.43	8.97	2.05
MC exp. Multijets events	0.07	0.00	0.00	0.00
MC exp. Wjets events	4.47	0.00	0.00	0.00
MC exp. Top events	2.69	0.01	0.84	0.04
MC exp. Diboson events	5.43	0.72	2.09	0.58
MC exp. TopL events	0.00	0.00	0.00	0.00
MC exp. WjetsL events	0.00	0.00	0.00	0.00
MC exp. VRZma events	0.00	0.00	0.00	0.00
MC exp. VRZMa events	10.24	0.00	0.00	0.00
MC exp. VRZmA events	0.00	0.00	0.00	0.00
MC exp. VRZll events	0.00	0.70	0.00	0.00
MC exp. VRZllMa events	0.00	0.00	0.00	1.43
MC exp. VRZllmA events	0.00	0.00	6.03	0.00

Table 59: **SR4jL** : Background fit results for the validation regions VRZMa, VRZll, VRZllmA, and VRZllMa, for an integrated luminosity of $\int L dt = 3.2 \text{ fb}^{-1}$. Nominal MC expectations (normalised to MC cross-sections) are given for comparison. The errors are the statistical plus systematic uncertainties.

SR4jL channel	CRYMA
Observed events	12
Fitted bkg events	16.99 ± 3.87
Fitted Wjets events	0.23 ± 0.09
Fitted Zjets events	0.00 ± 0.00
Fitted Top events	0.18 ± 0.12
Fitted Diboson events	0.24 ± 0.17
Fitted CRYMA events	16.34 ± 3.86
MC exp. SM events	11.41
MC exp. Wjets events	0.38
MC exp. Zjets events	0.00
MC exp. Top events	0.35
MC exp. Diboson events	0.24
MC exp. CRYMA events	10.44

Table 60: **SR4jL** : Background fit results for the validation region CRYMA, for an integrated luminosity of $\int L dt = 3.2 \text{ fb}^{-1}$. Nominal MC expectations (normalised to MC cross-sections) are given for comparison. The errors are the statistical plus systematic uncertainties.

SR4jL channel	VRWMA	VRWMA	VRWMA
Observed events	5	16	50
Fitted bkg events	5.54 ± 1.50	11.50 ± 3.50	42.35 ± 12.97
Fitted Multijets events	0.00 ± 0.00	0.00 ± 0.00	0.00 ± 0.00
Fitted Zjets events	0.05 ± 0.02	0.10 ± 0.03	0.36 ± 0.09
Fitted Top events	0.36 ± 0.19	1.04 ± 0.51	2.59 ± 0.96
Fitted Diboson events	1.73 ± 0.91	2.88 ± 1.56	7.40 ± 3.93
Fitted TopL events	0.00 ± 0.00	0.00 ± 0.00	0.00 ± 0.00
Fitted ZjetsL events	0.00 ± 0.00	0.00 ± 0.00	0.00 ± 0.00
Fitted VRWMA events	3.41 ± 1.16	0.00 ± 0.00	0.00 ± 0.00
Fitted VRWMA events	0.00 ± 0.00	7.49 ± 3.15	0.00 ± 0.00
Fitted VRWMA events	0.00 ± 0.00	0.00 ± 0.00	32.00 ± 12.44
MC exp. SM events	5.98	15.20	55.83
MC exp. Multijets events	0.00	0.00	0.00
MC exp. Zjets events	0.05	0.10	0.36
MC exp. Top events	0.69	1.99	4.97
MC exp. Diboson events	1.73	2.88	7.41
MC exp. TopL events	0.00	0.00	0.00
MC exp. ZjetsL events	0.00	0.00	0.00
MC exp. VRWMA events	3.52	0.00	0.00
MC exp. VRWMA events	0.00	10.24	0.00
MC exp. VRWMA events	0.00	0.00	43.10

Table 61: **SR4jL** : Background fit results for the validation regions VRWMA, VRWMA, and VRWMA, for an integrated luminosity of $\int L dt = 3.2 \text{ fb}^{-1}$. Nominal MC expectations (normalised to MC cross-sections) are given for comparison. The errors are the statistical plus systematic uncertainties.

SR4jM channel	VRZMa	VRZll	VRZllmA	VRZllMa
Observed events	68	1	4	12
Fitted bkg events	74.50 ± 13.44	1.38 ± 0.43	2.40 ± 0.64	7.48 ± 1.85
Fitted Multijets events	0.91 ± 0.14	0.00 ± 0.00	0.00 ± 0.00	0.00 ± 0.00
Fitted Wjets events	14.73 ± 2.83	0.00 ± 0.00	0.00 ± 0.00	0.01 ± 0.00
Fitted Top events	7.88 ± 1.90	0.05 ± 0.04	0.11 ± 0.07	0.42 ± 0.15
Fitted Diboson events	17.69 ± 9.01	0.57 ± 0.33	0.53 ± 0.33	2.36 ± 1.23
Fitted TopL events	0.00 ± 0.00	0.00 ± 0.00	0.00 ± 0.00	0.00 ± 0.00
Fitted WjetsL events	0.00 ± 0.00	0.00 ± 0.00	0.00 ± 0.00	0.00 ± 0.00
Fitted VRZma events	0.00 ± 0.00	0.00 ± 0.00	0.00 ± 0.00	0.00 ± 0.00
Fitted VRZMa events	33.29 ± 9.65	0.00 ± 0.00	0.00 ± 0.00	0.00 ± 0.00
Fitted VRZmA events	0.00 ± 0.00	0.00 ± 0.00	0.00 ± 0.00	0.00 ± 0.00
Fitted VRZll events	0.00 ± 0.00	0.76 ± 0.27	0.00 ± 0.00	0.00 ± 0.00
Fitted VRZllMa events	0.00 ± 0.00	0.00 ± 0.00	0.00 ± 0.00	4.69 ± 1.36
Fitted VRZllmA events	0.00 ± 0.00	0.00 ± 0.00	1.75 ± 0.54	0.00 ± 0.00
MC exp. SM events	90.52	1.51	2.97	8.75
MC exp. Multijets events	0.70	0.00	0.00	0.00
MC exp. Wjets events	18.66	0.00	0.00	0.01
MC exp. Top events	13.13	0.09	0.19	0.70
MC exp. Diboson events	17.69	0.57	0.53	2.36
MC exp. TopL events	0.00	0.00	0.00	0.00
MC exp. WjetsL events	0.00	0.00	0.00	0.00
MC exp. VRZma events	0.00	0.00	0.00	0.00
MC exp. VRZMa events	40.33	0.00	0.00	0.00
MC exp. VRZmA events	0.00	0.00	0.00	0.00
MC exp. VRZll events	0.00	0.85	0.00	0.00
MC exp. VRZllMa events	0.00	0.00	0.00	5.68
MC exp. VRZllmA events	0.00	0.00	2.25	0.00

Table 62: **SR4jM** : Background fit results for the validation regions VRZMa, VRZll, VRZllmA, and VRZllMa, for an integrated luminosity of $\int L dt = 3.2 \text{ fb}^{-1}$. Nominal MC expectations (normalised to MC cross-sections) are given for comparison. The errors are the statistical plus systematic uncertainties.

SR4jM channel	VRWMA	VRWMA	VRWmA
Observed events	9	55	13
Fitted bkg events	6.38 ± 1.53	47.68 ± 11.02	15.35 ± 4.02
Fitted Multijets events	0.00 ± 0.00	0.00 ± 0.00	0.00 ± 0.00
Fitted Zjets events	0.08 ± 0.02	0.40 ± 0.11	0.10 ± 0.04
Fitted Top events	0.42 ± 0.25	3.97 ± 1.00	0.71 ± 0.23
Fitted Diboson events	1.13 ± 0.62	10.02 ± 5.27	2.11 ± 1.22
Fitted TopL events	0.00 ± 0.00	0.00 ± 0.00	0.00 ± 0.00
Fitted ZjetsL events	0.00 ± 0.00	0.00 ± 0.00	0.00 ± 0.00
Fitted VRWMA events	4.76 ± 1.34	0.00 ± 0.00	0.00 ± 0.00
Fitted VRWMA events	0.00 ± 0.00	33.29 ± 9.65	0.00 ± 0.00
Fitted VRWmA events	0.00 ± 0.00	0.00 ± 0.00	12.43 ± 3.84
MC exp. SM events	6.10	57.38	19.39
MC exp. Multijets events	0.00	0.00	0.00
MC exp. Zjets events	0.08	0.40	0.10
MC exp. Top events	0.70	6.62	1.19
MC exp. Diboson events	1.13	10.02	2.11
MC exp. TopL events	0.00	0.00	0.00
MC exp. ZjetsL events	0.00	0.00	0.00
MC exp. VRWMA events	4.19	0.00	0.00
MC exp. VRWMA events	0.00	40.33	0.00
MC exp. VRWmA events	0.00	0.00	15.99

Table 63: **SR4jM** : Background fit results for the validation regions VRWMA, VRWMA, and VRWmA, for an integrated luminosity of $\int L dt = 3.2 \text{ fb}^{-1}$. Nominal MC expectations (normalised to MC cross-sections) are given for comparison. The errors shown are the statistical plus systematic uncertainties. The errors shown for the signal region are systematic uncertainties only.

SR4jM channel	CRYMA
Observed events	19
Fitted bkg events	22.88 ± 5.87
Fitted Wjets events	0.51 ± 0.20
Fitted Zjets events	0.00 ± 0.00
Fitted Top events	0.27 ± 0.20
Fitted Diboson events	0.25 ± 0.18
Fitted CRYMA events	21.85 ± 5.85
MC exp. SM events	14.05
MC exp. Wjets events	0.65
MC exp. Zjets events	0.00
MC exp. Top events	0.45
MC exp. Diboson events	0.25
MC exp. CRYMA events	12.70

Table 64: **SR4jM** : Background fit results for the validation region CRYMA, for an integrated luminosity of $\int L dt = 3.2 \text{ fb}^{-1}$. Nominal MC expectations (normalised to MC cross-sections) are given for comparison. The errors are the statistical plus systematic uncertainties.

SR6jL channel	VRZMa	VRZll	VRZllmA	VRZllMa
Observed events	10	0	1	2
Fitted bkg events	8.79 ± 2.33	0.25 ± 0.19	0.67 ± 0.42	0.59 ± 0.33
Fitted Multijets events	0.03 ± 0.02	0.00 ± 0.00	0.00 ± 0.00	0.00 ± 0.00
Fitted Wjets events	3.47 ± 1.32	0.00 ± 0.00	0.00 ± 0.00	0.00 ± 0.00
Fitted Top events	1.26 ± 0.69	$0.00^{+0.00}_{-0.00}$	$0.04^{+0.04}_{-0.04}$	$0.01^{+0.02}_{-0.01}$
Fitted Diboson events	2.44 ± 1.29	$0.15^{+0.15}_{-0.15}$	0.18 ± 0.13	0.35 ± 0.25
Fitted TopL events	0.00 ± 0.00	0.00 ± 0.00	0.00 ± 0.00	0.00 ± 0.00
Fitted WjetsL events	0.00 ± 0.00	0.00 ± 0.00	0.00 ± 0.00	0.00 ± 0.00
Fitted VRZma events	0.00 ± 0.00	0.00 ± 0.00	0.00 ± 0.00	0.00 ± 0.00
Fitted VRZMa events	1.59 ± 1.52	0.00 ± 0.00	0.00 ± 0.00	0.00 ± 0.00
Fitted VRZmA events	0.00 ± 0.00	0.00 ± 0.00	0.00 ± 0.00	0.00 ± 0.00
Fitted VRZll events	0.00 ± 0.00	$0.10^{+0.10}_{-0.10}$	0.00 ± 0.00	0.00 ± 0.00
Fitted VRZllMa events	0.00 ± 0.00	0.00 ± 0.00	0.00 ± 0.00	0.23 ± 0.22
Fitted VRZllmA events	0.00 ± 0.00	0.00 ± 0.00	0.44 ± 0.41	0.00 ± 0.00
MC exp. SM events	12.34	0.35	0.80	0.97
MC exp. Multijets events	0.02	0.00	0.00	0.00
MC exp. Wjets events	2.58	0.00	0.00	0.00
MC exp. Top events	3.06	0.01	0.10	0.02
MC exp. Diboson events	2.45	0.15	0.18	0.36
MC exp. TopL events	0.00	0.00	0.00	0.00
MC exp. WjetsL events	0.00	0.00	0.00	0.00
MC exp. VRZma events	0.00	0.00	0.00	0.00
MC exp. VRZMa events	4.23	0.00	0.00	0.00
MC exp. VRZmA events	0.00	0.00	0.00	0.00
MC exp. VRZll events	0.00	0.20	0.00	0.00
MC exp. VRZllMa events	0.00	0.00	0.00	0.60
MC exp. VRZllmA events	0.00	0.00	0.52	0.00

Table 65: **SR6jL** : Background fit results for the validation regions VRZMa, VRZll, VRZllmA, and VRZllMa regions, for an integrated luminosity of $\int L dt = 3.2 \text{ fb}^{-1}$. Nominal MC expectations (normalised to MC cross-sections) are given for comparison. The errors are the statistical plus systematic uncertainties.

SR6jL channel	VRWMA	VRWMA	VRWMA
Observed events	1	3	5
Fitted bkg events	1.12 ± 0.72	3.15 ± 1.66	3.89 ± 2.90
Fitted Multijets events	0.00 ± 0.00	0.00 ± 0.00	0.00 ± 0.00
Fitted Zjets events	0.01 ± 0.01	0.03 ± 0.01	0.03 ± 0.01
Fitted Top events	0.06 ± 0.06	0.38 ± 0.21	0.25 ± 0.22
Fitted Diboson events	0.33 ± 0.27	1.15 ± 0.62	0.47 ± 0.42
Fitted TopL events	0.00 ± 0.00	0.00 ± 0.00	0.00 ± 0.00
Fitted ZjetsL events	0.00 ± 0.00	0.00 ± 0.00	0.00 ± 0.00
Fitted VRWMA events	0.72 ± 0.67	0.00 ± 0.00	0.00 ± 0.00
Fitted VRWMA events	0.00 ± 0.00	1.59 ± 1.52	0.00 ± 0.00
Fitted VRWMA events	0.00 ± 0.00	0.00 ± 0.00	3.13 ± 2.86
MC exp. SM events	1.37	6.33	4.78
MC exp. Multijets events	0.00	0.00	0.00
MC exp. Zjets events	0.01	0.03	0.03
MC exp. Top events	0.15	0.92	0.61
MC exp. Diboson events	0.33	1.15	0.47
MC exp. TopL events	0.00	0.00	0.00
MC exp. ZjetsL events	0.00	0.00	0.00
MC exp. VRWMA events	0.88	0.00	0.00
MC exp. VRWMA events	0.00	4.23	0.00
MC exp. VRWMA events	0.00	0.00	3.66

Table 66: **SR6jL** : Background fit results for the validation regions VRWMA, VRWMA, and VRWMA regions, for an integrated luminosity of $\int L dt = 3.2 \text{ fb}^{-1}$. Nominal MC expectations (normalised to MC cross-sections) are given for comparison. The errors are the statistical plus systematic uncertainties.

SR6jL channel	CRYMA
Observed events	2
Fitted bkg events	2.55 ± 1.48
Fitted Wjets events	0.14 ± 0.07
Fitted Zjets events	0.00 ± 0.00
Fitted Top events	0.06 ± 0.05
Fitted Diboson events	0.00 ± 0.00
Fitted CRYMA events	2.34 ± 1.48
MC exp. SM events	2.92
MC exp. Wjets events	0.11
MC exp. Zjets events	0.00
MC exp. Top events	0.15
MC exp. Diboson events	0.00
MC exp. CRYMA events	2.66

Table 67: **SR6jL** : Background fit results for the validation region CRYMA, for an integrated luminosity of $\int L dt = 3.2 \text{ fb}^{-1}$. Nominal MC expectations (normalised to MC cross-sections) are given for comparison. The errors are the statistical plus systematic uncertainties.

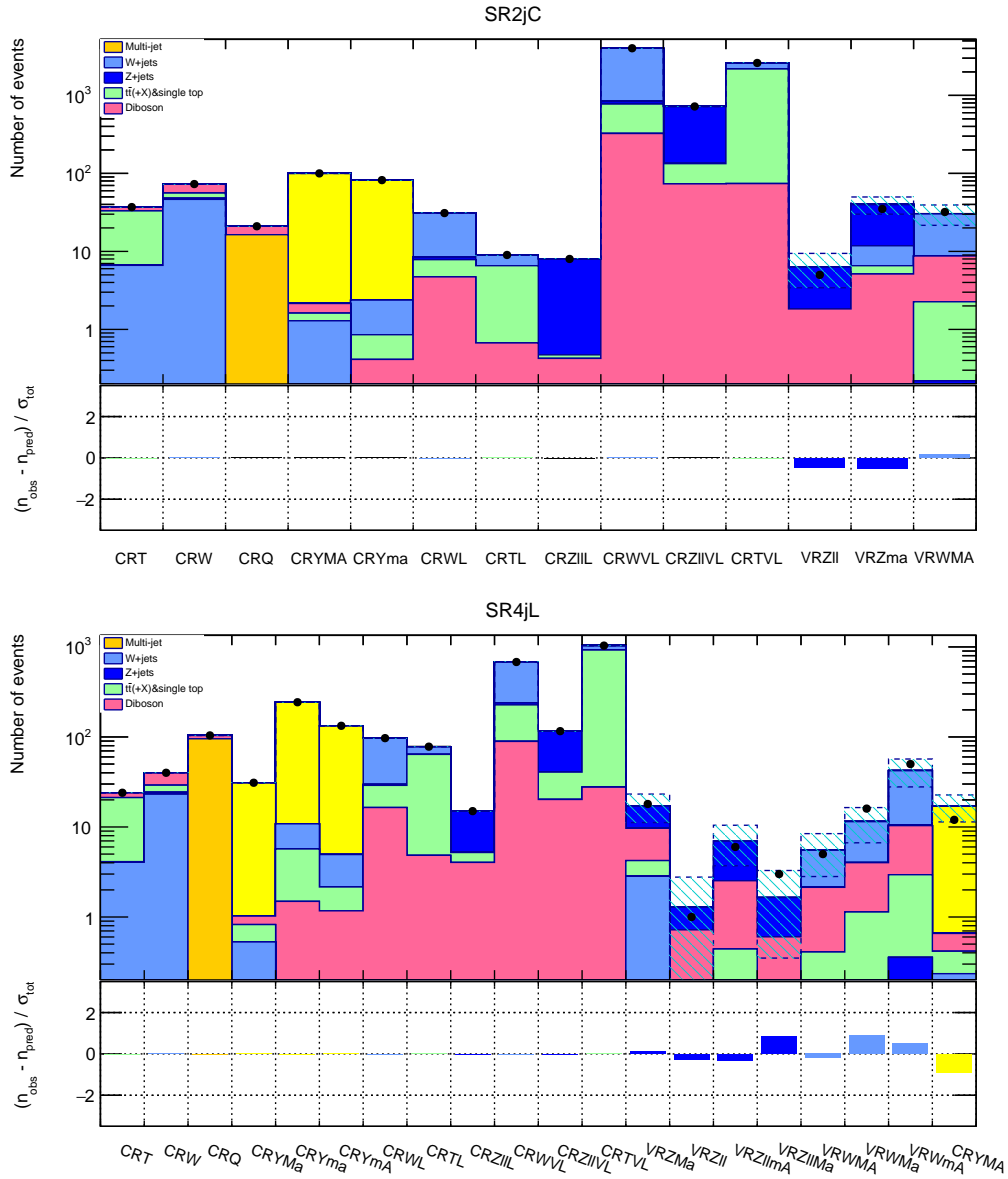


Figure 54: The comparison of expected and observed number of events in the control regions (CRs) and validation regions (VRs) for SR2jC and SR4jL. The validation regions are listed in Table 40. In upper pad, the histograms show the predicted SM number of events and the black dots show the observed number of events. The blue shaded error bands are statistical error plus systematic uncertainties. The lower pad shows the pull plots for the CRs and the VRs. The plotted value is $(n_{obs} - n_{pred}) / \sigma_{tot}$, where n_{obs} and n_{pred} are the observed and predicted number of events, and σ_{tot} is the total combination of statistical and systematic uncertainties. The error bands are plotted only for validation regions.

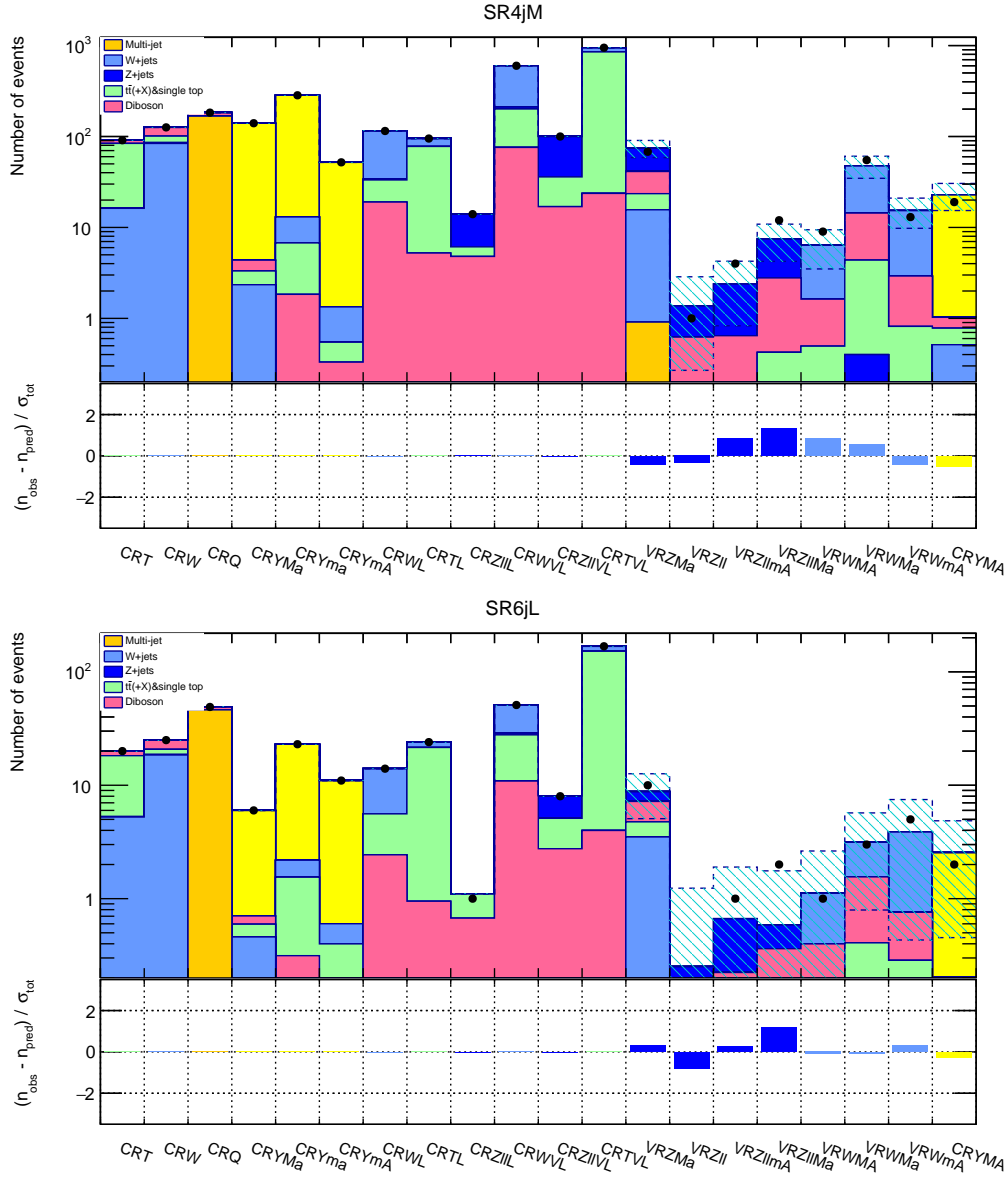


Figure 55: The comparison of expected and observed number of events in the control regions (CRs) and validation regions (VRs) for SR4jM and SR6jL. The validation regions are listed in Table 40. In upper pad, the histograms show the predicted SM number of events and the black dots show the observed number of events. The blue shaded error bands are statistical error plus systematic uncertainties. The lower pad shows the pull plots for the CRs and the VRs. The plotted value is $(n_{obs} - n_{pred}) / \sigma_{tot}$, where n_{obs} and n_{pred} are the observed and predicted number of events, and σ_{tot} is the total combination of statistical and systematic uncertainties. The error bands are plotted only for validation regions.

7 Statistical treatment

In this analysis, the SM process backgrounds (BGs) in signal region (SR) are estimated with both MC-based and data-driven method. For the BG estimation using the MC simulated SM samples, control regions (CRs) where the events of the SM processes fully dominate are prepared to normalize the difference of acceptance between data and MC. For the BG estimation using data-driven method, sufficient number of CRs are needed to estimate one SM process in SRs. The details are described in Chapter 6. To estimate the SM process BGs with CRs, a simultaneous fit in all the CRs is needed. For the evaluation of signal exclusion limit, proper statistical treatment is needed. These are processed using profile log likelihood which is described in Sec.7.1 and Sec.7.2. For the exclusion, CL_s method is used and is described in Sec.7.3. In the fit, systematic uncertainties are taken into account and are described in Sec.7.4.

7.1 Log likelihood

For simplification, at first, the case of one-bin measurement is considered. In such case, the probability density function (PDF) is

$$\mathcal{P}(n|\mu_{sig}, S, B) = \text{Pois}(n|\mu_{sig}S + B), \quad (84)$$

where n is observed number of events, μ_{sig} is signal strength, B is expected number of background events, S is expected number of signal events, and Pois is Poisson function. $\mu_{sig} = 0$ correspond to background-only hypothesis and $\mu_{sig} = 1$ correspond to signal and background hypothesis. The likelihood function L is \mathcal{P} , and the fit is executed to maximize $\log L$.

In actual measurement, there are systematic uncertainties in the expected number of events for signal and background, $B(\boldsymbol{\theta})$ and $S(\boldsymbol{\theta})$. These θ s are the parameter of systematic uncertainties and the PDF is

$$\mathcal{P}(\boldsymbol{\theta}|\boldsymbol{\theta}^0, \boldsymbol{\sigma}_{\boldsymbol{\theta}^0}) = \prod_{j \in Sys} \text{Gaus}(\theta_j^0 - \theta_j, \sigma_{\theta_j^0}), \quad (85)$$

where $\text{Gaus}(\theta_j^0 - \theta_j, \sigma_{\theta_j^0})$ is the Gaussian distribution function of θ_j around θ_j^0 with standard deviation, $\sigma_{\theta_j^0}$. Since multiple CRs are prepared in this analysis, the total likelihood function become,

$$L(\mathbf{n}|\mu_{sig}, \mathbf{S}, \mathbf{B}, \boldsymbol{\theta}) = \text{Pois}(n_{SR}|\lambda(\mu_{sig}, S, B, \boldsymbol{\theta}))_{SR} \cdot \prod_{i \in CR} \text{Pois}(n_i|\lambda(\mu_{sig}, S_i, B_i, \boldsymbol{\theta})) \cdot \prod_{j \in Sys} \text{Gaus}(\theta_j^0 - \theta_j, \sigma_{\theta_j^0}), \quad (86)$$

where λ is expected value for Poisson distribution, and λ is a function of μ_{sig} , S , B , and θ .

As described in Chapter. 6, multiple parameters are fitted in multiple CRs. Therefore, more precisely, $\lambda(\mu_{sig}, S_i, B_i, \theta)$ becomes

$$\lambda(\mu_{sig}, S_i, \boldsymbol{\mu}_{MCs}, \mathbf{B}'_{MCs}, B_i, \mu_Z, \boldsymbol{\varepsilon}, \boldsymbol{\theta}), \quad (87)$$

where \mathbf{B}'_{MCs} and $\boldsymbol{\mu}_{MCs}$ are the nominal expected numbers of events estimated from the SM process with MC samples and their normalization factors fitted in CRs, μ_Z is the expected number of events for $Z(\rightarrow \nu\nu)$ +jets in SR, and $\boldsymbol{\varepsilon}$ are the fit parameters used for the estimation of μ_Z as described in Table 39. For example in CRWL with ABCD+WXYZ method, using the Eq.(82), the expected value of Poisson is

$$\begin{aligned} \lambda(\mu_{sig}, S_i, \boldsymbol{\mu}_{MCs}, \mathbf{B}'_{MCs}, B_i, \mu_Z, \boldsymbol{\varepsilon}, \boldsymbol{\theta}) &= \mu_{sig} \cdot S_{CRWL} + \mu_{TopL} \cdot B_{CRWL}^{Top} + B_{CRWL}^{diboson} \\ &+ B_{CRWL}^{Z+jets} + (\mu_Z \cdot \varepsilon_{YMA} \cdot \varepsilon_{YMa} \cdot \varepsilon_{YMA} \cdot \varepsilon_{WL} \cdot R_{Z/Y}), \end{aligned} \quad (88)$$

where $R_{Z/Y}$ is included in $\boldsymbol{\theta}$.

7.2 Profile log likelihood

To evaluate p -value of this analysis, profile log likelihood method is used. For the evaluation of one hypothesized μ_{sig} ⁵, the profile likelihood ratio is given by

$$q_\mu = \frac{L(\mu|\hat{\boldsymbol{\theta}})}{L(\hat{\mu}|\hat{\boldsymbol{\theta}})} \quad (89)$$

where $\boldsymbol{\theta}$ is a set of the parameters including nuisance ones, $\hat{\boldsymbol{\theta}}$ is the $\boldsymbol{\theta}$ which maximize L for one given μ , and $\hat{\mu}$ and $\hat{\boldsymbol{\theta}}$ are the determined values which maximize L . If q_μ is near 1, it means good agreement between hypothesized μ value and observed data. It is much convenient to define statistic

$$t_\mu = -2 \ln q_\mu, \quad (90)$$

since q_μ moves in the range of [0,1] and t_μ moves in the range of [0, ∞]. With this transformation, q_μ exclusion can be interpreted with significance defined in one-sided test of Gaussian distribution.

Now, the discrepancy between data and μ is in proportion to t_μ . The degree of disagreement is then represented by p -value,

$$p_\mu = \int_{t_\mu^{obs}}^{\infty} f(t_\mu|\mu) dt_\mu, \quad (91)$$

⁵From this section, μ_{sig} is represented with μ

where $f(t_\mu|\mu)$ is the distribution of the t_μ as in Figure 56(a). The interpretation of p -value in significance (Z) is assuming the Gaussian distribution. The p -value from t_μ is converted to Z assuming the relation of Z and p -value in Gaussian distribution as shown in Figure 56(b).

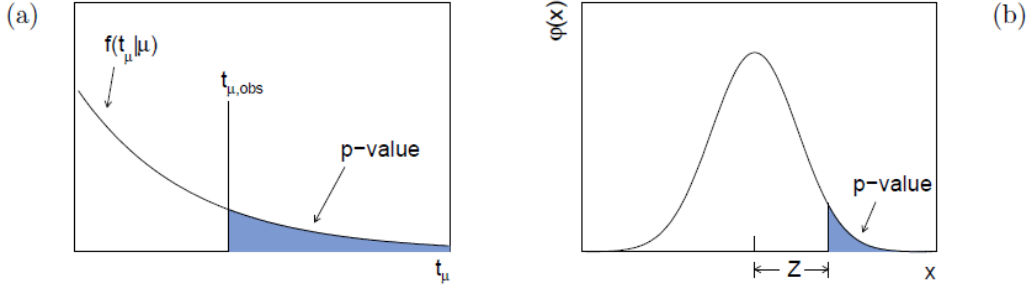


Figure 56: Distributions of statistics[66]. (a) Distribution of t_μ and the relation to p -value from the observed data. (b) Distribution of Gauss function $\phi(x) = (1/\sqrt{2\pi}) \exp(-x^2/2)$, and relation between p -value and Z (significance) is shown.

7.2.1 Approximation for discovery limit

For the discovery limit, background only hypothesis ($\mu=0$) is tested. For the simple test of discovery limit, we assume the likelihood function,

$$L(\mu) = \text{Poiss}(n|\mu S + B). \quad (92)$$

Then, the discovery q_0 become,

$$q_0 = \begin{cases} -2 \ln \frac{L(0)}{L(\hat{\mu})} & \hat{\mu} \geq 0, \\ 0 & \hat{\mu} < 0. \end{cases} \quad (93)$$

If n is approximated to be $\mu S + B$ and $\mu = 1$, significance become

$$Z_0 \simeq \sqrt{2 \left((S + B) \ln \left(\frac{S + B}{B} \right) - S \right)} \quad (94)$$

For the case $B \gg S$, this can be expanded to be

$$Z_0 \simeq \frac{S}{\sqrt{B}}. \quad (95)$$

This is widely used to evaluate significance simply.

7.3 CL_S technique

In this analysis CL_S [67] is used for the upper limit calculation.

In past, for the signal exclusion fit, p -value with $\mu = 1$ hypothesis is calculated. With such p -value (p_{S+B}), $CL_{S+B} = p_{S+B}$ is defined and used for confidence level (CL) of exclusion. This is the case for measurement with large number of events. However, this is not appropriate for number-counting measurement like this analysis. The sensitivity is evaluated with $CL_B = 1 - p_B$, where p_B is the p -value with $\mu = 0$ hypothesis. If the expected number of events in a SR is small, the $f(t_\mu|\mu)$ for $\mu = 1$ and $\mu = 0$ are similar as in Figure 57. In this case, the signal is excluded because the CL_{S+B} is small, even though the measurement has low sensitivity because the CL_B is small. To avoid this problem, CL_S technique is used. This assumes the probability of $S + B \leq N_{obs}$ under the condition, $B \leq N_{obs}$, i.e.

$$P((S + B) \leq N_{obs} | B \leq N_{obs}) = \frac{P((S + B) \leq N_{obs})}{P(B \leq N_{obs})}. \quad (96)$$

If these are interpreted to CL, CL_S is defined:

$$CL_S = \frac{CL_{S+B}}{CL_B}, \quad (97)$$

where CL_B is the CL for background only hypothesis. This CL_S is widely used in particle physics to evaluate the exclusion confidence level.

7.4 Systematic uncertainties

The origin of systematic uncertainties are classified into experimental uncertainties and theoretical uncertainties. These uncertainties are taken into account in the final fit as nuisance parameters.

7.4.1 Experimental uncertainties

The primary candidates of experimental uncertainties are luminosity uncertainty, jet energy scale (JES) uncertainty, jet energy resolution (JER), and E_T^{miss} resolution (MER) and these uncertainties are taken into account in the fit. The lepton reconstruction uncertainties and b -tag uncertainties are not considered since the effect for the SRs are expected to be negligible.

Luminosity uncertainty: The uncertainties on the integrated luminosity is $\pm 5\%$. This uncertainty is considered only in the exclusion fit.

JES uncertainty: The measurement of JES is described in Refs.[69–71]. The uncertainties are measured as a function of p_T and η of jet (Figure 58).

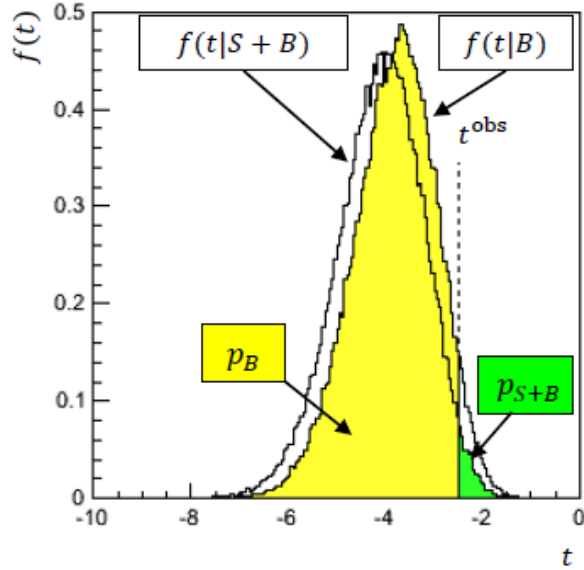


Figure 57: The distribution of the t_μ under the hypothesis of $\mu = 0$ and $\mu = 1$ [68]. $CL_B = 1 - p_B$ and $CL_{S+B} = p_{S+B}$.

JER: The measurement of JER is described in Ref.[72]. The uncertainty of JER is added in the fit.

MET SoftTerm: As described in Sec.4.6, E_T^{miss} consists of objects and "Soft-Term". The systematic uncertainties from each object are separated from "MET" uncertainty. Thus, the resolution and scale uncertainties from $E_T^{\text{miss, SoftTerm}}$ are taken into account.

7.4.2 Theoretical uncertainties

The considered theoretical uncertainties are the uncertainties from theoretical modelling of SM backgrounds with MC, the uncertainties from data-driven BG estimation (Sec. 6.5), and theoretical uncertainty of signal cross section.

MC uncertainties The theoretical uncertainties of SM MCs are evaluated with comparing the different generators. For W/Z +jets MCs, the difference of SHERPA2.1 and MADGRAPH5+PYTHIA8 is used. For $t\bar{t}$ MCs, the difference between POWHEG-BOX+PYTHIA6 and "aMC@NLO+HERWIG++", the parton showering difference between PYTHIA8 and HERWIG++, and the difference in tuning of underlying events

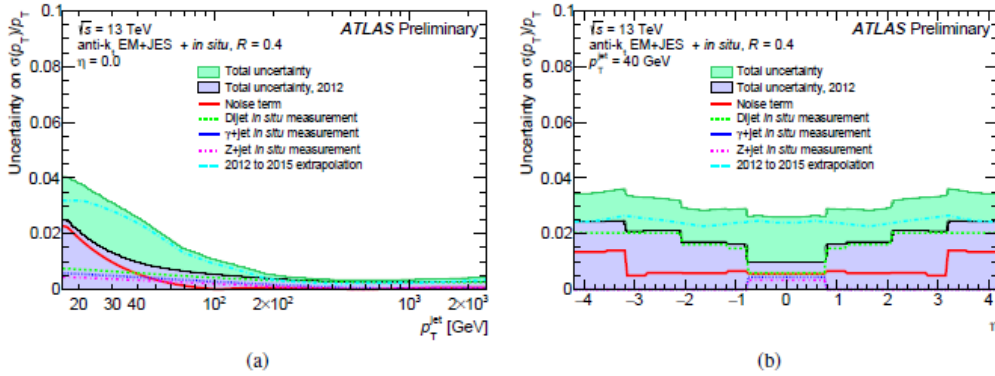


Figure 58: JES uncertainties estimated with $\sqrt{s} = 13$ TeV data with 25 ns bunch spacing[71]. The green band shows the total uncertainty for $\sqrt{s} = 13$ TeV data. The purple band shows the total uncertainty for $\sqrt{s} = 8$ TeV data (Run1). (a) shows the uncertainty as a function of p_T^{jet} in $\eta = 0$. (b) shows the uncertainty as a function of η with $p_T^{jet} = 40$ GeV.

between A14[73] and PERUGIA2012[74] are taken into account. For the MCs including diboson processes, a flat 50% scale uncertainty is applied conservatively to cover all the uncertainties including PDF uncertainty and this uncertainty is applied only in SRs and validation regions (VRs) where the background estimation method is validated. In addition to these theoretical uncertainties, statistical uncertainties of MC samples are also taken into account.

Uncertainties from data-driven BG estimation This is the uncertainty from the BG estimation method. The details of this uncertainties are described in Sec.6.5.

Signal cross section uncertainty This uncertainty consists of these three components.

- Scale uncertainty : Uncertainties from factorization and renormalization scale. Both scales are varied with factors of 0.5 and 2, and the difference from nominal is evaluated as scale uncertainties.
- PDF uncertainty : PDF are extrapolated from experimental measurement, such as HERA[75] and Tevatron. The propagation of uncertainties are evaluated with CTEQ[76] and MSTW[77] PDF sets.
- Strong coupling (α_s) uncertainty: The cross section uncertainties from α_s variation with CTEQ is considered.

8 Results

The estimated and observed events after the fits are described in 8.1. The interpretation of the results using simplified model of gluino pair-production is described in 8.2.

8.1 Fit results for signal region

The observed events and expected events of **SR2jC**, **SR4jL**, **SR4jM**, **SR6jL** are summarized in Table 68. The breakdown of dominant systematic errors in each

Signal regions	SR2jL	SR4jL	SR4jM	SR6jL
Observed events	45	12	14	4
Fitted bkg events	44.51 ± 9.37	9.21 ± 2.39	11.45 ± 2.40	2.79 ± 0.96
Fitted Multijets events	0.06 ± 0.02	$0.01^{+0.02}_{-0.01}$	$0.01^{+0.01}_{-0.01}$	0.11 ± 0.04
Fitted Wjets events	5.51 ± 1.20	1.66 ± 0.74	2.58 ± 0.99	1.20 ± 0.53
Fitted Top events	1.34 ± 0.68	0.78 ± 0.41	1.19 ± 0.30	0.28 ± 0.21
Fitted Diboson events	10.70 ± 5.40	2.67 ± 1.37	2.31 ± 1.19	0.49 ± 0.26
Fitted Z_SR events	26.89 ± 7.57	4.08 ± 1.84	5.36 ± 1.92	$0.70^{+0.74}_{-0.70}$
MC exp. SM events	46.69	11.91	13.60	3.56
MC exp. Multijets events	0.04	0.01	0.01	0.10
MC exp. Wjets events	8.72	2.71	3.28	0.89
MC exp. Top events	2.43	1.50	1.99	0.66
MC exp. Diboson events	10.70	2.67	2.31	0.49
MC exp. Z_SR events	24.80	5.02	6.02	1.41

Table 68: Background fit results for the Signal regions for an integrated luminosity of $\int L dt = 3.2 \text{ fb}^{-1}$. Nominal MC expectations (normalised to MC cross-sections) are given for comparison.

SR is summarized in Table 69 -72.

The distributions of m_{eff} and aplanarity in each signal region are shown in Figure 59-60. The distribution of Z+jets events in SR is evaluated from the distribution of γ +jets events in CRYMA region with normalization factor ($1/\epsilon_{YMA}$). These are not the actual estimated number of events for SR4jL, SR4jM, and SR6jL, because the number of events in CRYMA is estimated with ABCD method.

Since significant excess is not observed, model independent upper limits are calculated conservatively. The summary of limits are in Table 73. It shows 95%

Uncertainty of channel	SR_cuts
Total background expectation	44.51
Total statistical error ($\sqrt{N_{\text{exp}}}$)	± 6.67
Total background systematic error	± 9.37 [21.05%]
μ_Z	± 7.57 [17.0%]
Systematics Dibosons	± 5.35 [12.0%]
JES	± 1.35 [3.04%]
μ_{Wjets}	± 1.15 [2.6%]
MC statistics	± 0.74 [1.7%]
Generator Top	± 0.58 [1.3%]
Generator W	± 0.35 [0.79%]
μ_{Top}	± 0.34 [0.77%]
Top radiation	± 0.13 [0.30%]
Top tuning	± 0.13 [0.30%]
MET SoftTerm	± 0.12 [0.27%]
JER	± 0.11 [0.26%]
$\mu_{Multijets}$	± 0.02 [0.04%]
Top fragmentation	± 0.01 [0.02%]

Table 69: Breakdown of the dominant systematic uncertainties in the estimated number of background events in SR2jC. Note that the uncertainties can be correlated, and do not necessarily add up quadratically to the total background uncertainty. The percentages show the size of the uncertainty relative to the total expected background.

Uncertainty of channel	SR_cuts
Total background expectation	9.21
Total statistical error ($\sqrt{N_{\text{exp}}}$)	± 3.03
Total background systematic error	± 2.39 [25.98%]
μ_Z	± 1.84 [20.0%]
Systematics Dibosons	± 1.33 [14.5%]
μ_{Wjets}	± 0.54 [5.9%]
Generator W	± 0.48 [5.3%]
MC statistics	± 0.38 [4.1%]
JES	± 0.37 [4.0%]
Generator Top	± 0.31 [3.3%]
μ_{Top}	± 0.25 [2.7%]
Top fragmentation	± 0.14 [1.5%]
MET SoftTerm	± 0.12 [1.31%]
Top tuning	± 0.08 [0.85%]
Top radiation	± 0.08 [0.85%]
JER	± 0.06 [0.66%]
$\mu_{Multijets}$	± 0.00 [0.03%]

Table 70: Breakdown of the dominant systematic uncertainties in the estimated number of background events in SR4jL. Note that the uncertainties can be correlated, and do not necessarily add up quadratically to the total background uncertainty. The percentages show the size of the uncertainty relative to the total expected background.

Uncertainty of channel	SR_cuts
Total background expectation	11.45
Total statistical error ($\sqrt{N_{\text{exp}}}$)	± 3.38
Total background systematic error	± 2.40 [21.01%]
μ_Z	± 1.92 [16.7%]
Systematics Dibosons	± 1.15 [10.1%]
Generator W	± 0.81 [7.0%]
MC statistics	± 0.42 [3.6%]
μ_{Wjets}	± 0.40 [3.5%]
JES	± 0.39 [3.4%]
JER	± 0.24 [2.1%]
μ_{Top}	± 0.19 [1.7%]
Top radiation	± 0.12 [1.0%]
Top tuning	± 0.12 [1.0%]
Generator Top	± 0.11 [0.92%]
MET SoftTerm	± 0.03 [0.27%]
Top fragmentation	± 0.02 [0.17%]
$\mu_{Multijets}$	± 0.00 [0.01%]

Table 71: Breakdown of the dominant systematic uncertainties in the estimated number of background events in SR4jM. Note that the uncertainties can be correlated, and do not necessarily add up quadratically to the total background uncertainty. The percentages show the size of the uncertainty relative to the total expected background.

Uncertainty of channel	SR_cuts
Total background expectation	2.79
Total statistical error ($\sqrt{N_{\text{exp}}}$)	± 1.67
Total background systematic error	± 0.96 [34.54%]
μ_Z	± 0.74 [26.4%]
$\mu_{W \text{ jets}}$	± 0.36 [12.8%]
Generator W	± 0.32 [11.3%]
MC statistics	± 0.28 [9.9%]
Systematics Dibosons	± 0.25 [8.8%]
Generator Top	± 0.17 [6.0%]
μ_{Top}	± 0.11 [3.9%]
JES	± 0.09 [3.4%]
MET SoftTerm	± 0.05 [1.7%]
Top fragmentation	± 0.04 [1.5%]
$\mu_{Multijets}$	± 0.04 [1.4%]
Top radiation	± 0.03 [1.0%]
Top tuning	± 0.03 [1.0%]
JER	± 0.03 [0.97%]

Table 72: Breakdown of the dominant systematic uncertainties in the estimated number of background events in SR6jL. Note that the uncertainties can be correlated, and do not necessarily add up quadratically to the total background uncertainty. The percentages show the size of the uncertainty relative to the total expected background.

Signal channel	$\langle \epsilon\sigma \rangle_{\text{obs}}^{95}$ [fb]	S_{obs}^{95}	S_{exp}^{95}	CL_B	$p(s = 0)$
SR2jC	7.45	23.9	$23.5^{+7.5}_{-5.4}$	0.52	0.47
SR4jL	3.47	11.1	$9.1^{+3.9}_{-2.8}$	0.71	0.25
SR4jM	3.67	11.8	$10.0^{+4.3}_{-2.9}$	0.68	0.29
SR6jL	1.98	6.4	$5.7^{+2.6}_{-1.7}$	0.66	0.30

Table 73: Left to right: 95% CL upper limits on the visible cross section ($\langle \epsilon\sigma \rangle_{\text{obs}}^{95}$) and on the number of signal events (S_{obs}^{95}). The third column (S_{exp}^{95}) shows the 95% CL upper limit on the number of signal events, given the expected number (and $\pm 1\sigma$ excursions on the expectation) of background events. The last two columns indicate the CL_B value, i.e. the confidence level observed for the background-only hypothesis, and the discovery p -value ($p(s = 0)$).

CL upper limits to visible cross section ($\langle \epsilon\sigma \rangle_{\text{obs}}^{95}$), observed number of signal events (S_{obs}^{95}), expected number of signal events (S_{exp}^{95}), and the p_0 value.

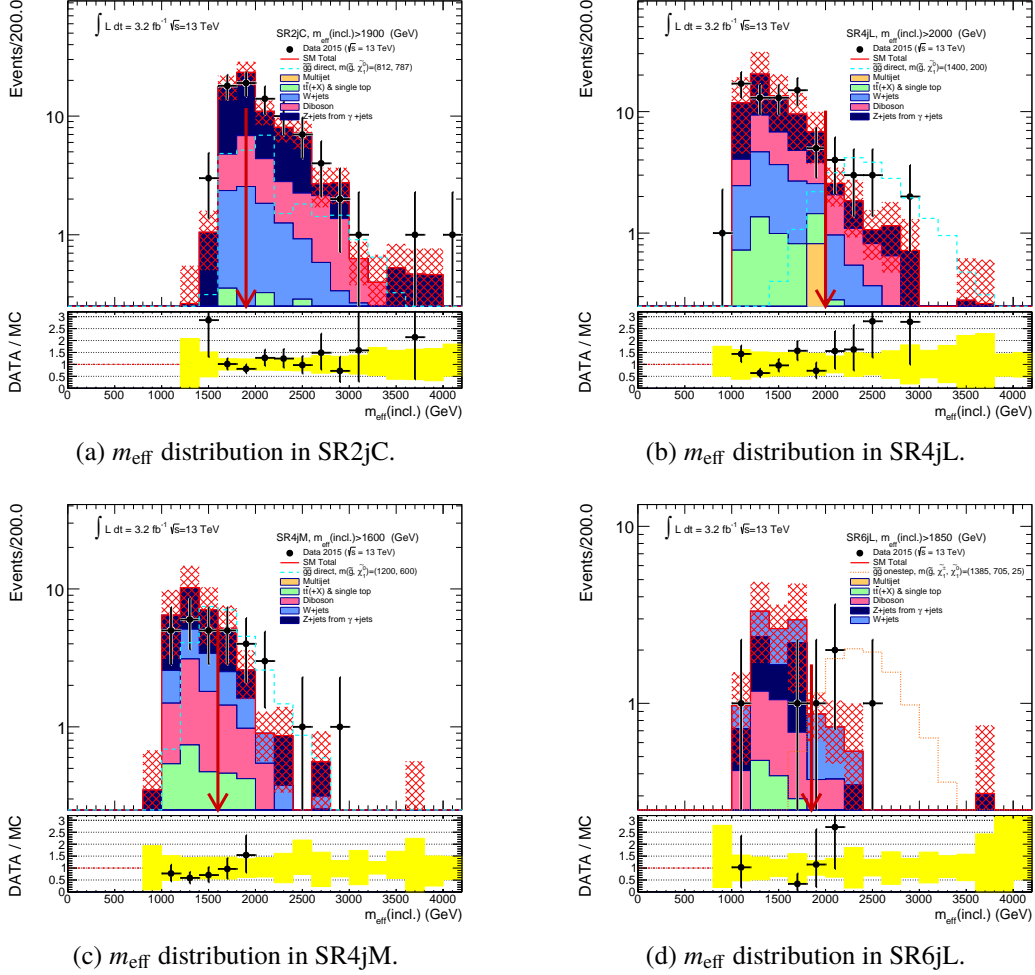
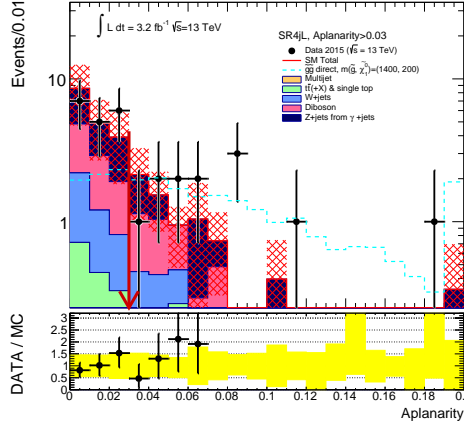
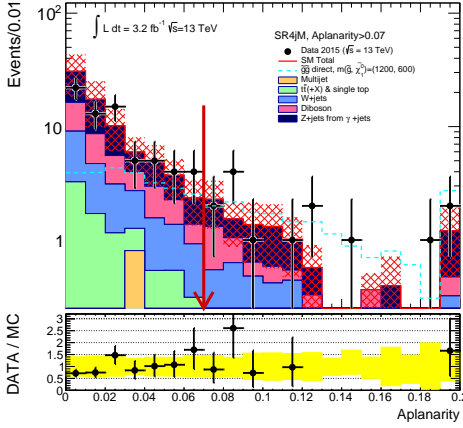


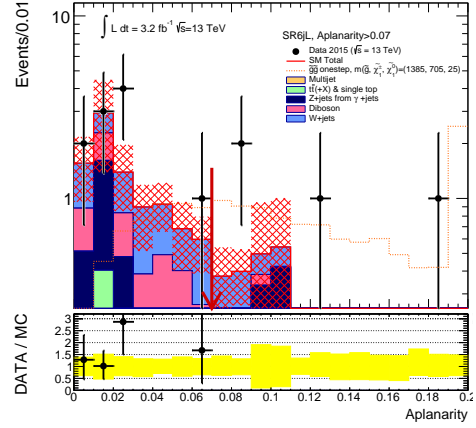
Figure 59: m_{eff} distributions in each SR before the m_{eff} cut (shown with red arrow). The black dots show the observed data events. The red histogram show the total SM backgrounds. The dashed lines show the expected signal histograms from MC simulation. The normalization of top, W, and multi-jet samples are from the fit results. The m_{eff} distributions of Z+jets samples are evaluated from γ +jets events in CRYMA region, and the normalization factor is the inverse of ε_{YMA} . The red shaded band in SM Total and yellow band in ratio plot show the total combined error of the MC statistical error, systematic errors, fitting error in normalization factor, and data statistical error in γ +jets events. Systematic errors are generator uncertainties and JES uncertainty as described in Sec.7.4. Errors in the normalization factors and systematic uncertainties are applied independently, though they have correlation. Therefore the errors become larger than the actual ones. In SR4jL, SR4jM, SR6jL, the number of events in CRYMA is estimated with ABCD method, and hence the errors from data statistics in Z+jets (γ +jets) become larger than actual ones.



(a) aplanarity distribution in SR4jL.



(b) aplanarity distribution in SR4jM.



(c) aplanarity distribution in SR6jL.

Figure 60: Aplanarity distributions in each SR before the aplanarity cut (shown with red arrow). The black dots show the observed data events. The red histogram show the total SM backgrounds. The dashed lines show the expected signal histograms from MC simulation. The normalization of top, W, and multi-jet samples are from the fit results. The aplanarity distributions of Z+jets samples are evaluated from γ +jets events in CRYMA region, and the normalization factor is the inverse of ε_{YMA} . The red shaded band in SM Total and yellow band in ratio plot show the total combined error of the MC statistical error, systematic errors, fitting error in normalization factor, and data statistical error in γ +jets events. Systematic errors are generator uncertainties and JES uncertainty as described in Sec.7.4. Errors in the normalization factors and systematic uncertainties are applied independently, though they have correlation. Therefore the errors become larger than the actual ones. In **SR4jL**, **SR4jM**, **SR6jL**, the number of events in CRYMA is estimated with ABCD method, and hence the errors from data statistics in Z+jets (γ +jets) become larger than actual ones.

8.2 Interpretations and discussions

The Figure 61 shows the limit for the gluino direct-decay simplified model. For the case $m(\tilde{\chi}_1^0) = 0$, the gluino mass is excluded up to 1530 GeV. The comparison with the CMS Run1 analysis with M_{T2} variable[78] is shown in Figure 62.

The Figure 63 shows the limit for the gluino onestep-decay simplified model. For the case $m(\tilde{\chi}_1^0) = 0$, the gluino mass is excluded up to 1510 GeV. There is no results from the Run1 CMS experiment with the same signal samples. As a reference, the results of the Run1 CMS experiment using different gluino onestep-decay simplified model is shown in Figure 64. The model include neutral Next to Lightest SUSY Particle(NLSP) which decays into Z in addition to the onestep-decay simplified model of this thesis.

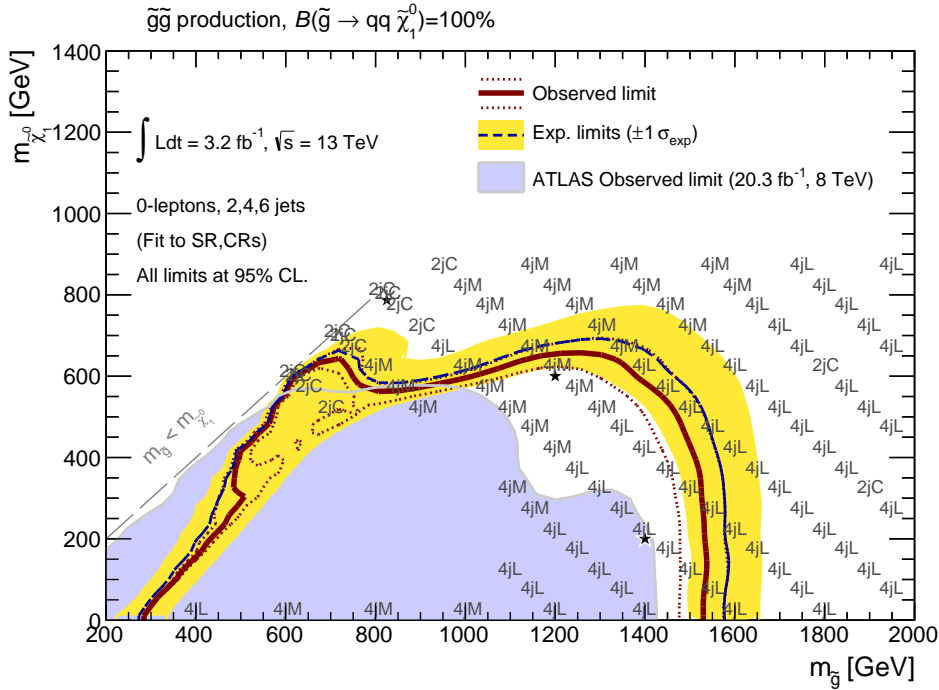


Figure 61: Exclusion contour with 95% CL for gluino pair-production with gluino decaying directly into LSP and quarks. The blue dashed contour and yellow band show the expected limit with 1σ excursion with systematic uncertainties. The red solid and dotted contours show the observed limit with 1σ excursion with signal theoretical uncertainties. The pale purple region shows the observed limit from the ATLAS Run1 analyses[79]. The stars are from optimized point $(m(\tilde{g}), m(\tilde{\chi}_1^0))$ of SR4jL, SR2jL, SR4jM .

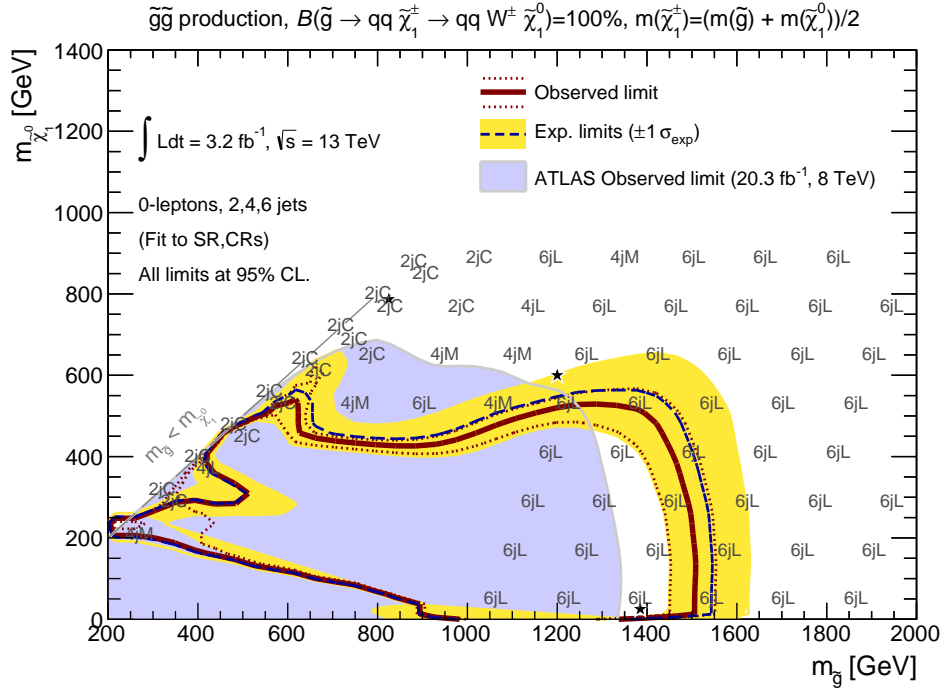


Figure 63: Exclusion contour with 95% CL for gluino pair-production in onestep-decay model. Each gluino decays into $q\bar{q} \tilde{\chi}_1^\pm$ and $\tilde{\chi}_1^\pm$ decays into $W \tilde{\chi}_1^0$. The assumed mass relation is $m(\tilde{\chi}_1^\pm) = (m(\tilde{g}) + m(\tilde{\chi}_1^0))/2$. The red solid and dotted contours show the observed limit with 1σ excursion with signal theoretical uncertainties. The blue dashed contour and yellow band show the expected limit with 1σ excursion with systematic uncertainties. The pale purple region shows the observed limit from the ATLAS Run1 analyses[18]. The stars are from optimized point $(m(\tilde{g}), m(\tilde{\chi}_1^0))$ of **SR6jLSR2jL**, **SR4jM**, **SR2jL**.

In the gluino onestep-decay model, the mass points around $m(\tilde{g}) : m(\tilde{\chi}_1^\pm) : m(\tilde{\chi}_1^0) \sim 900 : 700 : 500$ are not excluded whereas the region is excluded in Run1 analysis. These regions are not typical mass regions and dedicated SRs are not prepared. In such region, large E_T^{miss} is not efficient since mass gaps of gauginos are very small. Therefore, a SR with much smaller E_T^{miss} cut will be needed. In the case, the other BG estimation will be needed since data-driven γ replacement is effective only for high E_T^{miss} region SM background estimation. Therefore, in future analysis with large integrated luminosity, the low E_T^{miss} region dedicated for the small mass gap regions will be needed.

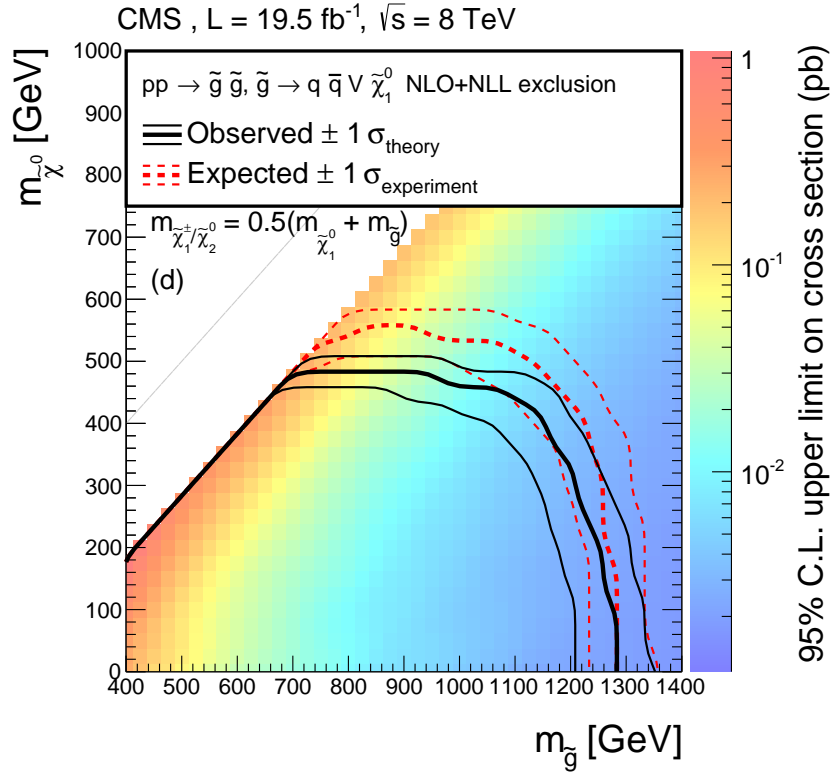


Figure 64: Exclusion contour with 95% CL for gluino pair-production in onestep-decay model from the CMS experiment Run1 analysis[80]. Each gluino decays into $q\bar{q} + \tilde{\chi}_1^\pm/\tilde{\chi}_2^0$ and $\tilde{\chi}_1^\pm/\tilde{\chi}_2^0$ decays into $W/Z + \tilde{\chi}_1^0$. The assumed mass relation is $m(\tilde{\chi}_1^\pm/\tilde{\chi}_2^0) = (m(\tilde{g}) + m(\tilde{\chi}_1^0))/2$. The black solid and dotted contours show the observed limit with 1σ excursion with signal theoretical uncertainties. The red solid and dotted contours show the expected limit with 1σ excursion with systematic uncertainties.

9 Conclusion

This thesis reports a search for gluino pair-production in proton-proton collision at $\sqrt{s} = 13$ TeV with an integrated luminosity of 3.2 fb^{-1} recorded by the ATLAS detector at CERN. Gluino pair-production is searched for using events with large E_T^{miss} , jets, and no lepton in the final states of the proton-proton collisions.

To optimize the event selection for non-planar multi-jet events, a variable "aplanarity" is newly introduced, which results in better signal sensitivity over the previous searches. Four signal regions (SRs) are prepared for gluino pair production search. SR2jC is the SR for the case $m(\tilde{\chi}_1^0)$ is close to $m(\tilde{g})$. SR4jL is the SR for the case difference between $m(\tilde{g})$ and $m(\tilde{\chi}_1^0)$ is large. SR4jM is the SR for the case $m(\tilde{g}) \sim 2m(\tilde{\chi}_1^0)$. SR6jL is the SR for the case difference between $m(\tilde{g})$ and $m(\tilde{\chi}_1^0)$ is large in the simplified model of gluino onestep-decay.

A new method to evaluate number of background (BG) events using the real data is applied in this analysis. For the claim of discovery of SUSY signal, data-driven BG estimation method is important. Therefore, a BG estimation method which does not rely on the MC simulation as much as possible is devised and applied. The number of events estimated with the method and that of observed data shows good agreement. This means the new BG estimation method is evaluated to be effective.

No significant excess is observed in SRs. The exclusion of SUSY signals is interpreted using simplified models in which gluinos are pair-produced and each gluino decays into two quarks and an electroweakino. In gluino direct-decay model in which the electroweakino is LSP, gluinos with masses up to 1530 GeV are excluded for the massless LSP at 95% CL. This result is also interpreted with gluino onestep-decay simplified model in which the electroweakino is $\tilde{\chi}_1^\pm$ and $\tilde{\chi}_1^\pm$ decays into W and LSP. For the massless LSP, gluinos with masses up to 1510 GeV is excluded at 95% CL.

In some typical mass spectrum described in the introduction (Sec.1.3.2) like $m(\tilde{g}) : m(\tilde{\chi}_1^0) = 6:1$ or $7:1$, the gluinos with masses up to ~ 1510 GeV are excluded in both model.

These results give a new constraint in SUSY models or parameter space which is not excluded by Run1 SUSY search.

In future, the LHC-ATLAS experiment plans to accumulate data which correspond to $\sim 100 \text{ fb}^{-1}$ at $\sqrt{s}=13$ (or 14) TeV until 2018. From my simple study, it is expected to reach gluinos with masses up to 2100 GeV in direct-decay model for the massless LSP at 3σ sensitivity reach with the data. Therefore, it might be possible that a gluino with mass which is not excluded by this thesis is discovered in near future.

Acknowledgements

I would like to show my greatest appreciation to my supervisor, Prof. Sachio Komamiya, for his generosity to accept me as a Ph.D. student. Without his support, I could not continue my research.

I would like to express my gratitude to Dr. Naoko Kanaya, for her help to implement new variables to the group analysis and encourage to the development of background estimation method. Her support is also helpful to search a comfortable apartment in France, and this led to increase work efficiency.

I appreciate the feedback offered by Prof. Shoji Asai. His epoch making idea and deep knowledge always helped my analysis. I had many support from Dr. Shimpei Yamamoto about maintenance of computing resource and knowledge about statistical treatment. I would like to thank Prof. Junich Tanaka and Prof. Yuji Enari for the help for upgrade study about the LAr calorimeter and many suggestions for my analysis. I had discussion with Dr. Tatsuya Masubuchi about the background estimation method and it gave me a deep understanding. I super ultra hyper miracle thank Dr. Takashi Yamanaka for his generous support not only for the analysis but also the private life in France. I would like to express my gratitude to Dr. Takuya Nobe for his suggestion for my thesis.

I am deeply grateful to all the staffs and students of ICEPP, the University of Tokyo, and KEK for many supports for research and staying at CERN. I would like to thank Prof. Tatsuo Kawamoto, Prof. Tomio Kobayashi, Prof. Koji Terashi, Dr. Koji Nakamura, Dr. Keita Hanawa, Dr. Tomoyuki Saito, Dr. Yuichi Sasaki, Dr. Shingo Kazama, Dr. Yohei Yamaguchi, Dr. Keisuke Yoshihara, Mr. Masahiro Morinaga, Ms. Aine Kobayashi, Mr. Shion Chen, Mr. Chikuma Kato, Ms. Chihiro Kozakai, Mr. Tatsuya Mori, and Mr. Shunsuke Adachi.

I would like to appreciate the members of analysis group at CERN: Dr. Jamie Boyd, Dr. Tommaso Lari, Dr. Nikola Makovec, Dr. Chris Young, Dr. Marija Vranjes Milosavljevic, and Dr. Laurent Duflet for their enormous support as a convener of the groups. Dr. Judita Mamuzic for help of usage of TMVA. Dr. Yu Nakahama for help of the fit implementation. Dr. Geraldine Conti and Mr. Baptiste Akio Jean abeloos for cooperation of photon studies. Dr. Monica D'Onofrio for her help to study the generator of γ +jets. Dr. Jeanette Miriam Lorenz, Dr. Sophio Pataraiia, and Dr. Sarah Louise Williams for help and cooperation to implement simultaneous fit for data-driven background estimation.

I would like to thank all the members of the ATLAS experiments and the LHC staffs.

For comfortable staying at CERN, I would like to show my appreciation to Mr. Vladimir Troubetzkoi and Ms. Masako Hayashi.

I would like to express my gratitude to my colleagues of the company I was employed for accepting my retirement and wishing my success.

Finally, I want to thank my family.

Appendix

A Photon

In this section, some studies related to photons are described.

A.1 Jet-Photon overlap removal validation

According to the definition of jets in Sec.4.1, photons are also reconstructed as jets. Therefore, the same objects must be removed. In this removal, these three points should be considered:

1. ΔR of photon and jet which are from the same truth photons. This is for the removal of overlap objects.
2. ΔR of photon (from truth photons) and jet (not from truth photons). This is for the check of miss-removal of jets.
3. ΔR of photon (not from truth photons) and jet (not from truth photons). This is for the check of removal of fake photons.

For the 1 and 2, γ +jets MC samples are used. For the 3, QCD multi-jet MC sample are used. The photons are baseline photons (Tight ID) after the overlap removal with electrons and muons are selected. Matching of reconstructed photons with truth photons are with the condition, $\Delta R < 0.05$. The jets are baseline jets after the overlap removal with electrons and muons. Matching of reconstructed jets with truth photons are with the condition, $\Delta R < 0.4$.

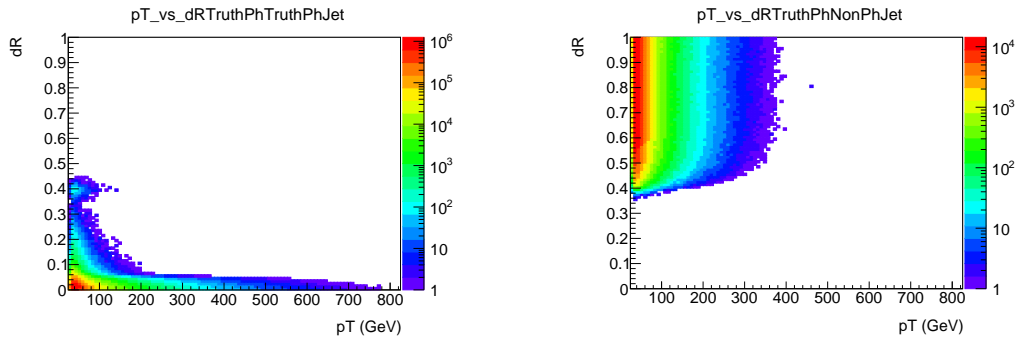
The 2D distribution in ΔR and p_T plane of 1 is shown in Figure 65(a). The candidate ΔR size for overlap removal is 0.4, since the isolation cone size of photon is at most 0.4 and cone size of jet is 0.4. From the figure, it can be seen the $\Delta < 0.4$ is enough to remove the overlap.

γ control region is used to estimate the events of $Z(\rightarrow \nu\nu)$ +jets events in signal region. If the OR with $\Delta R < 0.4$ removes truth jets around a photon, the number of jets behaviour in γ become different and not suitable for the estimation of Z +jets events. Therefore, the ΔR of truth photons and jets are checked with Figure 65(b). In the region, $\Delta R < 0.4$, around truth photons, the jets events are very small and negligible. Thus the excess removal of jets are not worth consideration.

If the ΔR of jet $\rightarrow \gamma$ photon and jets have difference with the truth one, the OR can be used to remove fake events. Therefore, the ΔR of not truth photons and jets are checked with Figure 65(c). If the fake events is dominant in the region away from $\Delta R \sim 0.0$ (e.g. $0.2 < \Delta R < 0.4$), much tight OR can be used to reduce fake

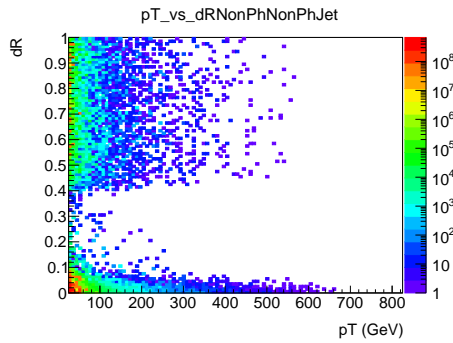
events. However, the fake dominant region is also around $\Delta R \sim 0.0$. Thus the OR cannot help for fake events reduction.

In summary, the overlap removal between photon and jets is only with removal of jets in $\Delta R < 0.4$ of photons.



(a) ΔR between photon and jet which are from the same truth photons.

(b) ΔR between photon (from truth photon) and jet (not from truth photon).



(c) ΔR between photon (not from truth photon) and jet (not from truth photon).

Figure 65: 2D distribution of ΔR vs p_T . Number of events are for the case, $\int L dt = 1.0 \text{ fb}^{-1}$.

A.2 Photon purity estimation with ABCD method

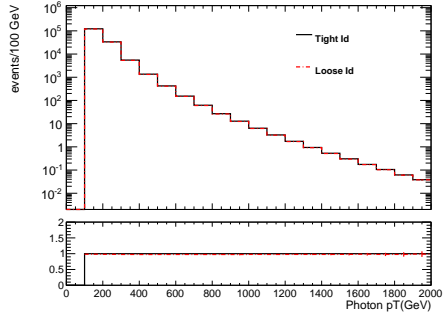
For the estimation of photon purity, ABCD method using photon ID selection and isolation selection is considered.

A.2.1 The difference of overlap-removal and ID order

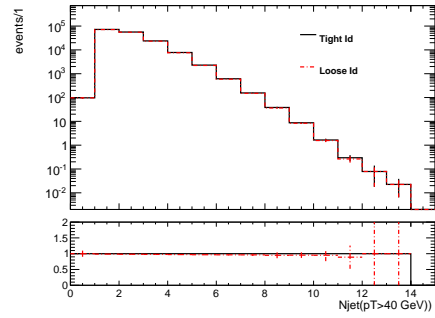
For the ABCD method, photon ID and isolation cuts are considered. For the ID based cuts, baseline photon is Loose ID and the two regions are with Tight ID cut. In final γ CR, we use photons which pass Overlap Removal (OR) with the exact one Tight ID photon selection. Therefore the difference between two types of selections need to be studied.

- Photons pass OR with exact one Tight ID photon.
- Photons pass Tight ID after OR with exact one Loose ID photon.

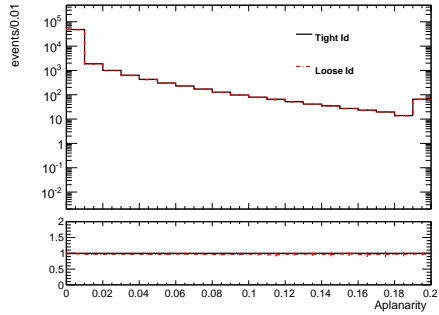
With true γ +jets samples and fake-photon (multi-jet) samples, some variables distributions used in γ CR are checked. In both cases, Cone40 isolation is applied. And no jet related cuts are applied. The comparison for true γ +jets samples are Figure 66 and for fake-photon samples are Figure 67. In any distributions, there are no difference within MC stat. error. Thus, the OR removal with exact one Loose ID photon can be used for the study of Tight ID photon.



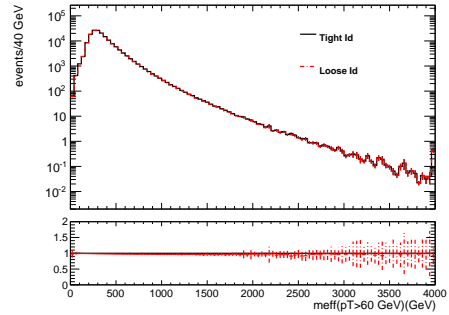
(a) Photon p_T



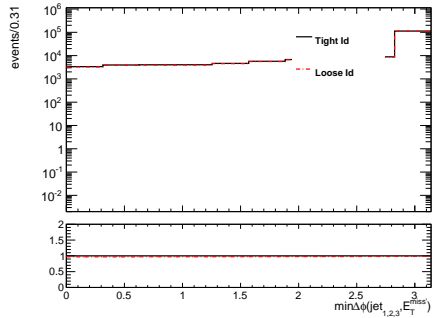
(b) $N_{\text{jet}}(p_T > 40 \text{ GeV})$



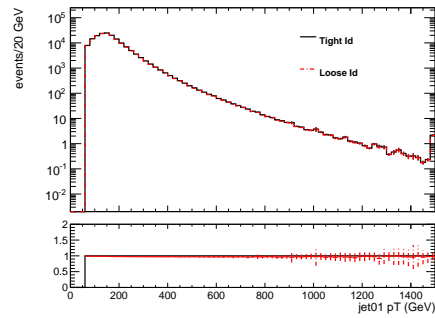
(c) Aplanarity



(d) $m_{\text{eff}}(p_T > 60 \text{ GeV})$

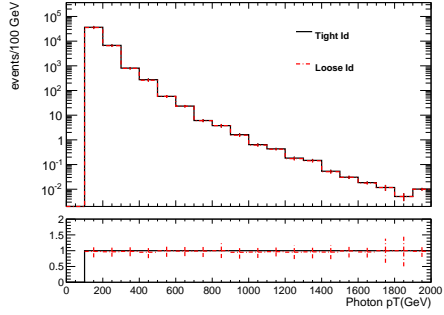


(e) $\min\Delta\phi(j_i, E_T^{\text{miss}})$

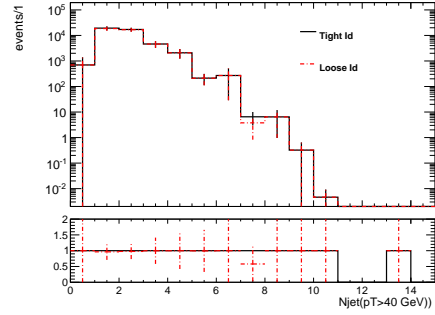


(f) Jet 01 p_T

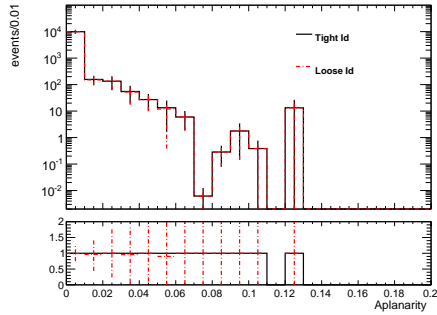
Figure 66: Distributions of each variable with two selection criteria for true photon samples. Black solid line shows the OR with exact one Tight ID photon. Red dotted line shows the Tight ID after the OR with exact one Loose ID photon. The below pad is the ratio plot.



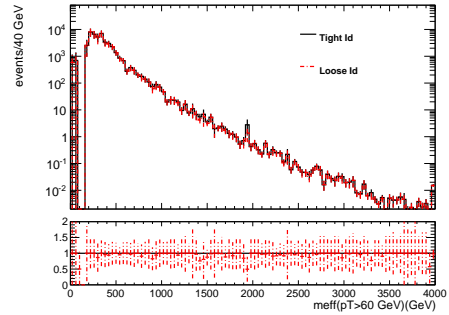
(a) Photon p_T



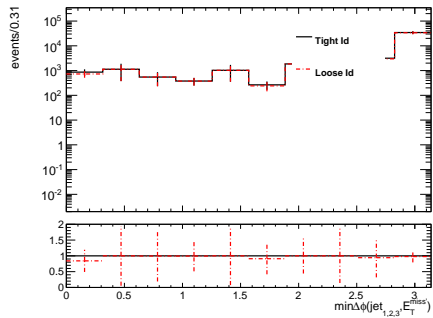
(b) $N_{\text{jet}}(p_T > 40 \text{ GeV})$



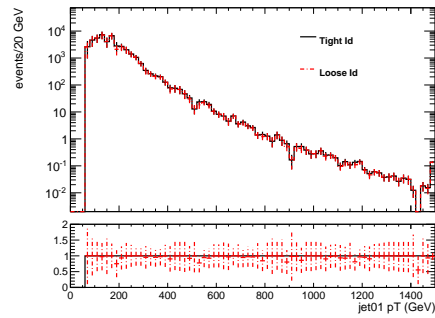
(c) Aplanarity



(d) $m_{\text{eff}}(p_T > 60 \text{ GeV})$



(e) $\min\Delta\phi(j_i, E_T^{\text{miss}})$



(f) Jet01 p_T

Figure 67: Distributions of each variable with two selection criteria for fake-photon samples. Black solid line shows the OR with exact one Tight ID photon. Red dotted line shows the Tight ID after the OR with exact one Loose ID photon. The below pad is the ratio plot.

A.2.2 Correlation study for ABCD method

The target of ABCD method is to estimate multi-jet BGs with data-driven way. Therefore, the correlation between Tight ID related selections with isolation cut after Loose photon ID selection are studied.

The value to evaluate the correlation is R Eq.(107). I selected one loose ID photon ($p_T > 500$ GeV) with multi-jet MC samples to evaluate the R -value. The summary table of the R for each cuts used in Tight ID is Table 74. Even the smallest $|R|$ value, the difference from 1 is 29%. Therefore, the simple ABCD method cannot be applied.

cutname	$ R-1 $	correlation factor
DeltaE	0.29	0.065
Eratio	0.80	0.082
fracm	2.63	0.085
wtot	3.89	0.079
weta1	96.9	0.048
weta2	242.4	0.083
Rphi	336.0	0.032
HadLeak	1040.4	0.056
Reta	1622.0	0.043
f1	2362.5	0.032

Table 74: R value and correlation factor of each cut used in Tight ID and Cone40 Isolation cut. The cuts are sorted ascending order with $|R|$ value.

B TMVA

The Toolkit for MultiVariate Analysis (TMVA)[63] is the software for evaluation of multivariate classification. It includes many packages depend on the purpose of analysis. For the cut optimization, " Rectangular cut optimization " is used. This optimize the rectangular cuts on discriminating variables. In this package, some types of algorithm are implemented. Among them, Genetic Algorithm (GA) is used in this study.

B.1 Genetic algorithm

Each candidate cut combination is called *individual* and the group of *individual* is called *population*. The cut values of discriminating variables for each individual is called *genomes*. The GA is used to make a cut combination which shows smallest efficiency of BG samples for each efficiency of signal samples. The signal efficiency is scanned from 0% to maximum%, and the best optimized cut combinations which minimize the BG efficiency are determined for each signal efficiency. The procedure of the algorithm is as follows:

1. Initialization: The *population* is generated randomly at first. In this analysis 300 *individuals* are generated.
2. Selection: The performance of cut combinations of *individuals* are evaluated. Evaluation is based on the smallness of the efficiency of BG samples against a given signal efficiency. The worst fraction of the *population* is discarded.
3. Reproduction: The selected *individuals* are copied. Some of them are mutated randomly following the Gaussian p.d.f. This means the cut values of individuals are changed randomly.
4. Termination: The steps of selection and reproduction is iterated up to 40 times. The best 10 *individuals* are saved.

This cycle is executed independently 3 times. The best *individual* is selected among the top 30 selections. Then, the best cut combination which minimize BG efficiency for a given signal efficiency is determined.

This algorithm provide higher speed and detailed optimization compared to brute force optimization which scan all the cut combinations of discriminant variables with discrete scan intervals. With some signal points, the optimized cut combinations by GA and brute force method are compared. Since the optimized results are similar, GA method is adopted.

B.1.1 Determination of optimized cut combination

From the processes of GA in TMVA, combinations of a signal efficiency, a BG efficiency, and a cut combination are determined. From the combinations, a cut combination which maximize the significance is determined using the corresponding signal efficiency and the BG efficiency.

C ABCD method

The ABCD method is one of the data-driven estimation method. The idea of the ABCD method is very simple.

The region which you want to estimate a component (signal) is defined as "A". And for the ABCD method, two cuts which have small correlation for the signal events are needed. If such cuts (cut1 and cut2) exists, the rest regions (B, C, D) is defined as in Table 75.

	veto cut1	pass cut1
pass cut2	B	A
veto cut2	D	C

Table 75: Definition of ABCD regions. "A" is the region where the events need to be estimated.

In these conditions, this equation holds:

$$\frac{N_A}{N_B} = \frac{N_C}{N_D}, \quad (98)$$

since two selections with cut1 and cut2 have small correlation. At this point, the small correlation between two cuts is not necessary as far as the Eq.(98) holds.

Thanks to Eq.(98), the signal events in A can be estimated with these equations:

$$N_B^{\text{obs}} = N_A^{\text{Sig}} \times \varepsilon_B, \quad (99)$$

$$N_C^{\text{obs}} = N_A^{\text{Sig}} \times \varepsilon_C, \quad (100)$$

$$N_D^{\text{obs}} = N_A^{\text{Sig}} \times \varepsilon_B \times \varepsilon_C, \quad (101)$$

where $N_B^{\text{obs}}, N_C^{\text{obs}}, N_D^{\text{obs}}$ is the observed events in each region, N_A^{Sig} is the estimated signal events in region A, and the ε s are,

$$\varepsilon_B = \frac{N_B^{\text{Sig}}}{N_A^{\text{Sig}}} \quad (102)$$

$$\varepsilon_C = \frac{N_C^{\text{Sig}}}{N_A^{\text{Sig}}}. \quad (103)$$

In actual cases, the events in regions for the ABCD method is not pure with signal. In such case, the BG components should be subtracted for the method. In

total, the equation is :

$$N_B^{\text{obs}} = N_A^{\text{Sig}} \times \varepsilon_B + N_B^{\text{BG}}, \quad (104)$$

$$N_C^{\text{obs}} = N_A^{\text{Sig}} \times \varepsilon_C + N_C^{\text{BG}}, \quad (105)$$

$$N_D^{\text{obs}} = N_A^{\text{Sig}} \times \varepsilon_B \times \varepsilon_C + N_D^{\text{BG}}, \quad (106)$$

C.1 ABCD method with correction

If the condition Eq.(98) does not hold and there are two components which should be estimated from observed data, the ABCD method in Appendix C cannot be used. In such case, semi data-driven estimation method is needed. In this section, the ABCD method with using some variables from MC is explained. For this estimation, some conditions are needed:

- In each region for ABCD method, one signal and one BG components are dominant.
- For signal events, only the normalization of MC samples should be decided from data. This means ε_B , ε_C , and ε_D from signal MC can be used.
- For BG events, only the double-ratio from MC estimation can be used. The double-ratio is defined as

$$R^{\text{BG,MC}} := \frac{N_A^{\text{BG}} \cdot N_D^{\text{BG}}}{N_B^{\text{BG}} \cdot N_C^{\text{BG}}}. \quad (107)$$

The assumed situation of this method is that signal component is γ +jets event and BG component is jet $\rightarrow \gamma$ fake event, and selections are ID cut and isolation cut. True photon events is comparatively reproduced with MC compared to fake photon events. Therefore, the ratio (ε) from signal MC is used and only the R from BG MC is used. Under this condition, this one equation holds:

$$N_A^{\text{Sig}} = N_A^{\text{obs}} - R^{\text{BG,MC}} \frac{(N_B^{\text{obs}} - \varepsilon_B^{\text{Sig,MC}} N_A^{\text{Sig}}) (N_C^{\text{obs}} - \varepsilon_C^{\text{Sig,MC}} N_A^{\text{Sig}})}{(N_D^{\text{obs}} - \varepsilon_D^{\text{Sig,MC}} N_A^{\text{Sig}})}. \quad (108)$$

From this equation, the N_A^{Sig} is determined uniquely and the uncertainty for this estimation is from MC stat. error of ε and R, and the stat. error of observed data.

References

- [1] ATLAS Collaboration. ‘Observation of a new particle in the search for the Standard Model Higgs boson with the {ATLAS} detector at the {LHC}’. In: *Physics Letters B* 716.1 (2012), pp. 1–29. ISSN: 0370-2693.
DOI: <http://dx.doi.org/10.1016/j.physletb.2012.08.020>.
URL: <http://www.sciencedirect.com/science/article/pii/S037026931200857X>.
- [2] CMS Collaboration. ‘Observation of a new boson at a mass of 125 GeV with the {CMS} experiment at the {LHC}’. In: *Physics Letters B* 716.1 (2012), pp. 30–61. ISSN: 0370-2693.
DOI: <http://dx.doi.org/10.1016/j.physletb.2012.08.021>.
URL: <http://www.sciencedirect.com/science/article/pii/S0370269312008581>.
- [3] K. A. Olive et al. ‘Review of Particle Physics’. In: *Chin. Phys.* C38 (2014), p. 090001.
DOI: [10.1088/1674-1137/38/9/090001](https://doi.org/10.1088/1674-1137/38/9/090001).
- [4] K. G. Begeman, A. H. Broeils and R. H. Sanders. ‘Extended rotation curves of spiral galaxies: Dark haloes and modified dynamics’. In: *Mon. Not. Roy. Astron. Soc.* 249 (1991), p. 523.
- [5] P. A. R. Ade et al. ‘Planck 2013 results. XVI. Cosmological parameters’. In: *Astron. Astrophys.* 571 (2014), A16.
DOI: [10.1051/0004-6361/201321591](https://doi.org/10.1051/0004-6361/201321591).
arXiv: [1303.5076 \[astro-ph.CO\]](https://arxiv.org/abs/1303.5076).
- [6] D. I. Kazakov. ‘Beyond the standard model: In search of supersymmetry’. In: *2000 European School of high-energy physics, Caramulo, Portugal, 20 Aug-2 Sep 2000: Proceedings*. 2000, pp. 125–199.
arXiv: [hep-ph/0012288 \[hep-ph\]](https://arxiv.org/abs/hep-ph/0012288).
URL: <http://alice.cern.ch/format/showfull?sysnb=2235897>.
- [7] Labelle.P. *Supersymmetry Demystified*. The McGraw-Hill Companies, 2008.
- [8] S. P. Martin. ‘A Supersymmetry primer’. In: (1997). [Adv. Ser. Direct. High Energy Phys.18,1(1998)]. DOI: [10.1142/9789812839657_0001](https://doi.org/10.1142/9789812839657_0001), [10.1142/9789814307505_0001](https://doi.org/10.1142/9789814307505_0001).
arXiv: [hep-ph/9709356 \[hep-ph\]](https://arxiv.org/abs/hep-ph/9709356).

- [9] R. Haag, J. T. Łopuszański and M. Sohnius.
‘All possible generators of supersymmetries of the S-matrix’.
In: *Nuclear Physics B* 88 (Mar. 1975), pp. 257–274.
DOI: [10.1016/0550-3213\(75\)90279-5](https://doi.org/10.1016/0550-3213(75)90279-5).
- [10] H. Nishino et al. ‘Search for Proton Decay via $p \rightarrow e^+ \pi^0$ and $p \rightarrow \mu^+ \pi^0$ in a Large Water Cherenkov Detector’.
In: *Phys. Rev. Lett.* 102 (2009), p. 141801.
DOI: [10.1103/PhysRevLett.102.141801](https://doi.org/10.1103/PhysRevLett.102.141801).
arXiv: [0903.0676](https://arxiv.org/abs/0903.0676) [hep-ex].
- [11] C. S. Aulakh et al. ‘See-saw and supersymmetry or exact R-parity’.
In: *Physics Letters B* 459.4 (1999), pp. 557–562. ISSN: 0370-2693.
DOI: [http://dx.doi.org/10.1016/S0370-2693\(99\)00708-X](http://dx.doi.org/10.1016/S0370-2693(99)00708-X).
URL: <http://www.sciencedirect.com/science/article/pii/S037026939900708X>.
- [12] A. H. Chamseddine, R. Arnowitt and P. Nath.
‘Locally Supersymmetric Grand Unification’.
In: *Phys. Rev. Lett.* 49 (14 1982), pp. 970–974.
DOI: [10.1103/PhysRevLett.49.970](https://doi.org/10.1103/PhysRevLett.49.970).
URL: <http://link.aps.org/doi/10.1103/PhysRevLett.49.970>.
- [13] M. Dine and W. Fischler.
‘A phenomenological model of particle physics based on supersymmetry’.
In: *Physics Letters B* 110.3 (1982), pp. 227–231. ISSN: 0370-2693.
DOI: [http://dx.doi.org/10.1016/0370-2693\(82\)91241-2](http://dx.doi.org/10.1016/0370-2693(82)91241-2).
URL: <http://www.sciencedirect.com/science/article/pii/0370269382912412>.
- [14] L. Randall and R. Sundrum. ‘Out of this world supersymmetry breaking’.
In: *Nucl. Phys.* B557 (1999), pp. 79–118.
DOI: [10.1016/S0550-3213\(99\)00359-4](https://doi.org/10.1016/S0550-3213(99)00359-4).
arXiv: [hep-th/9810155](https://arxiv.org/abs/hep-th/9810155) [hep-th].
- [15] H. Baer et al. ‘Gaugino Anomaly Mediated SUSY Breaking: phenomenology and prospects for the LHC’. In: *JHEP* 05 (2010), p. 069.
DOI: [10.1007/JHEP05\(2010\)069](https://doi.org/10.1007/JHEP05(2010)069). arXiv: [1002.4633](https://arxiv.org/abs/1002.4633) [hep-ph].
- [16] E. Halkiadakis, G. Redlinger and D. Shih. ‘Status and Implications of Beyond-the-Standard-Model Searches at the LHC’.
In: *Ann. Rev. Nucl. Part. Sci.* 64 (2014), pp. 319–342.
DOI: [10.1146/annurev-nucl-102313-025632](https://doi.org/10.1146/annurev-nucl-102313-025632).
arXiv: [1411.1427](https://arxiv.org/abs/1411.1427) [hep-ex].

- [17] P. Draper, G. Lee and C. E. Wagner.
‘Precise estimates of the Higgs mass in heavy supersymmetry’.
In: *Phys. Rev. D* 89.5 (2014), p. 055023.
DOI: [10.1103/PhysRevD.89.055023](https://doi.org/10.1103/PhysRevD.89.055023). arXiv: [1312.5743 \[hep-ph\]](https://arxiv.org/abs/1312.5743).
- [18] ATLAS Collaboration. ‘Summary of the searches for squarks and gluinos using $\sqrt{s} = 8$ TeV pp collisions with the ATLAS experiment at the LHC’.
In: *JHEP* 10 (2015), p. 054. DOI: [10.1007/JHEP10\(2015\)054](https://doi.org/10.1007/JHEP10(2015)054).
arXiv: [1507.05525 \[hep-ex\]](https://arxiv.org/abs/1507.05525).
- [19] L. Evans and P. Bryant. ‘LHC Machine’. In: *JINST* 3 (2008), S08001.
DOI: [10.1088/1748-0221/3/08/S08001](https://doi.org/10.1088/1748-0221/3/08/S08001).
- [20] ‘ATLAS photos’. URL: <http://www.atlas.ch/photos/index.html>.
- [21] A. Collaboration.
‘The ATLAS Experiment at the CERN Large Hadron Collider’.
In: *Journal of Instrumentation* 3.08 (2008), S08003.
URL: <http://stacks.iop.org/1748-0221/3/i=08/a=S08003>.
- [22] J. Goodson. ‘Search for Supersymmetry in States with Large Missing Transverse Momentum and Three Leptons including a Z-Boson’.
Presented 17 Apr 2012. PhD thesis. Stony Brook University, 2012.
- [23] ATLAS Collaboration.
ATLAS Insertable B-Layer Technical Design Report.
Tech. rep. CERN-LHCC-2010-013. ATLAS-TDR-19.
Geneva: CERN, 2010. URL: <https://cds.cern.ch/record/1291633>.
- [24] ATLAS Collaboration. ‘ATLAS pixel detector electronics and sensors’.
In: *JINST* 3 (2008), P07007. DOI: [10.1088/1748-0221/3/07/P07007](https://doi.org/10.1088/1748-0221/3/07/P07007).
- [25] ATLAS Collaboration. ‘Luminosity Determination in pp Collisions at $\sqrt{s} = 7$ TeV Using the ATLAS Detector at the LHC’.
In: *Eur. Phys. J. C* 71 (2011), p. 1630.
DOI: [10.1140/epjc/s10052-011-1630-5](https://doi.org/10.1140/epjc/s10052-011-1630-5).
arXiv: [1101.2185 \[hep-ex\]](https://arxiv.org/abs/1101.2185).
- [26] ATLAS Collaboration. ‘Improved luminosity determination in pp collisions at $\sqrt{s} = 7$ TeV using the ATLAS detector at the LHC’.
In: *Eur. Phys. J. C* 73.8 (2013), p. 2518.
DOI: [10.1140/epjc/s10052-013-2518-3](https://doi.org/10.1140/epjc/s10052-013-2518-3).
arXiv: [1302.4393 \[hep-ex\]](https://arxiv.org/abs/1302.4393).
- [27] ‘LuminosityPublicResultsRun2’. URL: https://twiki.cern.ch/twiki/bin/view/AtlasPublic/LuminosityPublicResultsRun2#Publications_and_Conference_Resu.

- [28] S. S. Höche, F. Krauss and F. Siegert. ‘QCD matrix elements and truncated showers’. In: *JHEP* 0905 (2009), p. 053. DOI: [10.1088/1126-6708/2009/05/053](https://doi.org/10.1088/1126-6708/2009/05/053). arXiv: [0903.1219](https://arxiv.org/abs/0903.1219) [[hep-ph](#)].
- [29] H.-L. Lai et al. ‘New parton distributions for collider physics’. In: *Phys. Rev. D* 82 (2010), p. 074024. DOI: [10.1103/PhysRevD.82.074024](https://doi.org/10.1103/PhysRevD.82.074024). arXiv: [1007.2241](https://arxiv.org/abs/1007.2241) [[hep-ph](#)].
- [30] R. D. Ball et al. ‘Parton distributions with LHC data’. In: *Nucl. Phys.* B867 (2013), pp. 244–289. DOI: [10.1016/j.nuclphysb.2012.10.003](https://doi.org/10.1016/j.nuclphysb.2012.10.003). arXiv: [1207.1303](https://arxiv.org/abs/1207.1303) [[hep-ph](#)].
- [31] M. L. Mangano et al. ‘Matching matrix elements and shower evolution for top-quark production in hadronic collisions’. In: *JHEP* 01 (2007), p. 013. DOI: [10.1088/1126-6708/2007/01/013](https://doi.org/10.1088/1126-6708/2007/01/013). arXiv: [hep-ph/0611129](https://arxiv.org/abs/hep-ph/0611129) [[hep-ph](#)].
- [32] L. Lonnblad and S. Prestel. ‘Matching Tree-Level Matrix Elements with Interleaved Showers’. In: *JHEP* 03 (2012), p. 019. DOI: [10.1007/JHEP03\(2012\)019](https://doi.org/10.1007/JHEP03(2012)019). arXiv: [1109.4829](https://arxiv.org/abs/1109.4829) [[hep-ph](#)].
- [33] D. J. Lange. ‘The EvtGen particle decay simulation package’. In: *Nucl. Instrum. Meth.* A462 (2001), pp. 152–155. DOI: [10.1016/S0168-9002\(01\)00089-4](https://doi.org/10.1016/S0168-9002(01)00089-4).
- [34] S. Agostinelli et al. ‘GEANT4: A Simulation toolkit’. In: *Nucl. Instrum. Meth.* A506 (2003), pp. 250–303. DOI: [10.1016/S0168-9002\(03\)01368-8](https://doi.org/10.1016/S0168-9002(03)01368-8).
- [35] ATLAS Collaboration. *Performance assumptions for an upgraded ATLAS detector at a High-Luminosity LHC*. Tech. rep. ATL-PHYS-PUB-2013-004. Geneva: CERN, 2013. URL: <http://cds.cern.ch/record/1527529>.
- [36] T. Gleisberg et al. ‘Event generation with SHERPA 1.1’. In: *JHEP* 0902 (2009), p. 007. DOI: [10.1088/1126-6708/2009/02/007](https://doi.org/10.1088/1126-6708/2009/02/007). arXiv: [0811.4622](https://arxiv.org/abs/0811.4622) [[hep-ph](#)].
- [37] T. Sjöstrand et al. ‘An Introduction to PYTHIA 8.2’. In: *Comput. Phys. Commun.* 191 (2015), pp. 159–177. DOI: [10.1016/j.cpc.2015.01.024](https://doi.org/10.1016/j.cpc.2015.01.024). arXiv: [1410.3012](https://arxiv.org/abs/1410.3012) [[hep-ph](#)].
- [38] Sjöstrand, Torbjorn and Mrenna, Stephen and Skands, Peter Z. ‘PYTHIA 6.4 Physics and Manual’. In: *JHEP* 0605 (2006), p. 026. DOI: [10.1088/1126-6708/2006/05/026](https://doi.org/10.1088/1126-6708/2006/05/026). arXiv: [hep-ph/0603175](https://arxiv.org/abs/hep-ph/0603175).

- [39] J. Alwall et al. ‘The automated computation of tree-level and next-to-leading order differential cross sections, and their matching to parton shower simulations’. In: *JHEP* 07 (2014), p. 079. DOI: [10.1007/JHEP07\(2014\)079](https://doi.org/10.1007/JHEP07(2014)079). arXiv: [1405.0301](https://arxiv.org/abs/1405.0301) [hep-ph].
- [40] M. Bahr et al. ‘Herwig++ Physics and Manual’. In: *Eur. Phys. J. C* 58 (2008), pp. 639–707. DOI: [10.1140/epjc/s10052-008-0798-9](https://doi.org/10.1140/epjc/s10052-008-0798-9). arXiv: [0803.0883](https://arxiv.org/abs/0803.0883) [hep-ph].
- [41] *NLL-fast*. URL: http://pauli.uni-muenster.de/~akule_01/nllwiki/index.php/NLL-fast.
- [42] W. Beenakker et al. ‘Squark and gluino production at hadron colliders’. In: *Nucl. Phys. B* 492 (1997), pp. 51–103. DOI: [10.1016/S0550-3213\(97\)80027-2](https://doi.org/10.1016/S0550-3213(97)80027-2). arXiv: [hep-ph/9610490](https://arxiv.org/abs/hep-ph/9610490) [hep-ph].
- [43] A. Kulesza and L. Motyka. ‘Threshold resummation for squark-antisquark and gluino-pair production at the LHC’. In: *Phys. Rev. Lett.* 102 (2009), p. 111802. DOI: [10.1103/PhysRevLett.102.111802](https://doi.org/10.1103/PhysRevLett.102.111802). arXiv: [0807.2405](https://arxiv.org/abs/0807.2405) [hep-ph].
- [44] A. Kulesza and L. Motyka. ‘Soft gluon resummation for the production of gluino-gluino and squark-antisquark pairs at the LHC’. In: *Phys. Rev. D* 80 (2009), p. 095004. DOI: [10.1103/PhysRevD.80.095004](https://doi.org/10.1103/PhysRevD.80.095004). arXiv: [0905.4749](https://arxiv.org/abs/0905.4749) [hep-ph].
- [45] W. Beenakker et al. ‘Soft-gluon resummation for squark and gluino hadroproduction’. In: *JHEP* 12 (2009), p. 041. DOI: [10.1088/1126-6708/2009/12/041](https://doi.org/10.1088/1126-6708/2009/12/041). arXiv: [0909.4418](https://arxiv.org/abs/0909.4418) [hep-ph].
- [46] W. Beenakker et al. ‘Squark and Gluino Hadroproduction’. In: *Int. J. Mod. Phys. A* 26 (2011), pp. 2637–2664. DOI: [10.1142/S0217751X11053560](https://doi.org/10.1142/S0217751X11053560). arXiv: [1105.1110](https://arxiv.org/abs/1105.1110) [hep-ph].
- [47] W Lampl et al. *Calorimeter Clustering Algorithms: Description and Performance*. Tech. rep. ATL-LARG-PUB-2008-002. ATL-COM-LARG-2008-003. Geneva: CERN, 2008. URL: <https://cds.cern.ch/record/1099735>.
- [48] M. Cacciari, G. P. Salam and G. Soyez. ‘The Anti-k(t) jet clustering algorithm’. In: *JHEP* 04 (2008), p. 063. DOI: [10.1088/1126-6708/2008/04/063](https://doi.org/10.1088/1126-6708/2008/04/063). arXiv: [0802.1189](https://arxiv.org/abs/0802.1189) [hep-ph].

- [49] ATLAS Collaboration. *Monte Carlo Calibration and Combination of In-situ Measurements of Jet Energy Scale, Jet Energy Resolution and Jet Mass in ATLAS*. Tech. rep. ATLAS-CONF-2015-037. Geneva: CERN, 2015. URL: <http://cds.cern.ch/record/2044941>.
- [50] ATLAS Collaboration. *Expected performance of the ATLAS b-tagging algorithms in Run-2*. Tech. rep. ATL-PHYS-PUB-2015-022. Geneva: CERN, 2015. URL: <https://cds.cern.ch/record/2037697>.
- [51] *Commissioning of the ATLAS b-tagging algorithms using $t\bar{t}$ events in early Run-2 data*. Tech. rep. ATL-PHYS-PUB-2015-039. Geneva: CERN, 2015. URL: <https://cds.cern.ch/record/2047871>.
- [52] ATLAS Collaboration. *Selection of jets produced in 13TeV proton-proton collisions with the ATLAS detector*. Tech. rep. ATLAS-CONF-2015-029. Geneva: CERN, 2015. URL: <https://cds.cern.ch/record/2037702>.
- [53] ATLAS Collaboration. *Expected electron performance in the ATLAS experiment*. Tech. rep. ATL-PHYS-PUB-2011-006. Geneva: CERN, 2011. URL: <https://cds.cern.ch/record/1345327>.
- [54] ATLAS Collaboration. *Electron identification measurements in ATLAS using $\sqrt{s} = 13$ TeV data with 50 ns bunch spacing*. Tech. rep. ATL-PHYS-PUB-2015-041. Geneva: CERN, 2015. URL: <https://cds.cern.ch/record/2048202>.
- [55] ATLAS Collaboration. ‘Measurement of the muon reconstruction performance of the ATLAS detector using 2011 and 2012 LHC proton–proton collision data’. In: *Eur. Phys. J. C* 74.11 (2014), p. 3130. DOI: [10.1140/epjc/s10052-014-3130-x](https://doi.org/10.1140/epjc/s10052-014-3130-x). arXiv: [1407.3935](https://arxiv.org/abs/1407.3935) [hep-ex].
- [56] *Muon reconstruction performance in early $\sqrt{s} = 13$ TeV data*. Tech. rep. ATL-PHYS-PUB-2015-037. Geneva: CERN, 2015. URL: <https://cds.cern.ch/record/2047831>.
- [57] ATLAS Collaboration. *Expected performance of missing transverse momentum reconstruction for the ATLAS detector at $\sqrt{s} = 13$ TeV*. Tech. rep. ATL-PHYS-PUB-2015-023. Geneva: CERN, 2015. URL: <http://cds.cern.ch/record/2037700>.

- [58] ATLAS Collaboration. ‘Performance of the ATLAS Trigger System in 2010’. In: *Eur. Phys. J. C* 72 (2012), p. 1849. DOI: [10.1140/epjc/s10052-011-1849-1](https://doi.org/10.1140/epjc/s10052-011-1849-1). arXiv: [1110.1530](https://arxiv.org/abs/1110.1530) [hep-ex].
- [59] ATLAS Collaboration. *Search for squarks and gluinos with the ATLAS detector in final states with jets and missing transverse momentum and 20.3 fb⁻¹ of $\sqrt{s} = 8$ TeV proton-proton collision data*. Tech. rep. ATLAS-CONF-2013-047. Geneva: CERN, 2013. URL: <http://cds.cern.ch/record/1547563>.
- [60] C. Chen. ‘New approach to identifying boosted hadronically-decaying particle using jet substructure in its center-of-mass frame’. In: *Phys. Rev. D* 85 (2012), p. 034007. DOI: [10.1103/PhysRevD.85.034007](https://doi.org/10.1103/PhysRevD.85.034007). arXiv: [1112.2567](https://arxiv.org/abs/1112.2567) [hep-ph].
- [61] H.-M. Chang et al. ‘Calculating track thrust with track functions’. In: *Phys. Rev. D* 88 (3 2013), p. 034030. DOI: [10.1103/PhysRevD.88.034030](https://doi.org/10.1103/PhysRevD.88.034030). URL: <http://link.aps.org/doi/10.1103/PhysRevD.88.034030>.
- [62] K. Cranmer. ‘Statistical Challenges for Searches for New Physics at the LHC’. In: *Statistical Problems in Particle Physics, Astrophysics and Cosmology*. Ed. by L. Lyons and M. Karagöz Ünel. 2006, p. 112. DOI: [10.1142/9781860948985_0026](https://doi.org/10.1142/9781860948985_0026). eprint: [physics/0511028](https://arxiv.org/abs/physics/0511028).
- [63] A. Hoecker et al. ‘TMVA: Toolkit for Multivariate Data Analysis’. In: *PoS ACAT* (2007), p. 040. arXiv: [physics/0703039](https://arxiv.org/abs/physics/0703039).
- [64] S. Ask et al. ‘Using gamma+jets Production to Calibrate the Standard Model Z(nunu)+jets Background to New Physics Processes at the LHC’. In: *JHEP* 10 (2011), p. 058. DOI: [10.1007/JHEP10\(2011\)058](https://doi.org/10.1007/JHEP10(2011)058). arXiv: [1107.2803](https://arxiv.org/abs/1107.2803) [hep-ph].
- [65] CMS Collaboration. *Data-Driven Estimation of the Invisible Z Background to the SUSY MET Plus Jets Search*. Tech. rep. CMS-PAS-SUS-08-002. 2009. Geneva: CERN, 2009. URL: <https://cds.cern.ch/record/1194471>.
- [66] G. Cowan et al. ‘Asymptotic formulae for likelihood-based tests of new physics’. In: *Eur. Phys. J. C* 71 (2011). [Erratum: *Eur. Phys. J. C* 73,2501(2013)], p. 1554. DOI: [10.1140/epjc/s10052-011-1554-0](https://doi.org/10.1140/epjc/s10052-011-1554-0), [10.1140/epjc/s10052-013-2501-z](https://doi.org/10.1140/epjc/s10052-013-2501-z). arXiv: [1007.1727](https://arxiv.org/abs/1007.1727) [physics.data-an].

- [67] A. L. Read. ‘Presentation of search results: the CL_s technique’. In: *Journal of Physics G: Nuclear and Particle Physics* 28.10 (2002), p. 2693.
URL: <http://stacks.iop.org/0954-3899/28/i=10/a=313>.
- [68] G. Cowan. *Statistics and Discoveries at the LHC (3/4)*.
URL: http://indico.cern.ch/event/77832/attachments/1057380/1507689/cowan_cern_3.pdf.
- [69] ATLAS Collaboration. ‘Jet energy measurement with the ATLAS detector in proton-proton collisions at $\sqrt{s} = 7$ TeV’.
In: *Eur. Phys. J. C* 73.3 (2013), p. 2304.
DOI: [10.1140/epjc/s10052-013-2304-2](https://doi.org/10.1140/epjc/s10052-013-2304-2).
arXiv: [1112.6426](https://arxiv.org/abs/1112.6426) [hep-ex].
- [70] ATLAS Collaboration.
‘Single hadron response measurement and calorimeter jet energy scale uncertainty with the ATLAS detector at the LHC’.
In: *Eur. Phys. J. C* 73.3 (2013), p. 2305.
DOI: [10.1140/epjc/s10052-013-2305-1](https://doi.org/10.1140/epjc/s10052-013-2305-1).
arXiv: [1203.1302](https://arxiv.org/abs/1203.1302) [hep-ex].
- [71] ATLAS Collaboration. *Jet Calibration and Systematic Uncertainties for Jets Reconstructed in the ATLAS Detector at $\sqrt{s} = 13$ TeV*.
Tech. rep. ATL-PHYS-PUB-2015-015. Geneva: CERN, 2015.
URL: <http://cds.cern.ch/record/2037613>.
- [72] ATLAS Collaboration. ‘Jet energy resolution in proton-proton collisions at $\sqrt{s} = 7$ TeV recorded in 2010 with the ATLAS detector’.
In: *Eur. Phys. J. C* 73.3 (2013), p. 2306.
DOI: [10.1140/epjc/s10052-013-2306-0](https://doi.org/10.1140/epjc/s10052-013-2306-0).
arXiv: [1210.6210](https://arxiv.org/abs/1210.6210) [hep-ex].
- [73] ATLAS Collaboration. ‘Summary of ATLAS Pythia 8 tunes’.
In: *ATL-PHYS-PUB-2012-003* (2012).
URL: <https://cds.cern.ch/record/1474107>.
- [74] P. Z. Skands. ‘Tuning Monte Carlo Generators: The Perugia Tunes’.
In: *Phys. Rev. D* 82 (2010), p. 074018.
DOI: [10.1103/PhysRevD.82.074018](https://doi.org/10.1103/PhysRevD.82.074018). arXiv: [1005.3457](https://arxiv.org/abs/1005.3457) [hep-ph].
- [75] G. E. Wolf. ‘HERA: Physics, Machine and Experiments’.
In: *NATO Sci. Ser. B* 164 (1987), pp. 375–449.
DOI: [10.1007/978-1-4684-5401-7_6](https://doi.org/10.1007/978-1-4684-5401-7_6).

- [76] J. F. Owens, A. Accardi and W. Melnitchouk.
'Global parton distributions with nuclear and finite- Q^2 corrections'.
In: *Phys. Rev. D* 87.9 (2013), p. 094012.
doi: [10.1103/PhysRevD.87.094012](https://doi.org/10.1103/PhysRevD.87.094012). arXiv: [1212.1702](https://arxiv.org/abs/1212.1702) [hep-ph].
- [77] A. D. Martin et al. 'Parton distributions for the LHC'.
In: *Eur. Phys. J. C* 63 (2009), pp. 189–285.
doi: [10.1140/epjc/s10052-009-1072-5](https://doi.org/10.1140/epjc/s10052-009-1072-5).
arXiv: [0901.0002](https://arxiv.org/abs/0901.0002) [hep-ph].
- [78] CMS Collaboration. 'Searches for Supersymmetry using the M_{T2} Variable in Hadronic Events Produced in pp Collisions at 8 TeV'.
In: *JHEP* 05 (2015), p. 078. doi: [10.1007/JHEP05\(2015\)078](https://doi.org/10.1007/JHEP05(2015)078).
arXiv: [1502.04358](https://arxiv.org/abs/1502.04358) [hep-ex].
- [79] ATLAS Collaboration. 'Search for squarks and gluinos with the ATLAS detector in final states with jets and missing transverse momentum using $\sqrt{s} = 8$ TeV proton-proton collision data'. In: *JHEP* 1409 (2014), p. 176.
doi: [10.1007/JHEP09\(2014\)176](https://doi.org/10.1007/JHEP09(2014)176). arXiv: [1405.7875](https://arxiv.org/abs/1405.7875) [hep-ex].
- [80] CMS Collaboration. 'Search for new physics in the multijet and missing transverse momentum final state in proton-proton collisions at $\sqrt{s} = 8$ TeV'.
In: *JHEP* 06 (2014), p. 055. doi: [10.1007/JHEP06\(2014\)055](https://doi.org/10.1007/JHEP06(2014)055).
arXiv: [1402.4770](https://arxiv.org/abs/1402.4770) [hep-ex].